Dark Cosmology Centre

Galaxy Evolution Over the Past Eleven Billion Years: Mergers and Quiescence

Allison Wing Shan Man

Advisor: Sune Toft
Co-advisor: Andrew Zirm

A dissertation submitted for the degree of
Doctor of Philosophy (PhD)

Dark Cosmology Centre, Niels Bohr Institute
Faculty of Science, University of Copenhagen

Submission: *18/11/2014*
Defence: *17/12/2014*

Opponents: *Prof. Jens Hjorth*
Dr. Jennifer Lotz
Prof. Piero Rosati

Cover image: "The Antennae Galaxies through the eyes of *Hubble* and ALMA"

The Antennae Galaxies (NGC 4038 and 4039) are two spiral galaxies undergoing a collision. Located 70 million light-years away, they offer an opportunity to examine the physics of extreme starbursts triggered by the galaxy merger. The newborn stars, shown in blue, were imaged at visible wavelengths by the *Hubble Space Telescope*. The recently commissioned Atacama Large Millimeter/Submillimeter Array imaged the emission of molecular gas clouds, the fuel for star formation, as overlaid in orange. The optical blue star-forming regions are only visible in regions free of obscuration by the dust in the orange molecular gas clouds. This image illustrates the need for multi-wavelength observations for a comprehensive understanding of the physical conditions in galaxies.

Credits: B. Saxton, (NRAO/AUI/NSF), ALMA (ESO/NAOJ/NRAO). Visible light image: the NASA/ESA *Hubble Space Telescope*

ABSTRACT

Galaxy evolution studies have been revolutionized by the advent of near-infrared observations over the last decade. An intriguingly population of distant red galaxies, only visible at near-infrared wavelengths, was discovered. They were previously overlooked, since they are invisible even in the deepest *Hubble Space Telescope (HST)* optical surveys. Their stellar populations, characterized using deep near-infrared photometric and spectroscopic observations, reveal that they are the most massive and evolved galaxies at early epochs. This suggests that they have undergone a rapid build-up of stellar mass followed by a short-lived, effective phase of star formation quenching. Curiously, their stellar densities are an order of magnitude higher than their local counterparts, containing 10^{11} solar masses within a radius of only 1.5 kpc. No similar galaxies exist in the local Universe, therefore they must undergo significant size evolution to become present-day giant ellipticals. The need for further evolution lends strong support to the idea that large galaxies form from hierarchal assembly, effective ruling out the monolithic collapse model. It is therefore important to understand the formation and evolution of this peculiar population of compact, massive quiescent galaxies, which in turn provides constraints to galaxy formation models.

Despite the wealth of observations, the dominant physical mechanisms driving the evolution of galaxies are still fiercely debated. Is galaxy merging a dominant mechanism in evolving the sizes and stellar masses of quiescent galaxies? Are quiescent galaxies truly passive, or are their stellar populations in fact not old but reddened by dust? The goal of this thesis is to address these two outstanding questions, in order to verify the existence of such an extreme galaxy population, and to measure the contribution of galaxy merging in evolving them into local ellipticals. In Chapter 1, I provide a broad overview of the current understanding of this population of quiescent massive galaxies, from their initial discovery a decade ago, to the latest findings based on state-of-the-art observations as well as theoretical models.

Galaxy merging is a major prediction of the concordance cosmology model, whereby large galaxies are assembled from merging smaller ones. Merging with smaller satellites can puff up the sizes of quiescent galaxies, yet it remains questionable whether galaxies merge frequently enough to match the required growth. Chapters 2 and 3 are

therefore devoted to measuring the redshift evolution of the galaxy merger fraction and rate. In Chapter 2, we present measurements of the galaxy major merger fraction of massive galaxies at $z = 0 - 3$ using *HST*/NICMOS. We show that the galaxy major merger fraction increases mildly with redshift out to $z = 3$. However, the limited sample size precludes us from understanding the reason for the discrepant measurements among similar studies. Chapter 3 reports our investigation of how systematic effects bias merger fraction measurements. We assemble the largest photometrically selected merger sample out to $z = 3$, using the latest deep near-infrared *HST*/WFC3 CANDELS survey and the ground-based UltraVISTA survey. The large sample size leads to significantly smaller random errors, and we use it to conduct a comparative study on homogeneous datasets. We demonstrate that previous galaxy merger fraction measurements at $z \sim 2$ were discrepant, because mergers were not selected in the same way. Selecting galaxy mergers by the observed H-band flux ratio leads to a bias towards bright star-forming satellites at $z > 2$, while selecting by stellar mass ratio is biased against these gas-rich satellites. Major and minor merging combined can only explain half of the size evolution observed for massive quiescent galaxies during $z = 0 - 2.5$. Additional processes are thus required to explain their observed strong average size evolution.

The quiescence of galaxies is inferred from their flat ultraviolet continuum slope. However, strong dust attenuation can lead to similarly red colors in obscured star-forming galaxies. Infrared observations that probe the dust-reprocessed starlight are thus required to detect obscured star formation. In Chapter 4, we test the null hypothesis that quiescent galaxies (classified as having modest unobscured star formation rates) are in fact dust-obscured starbursts, through a stacking analysis on the mid-, far-infrared and radio data. We confirm that on average quiescent galaxies do not host strong dust-obscured starbursts, and place stringent upper limits on their obscured star formations rates. Our results corroborate the need for strong quenching mechanisms. Quiescent galaxies show strong emissions in the radio stacks, in excess of those expected from the total (unobscured + obscured) star formation rate upper limits. This suggests a widespread presence of low-luminosity active galactic nuclei among quiescent galaxies.

CONTENTS

Dedicated to my family

ACKNOWLEDGMENTS

I would like to express my gratitude to Sune, who has been the most supportive, trusting and patient advisor. Thank you for reminding me of the big picture, for always making time to comment on my writing. I was fortunate to have Andrew as my co-advisor, who has been very resourceful and generous to share his knowledge and skills. I also thank Thomas, from whom I have learnt a lot about the gas and dust in galaxies, and the importance of writing terse and crisp. I thank the three of you for the encouragements, the guidance and for making my PhD studies enjoyable.

My gratitude extends to the entire DARK family. In particular, I am grateful to Jens, Anja and Johan, for convincing the Faculty of Science to offer a tuition waiver and a stipend for my MSc studies. My PhD studies was generously funded by the Niels Bohr Institute and the Danish National Research Foundation. The interactive atmosphere at DARK makes it a great learning environment. I thank all DARKers for contributing to this unique space-time. I appreciate the career and scientific discussions with many DARKers, especially Marianne, Kristian, Moire, Lise, and Jens. The DARK administration (Michelle, Julie, Corinne) and IT staff (Brian and Damon) are thanked for being so helpful and accommodating. I thank Stefan for giving me an opportunity to observe on La Palma and in Chile, and Martin for commenting on parts of this thesis.

I would like to thank Dave and Josh for hosting my six-month visit at IfA Hawaii. During my stay, I have learnt a lot about far-infrared astronomy and mergers through interacting with Dave, his group and Josh. I thank Caitlin and Mike for letting me help run their observing programs on Mauna Kea.

I must thank Prof. Kinwah Wu for being a dedicated mentor. He has been supportive of my research endeavors, and has always reminded me to strive to be a better scientist. I also thank my collaborators who contributed to the projects in this thesis.

A special thanks to my friends, at DARK, outside DARK, in Hong Kong and across continents, for your friendship and support. Not naming names here but I hope you know that I enjoy your company and you will be missed. My time at ECDK has been especially inspiring. Most important of all, I thank my family and Simon for their support and understanding.

1

INTRODUCTION

The concept of the Universe being made up of many galaxies like our own Milky Way has emerged since the 18^{th} century. However, only with the advent of large telescopes in the last century have astronomers been able to survey the deep sky, and made revolutionary discoveries in the field of galaxy evolution. Galaxies evolve on astronomical timescales much beyond human lifespans. By conducting censuses on millions of galaxies, astronomers effectively obtain snapshots of galaxies at different stages of their lives. The aim of extragalactic research is to determine the physical mechanisms that act on the various components of galaxies (stars, gas, dark matter, black hole), thereby drawing evolutionary links between the various phases of galaxies.

1.1 THE DISTANT RED AND DEAD GALAXIES

THEIR DISCOVERY

A significant population of "red and dead" galaxies were initially discovered in near-infrared imaging surveys (Daddi et al., 2003; Franx et al., 2003). This sample of red galaxies were selected with a red $J - K_s$ color to sample the strong Balmer / 4000 Å break in the spectra of massive galaxies at $2 < z < 4$. Their discovery was revolutionary, because this population of galaxies were invisible even in the deepest *Hubble* optical images. The optical faintness, combined with the lack of strong emission lines, indicates that they have no current star formation. Similarly red, quiescent massive galaxies with such compact sizes are extremely rare in the local Universe (Taylor et al., 2009; Trujillo et al., 2009; Shih & Stockton, 2011). Passive evolution is shown to be insufficient for increasing their sizes rapidly enough to match with observations (Kriek et al., 2008; Toft et al., 2009), if they are to evolve into local giant ellipticals of similar mass and quiescence. The mechanisms responsible for the size growth are the topics of active debate.

COMPACTNESS

The first indications of the compact nature of red and dead galaxies came from the inability to resolve them by ground-based telescopes (e.g. ISAAC at the Very Large Telescope). The compactness was later on confirmed by high resolution near-infrared imaging obtained from the *Hubble Space Telescope (HST)* with NICMOS (Daddi et al., 2005; Toft et al., 2005; Trujillo et al., 2006b; Toft et al., 2007; Zirm et al., 2007; Cimatti et al., 2008; van Dokkum et al., 2008; Damjanov et al., 2009; Kriek et al., 2009b). The more recently commissioned near-infrared instrument WFC3 onboard *HST* provides smaller pixel scales, allowing even more accurate size measurements (Cassata et al., 2010; Szomoru et al., 2010; Newman et al., 2012; Cassata et al., 2013; Chang et al., 2013; van der Wel et al., 2014), and even bulge-disk decomposition (Bruce et al., 2014). As these galaxies represent the most massive galaxies at early epochs, containing stellar masses $M_{\star} \gtrsim 10^{11}\ M_{\odot}$, their compactness implies extremely high stellar mass densities, an order of magnitude higher than their local counterparts (Zirm et al., 2007; Franx et al., 2008).

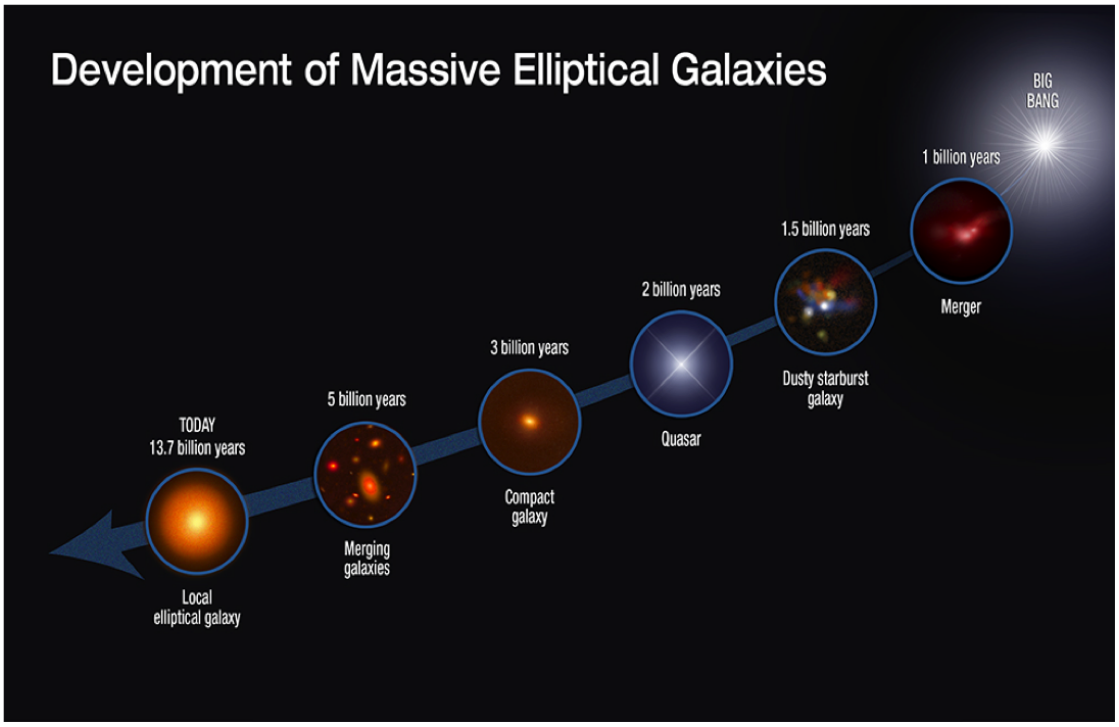

Figure 1.1: An illustration illustrating a plausible formation and evolutionary scenario of red and dead galaxies over cosmic history. (Credit: Sune Toft, *HST* press office.)

The compactness of the red and dead galaxies hints at a dissipational formation process. Various hydrodynamical simulations (e.g., Barnes 1990; Barnes & Hernquist 1991;

Mihos & Hernquist 1996; Di Matteo et al. 2005; Hopkins & Beacom 2006; Wuyts et al. 2010, although see Naab et al. 2007) have illustrated a viable path for the formation of massive, compact quiescent galaxies: during a gas-rich galaxy merger, gas loses angular momentum through gravitational torques, leading to strong gas inflows towards the center to fuel a nuclear starburst and an efficient phase of black hole accretion (quasar). After $\sim$ 1 Gyr, the radiation feedback of the accreting black hole terminates further star formation, either by heating up the gas and/or expelling the gas from the merger remnant (Di Matteo et al., 2005; Springel et al., 2005; Bower et al., 2006; Croton et al., 2006), leaving behind a dense stellar core devoid of cold molecular gas for further star formation. This is illustrated in the first four phases in Figure 1.1.

As galaxies evolve on timescales of billions of years, we are not able to follow their temporal changes and need to draw connections between these phases. While the mechanism responsible for terminating star formation in massive galaxies remains debated, various observations have demonstrated actively accretive black holes are predominantly found in recently quenched galaxies (Schawinski et al., 2009a,b; Barro et al., 2014), and have high-velocity (500 – 1000 km s^{-1}) gas outflows (Tremonti et al., 2007; Cimatti et al., 2013) as predicted by the above-mentioned feedback models. The number densities of dusty starburst galaxies are consistent with those of compact quiescent galaxies, as recently shown by Toft et al. (2014). These results lend support to the first four stages of the evolutionary scenario in Figure 1.1.

QUIESCENCE AND EVOLVED STELLAR POPULATIONS

Since the initial discovery of red and dead galaxies from photometric imaging surveys, their high redshifts ($z \gtrsim 2$) and quiescence were later confirmed by deep near-infrared spectroscopy (van Dokkum et al., 2003; Daddi et al., 2005; Kriek et al., 2006a,b). However, their faintness in optical and near-infrared implies long integration time, precluding large spectroscopic samples to be made. Only $\lesssim 10$ compact massive quiescent galaxies at $z \gtrsim 1.8$ have near-infrared spectra sufficiently deep for absorption line studies (van Dokkum et al., 2009; Onodera et al., 2010; van de Sande et al., 2011; Toft et al., 2012; van de Sande et al., 2013; Belli et al., 2014b).

Figure 1.2 illustrates a deep spectrum with VLT/X-SHOOTER for a massive compact quiescent galaxy at $z \sim 2$. The strong Balmer break indicates that the galaxy hosts significant stellar masses, while the flat ultraviolet continuum and the lack of strong emission lines are consistent with no ongoing star formation. Interestingly, the majority of the spectroscopically confirmed quiescent galaxies show post-starburst spectral shapes and young stellar ages (0.4 – 1 Gyr), perhaps due to the fact that the brightest quiescent galaxies are preferentially selected for spectroscopic follow-up.

A very deep 29-hour Gemini/GNIRS spectrum of a massive quiescent galaxy reveals faint emission lines, which are typical of low-ionization nuclear emission-line re-

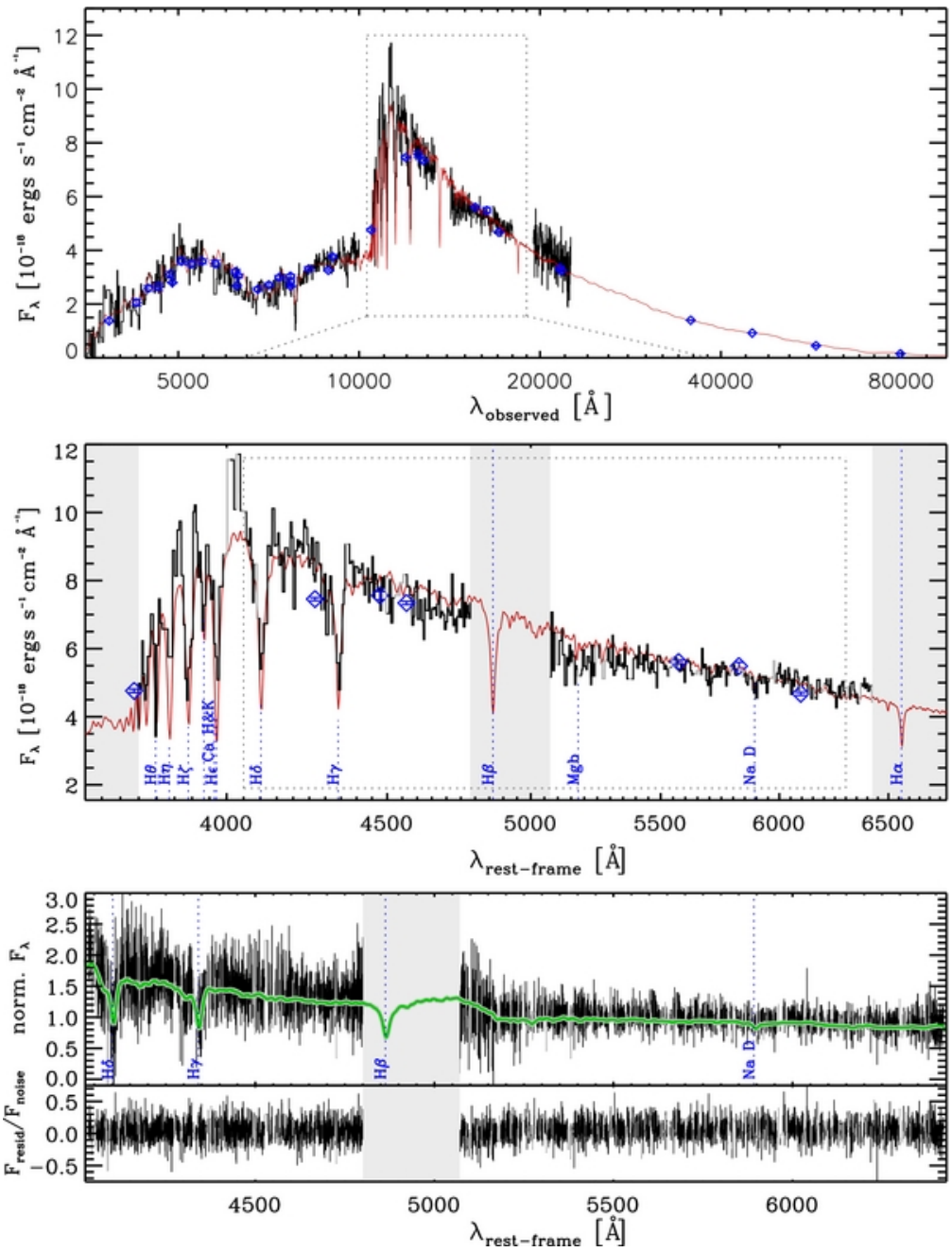

Figure 1.2: Deep VLT/X-SHOOTER spectrum for a massive quiescent galaxy at $z = 1.8$ (van de Sande et al., 2011). This galaxy has $M_\star = 1.5 \times 10^{11} M_\odot$ derived from its strong Balmer break. The spectrum has strong Balmer absorption lines (best illustrated in the middle panel) typical of spectral type A stars (life time ~ 1 Gyr). The lack of emission lines and the flat ultraviolet spectrum are consistent with no current star formation. This implies that the galaxy has experienced a recent starburst, and stellar population synthesis indicates a young stellar population of 0.4 Gyr.

gions (LINER, Kriek et al. 2009a). The LINER emission is again observed in more recent studies (Belli et al., 2014a), and is as a hint that active galactic nuclei may be responsible for suppressing star formation in quiescent galaxies.

1.2 The observed evolution of the quiescent galaxy population

More galaxies become quiescent, but fewer are compact

Through tracing the redshift evolution of the stellar mass function (Ilbert et al., 2010; Marchesini et al., 2009; Brammer et al., 2011; Ilbert et al., 2013; Muzzin et al., 2013), the fraction of quiescent galaxies increases over time as illustrated in the bottom panel of Figure 1.3 (left). This is a result of star-forming galaxies becoming quenched, therefore adding to the quiescent galaxy population at $z \sim 1$. At $z \sim 1.5$, half of the massive galaxies with $M_\star > 10^{11} M_\odot$ are quiescent.

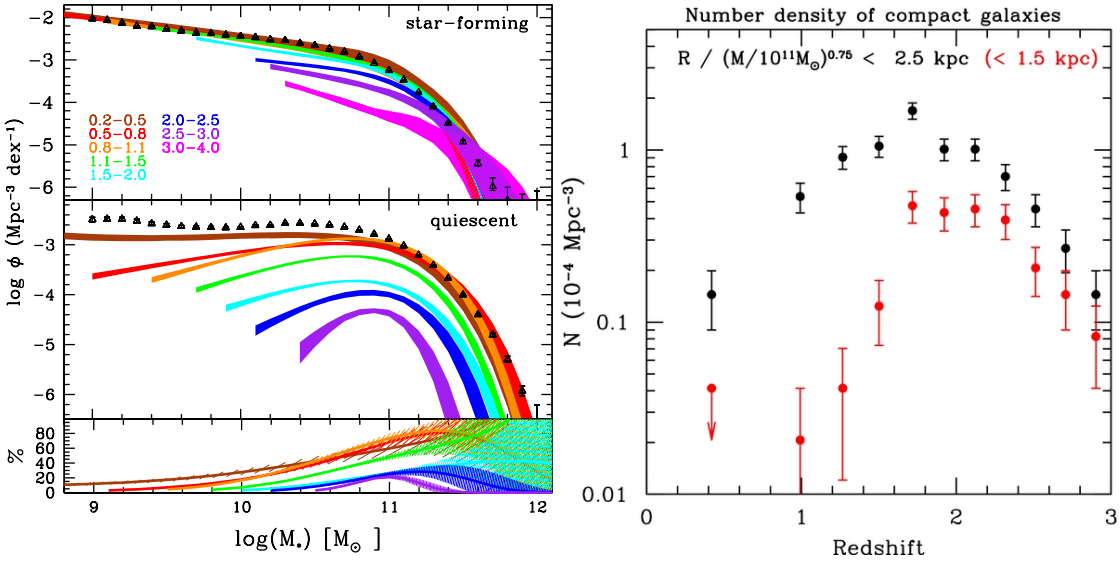

Figure 1.3: ***Left:*** The stellar mass function of star-forming (top) and quiescent (middle) galaxies at different redshifts (color-coded), presented in Ilbert et al. (2013). The bottom panel shows the quiescent fraction of galaxies. ***Right:*** The number densities of quiescent galaxies that are more compact than 2.5 kpc (black) and 1.5 kpc (red), as a function of redshift (van der Wel et al., 2014). The number density increases from $z \sim 3$ to $z \sim 1.8 - 2.2$, and diminishes drastically towards $z \sim 1$. This argues for the need of individual size evolution among quiescent galaxies to explain their "disappearance".

The wide-field WFC3 survey, CANDELS, provides sufficiently large samples of massive compact quiescent galaxies to trace their number density evolution. Specifically, these compact galaxies must disappear over a brief period from $z \sim 2$ to $z \sim 1$

(Szomoru et al. 2012; van der Wel et al. 2014; van Dokkum et al. 2014, right panel of Figure 1.3), which is evidence for the need to increase the sizes of quiescent galaxies already in place since $z \gtrsim 2$.

LARGER SIZES, MORE SPHEROID-LIKE

On average, the sizes of quiescent galaxies grow by a factor of 3 – 5 from $z \sim 2.5$ to $z \sim 0$ (Newman et al., 2012; van der Wel et al., 2014), while the size scatter and mass-dependence remains relatively constant with redshift (Figure 1.4). Apart from the apparent size growth, their structures also evolve from more disk-like at $z \sim 2$ towards more spheroid-like at $z \sim 0$, as reflected in their increasing Sersic indices and projected axial ratios with time (van der Wel et al., 2011; Chang et al., 2013). It remains an open question how, in the absence of further star formation, quiescent galaxies can grow rapidly in size and structures to become their present day descendants, the giant ellipticals.

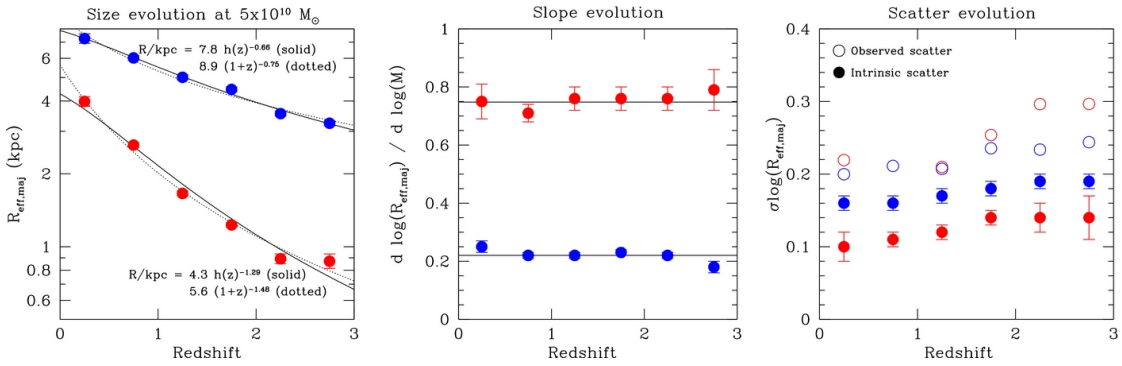

Figure 1.4: The size evolution of quiescent galaxies (red) more massive than $5{\times}10^{10} M_{\odot}$ as measured in the CANDELS survey (van der Wel et al., 2014). The left panel shows the size as a function of redshift, the middle panel shows the slope evolution of the size-mass relation, and the right panel shows the size scatter. When compared to star-forming galaxies (late-type, blue), quiescent (early-type) galaxies evolve faster in size (steeper slope, $R \propto (1+z)^{-1.48}$), while the size scatters for both populations are small ($\lesssim 0.2$ dex) and relatively constant in time.

LIGHT AND STELLAR MASS PROFILE

The superior resolution of WFC3 can resolve quiescent galaxies (down to ~ 1 kpc), enabling measurements of the radial dependence of colors and stellar mass. Szomoru et al. (2011) presented rest-frame $u-g$ color gradient measurements, and found that quiescent galaxies have negative color gradients (red cores, blue outskirts), a trend persistent out to $z \sim 2$. Without spectroscopic information, it is difficult to conclude that the redness of the cores are solely due to old stellar ages instead of dust attenuation. How-

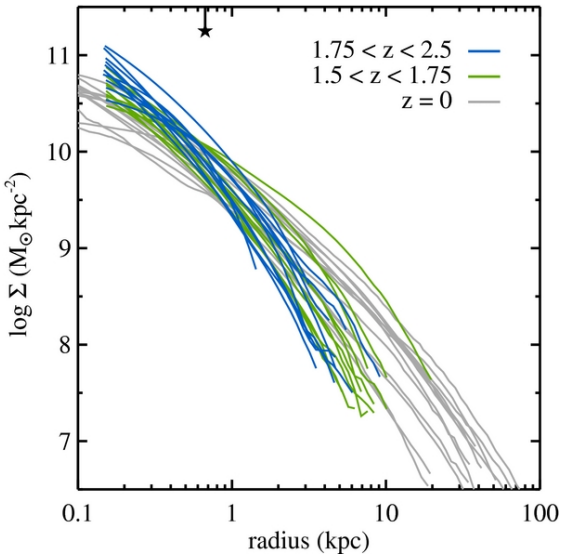

Figure 1.5: The stellar mass profile of quiescent galaxies at $z > 1.5$ (colored lines) compared to $z \sim 0$, presented in Szomoru et al. (2012). The mass densities of quiescent galaxies do not evolve strongly within the central kpc (given the imaging point spread function indicated as the star on the top x-axis), and furthermore it is evident that they must gain addition stellar mass in the outskirts over time.

ever, since quiescent galaxies are presumably no longer actively forming stars, they are expected to be relatively dust-free. In conjunction with the required mass growth in galaxy outskirts through studying the stellar mass profiles (Figure 1.5, Szomoru et al. 2012, 2013), these results support the "inside-out growth" scenario: dense galaxy cores form first (as discussed in Section 1.1), and satellites with younger ages are disrupted during their in-fall, and subsequently accreted onto the outskirts of the massive hosts.

Correlation between structure and star formation rate

Quiescent galaxies at $z \sim 2$ are distinct from star-forming galaxies in terms of structure and star formation activity, as illustrated in Figure 1.6. As further illustrated in Figure 1.7, massive and quiescent galaxies tend to be more spheroid-like (i.e. higher Sersic indices) than star-forming and/or lower mass galaxies. a trend persistent out to $z = 2.5$. This supports that the Hubble sequence at $z \sim 0$ (red sequence and blue cloud, leftmost panel in Figure 1.7) is in fact already in place by $z \sim 2$ (Kriek et al., 2009b; Williams et al., 2009, 2010; Conselice et al., 2011; Szomoru et al., 2011; Wuyts et al., 2011; Cassata et al., 2013). It is therefore speculated that the mechanism that quenches star formation also alters the morphology of galaxies, and that this mechanism is already in place at early epochs.

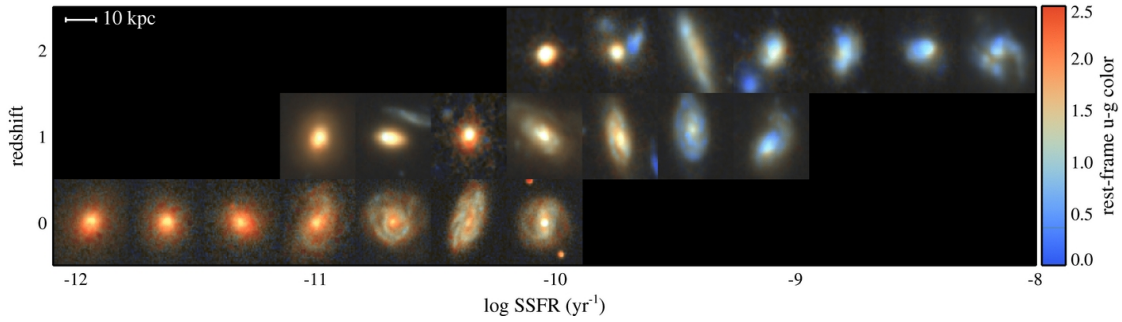

Figure 1.6: The relation between specific star formation rates (sSFR; x-axis) and structures, as a function of redshift (y-axis), presented in Szomoru et al. (2011) with WFC3 observations. From $z \sim 2$ to 0, galaxies become redder and have lower sSFR on average. At any epoch, star-forming galaxies tend to be more extended (see also Figure 1.4), disk-like and clumpy than quiescent galaxies.

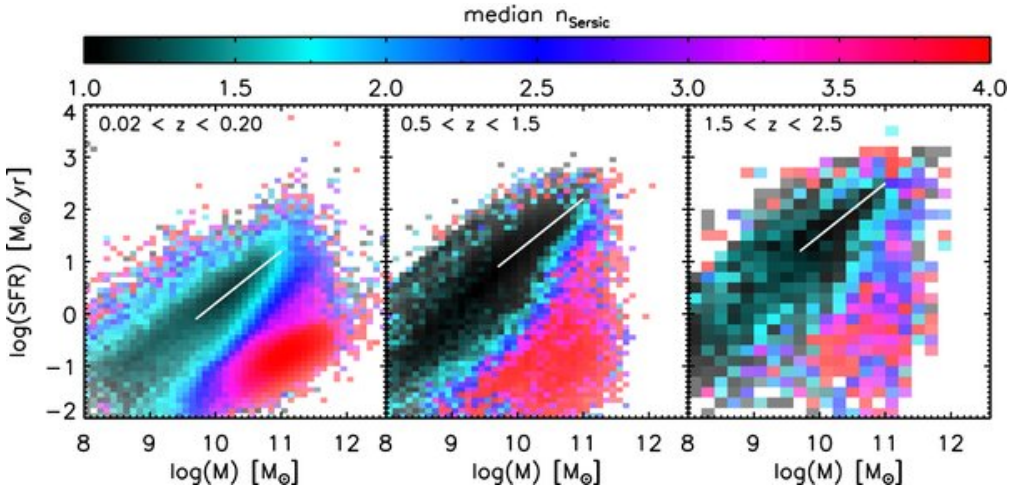

Figure 1.7: The star formation rate - stellar mass relation for galaxies at different redshifts (panels), color-coded by the Sersic indices (Wuyts et al., 2011). Red color represents spheroid-like galaxies, and blue color represents disk-like galaxies. The star-forming and quiescent galaxies are structurally distinct out to $z \sim 2.5$, suggesting that the mechanism leading to the transition from the blue cloud to the red sequence alters both the morphology and the star formation activity simultaneously.

1.3 THE ROLE OF MERGING IN EVOLVING QUIESCENT GALAXIES

If quiescent compact galaxies at $z \sim 2$ are to evolve into present-day giant ellipticals (last three steps in Figure 1.1), they would have to acquire stellar mass in the outskirts through merging (Figure 1.5). Hierarchical assembly is a direct prediction of the Λ

Cold Dark Matter model (White & Frenk, 1991; Kauffmann & White, 1993), whereby large galaxies are assembled from merging smaller ones.

Galaxy merging, in particular gas-poor dissipationless ones, remains a popular explanation for the observed size and Sersic index growth in quiescent galaxies. Minor mergers, conventionally defined as having mass ratios of 1:4 – 1:10, are expected to be more efficient in puffing up the sizes of galaxies compared to major mergers (mass ratios 1:1 – 1:4), per unit mass added. This is derived from the virial theorem, and later verified by more sophisticated merger simulations (Khochfar & Silk, 2006; Hopkins et al., 2009b; Bezanson et al., 2009; Naab et al., 2009; Nipoti et al., 2009; Oser et al., 2010, 2012; Hilz et al., 2012, 2013). The merger-driven size growth is illustrated along with the expected Sersic index growth in Figure 1.8.

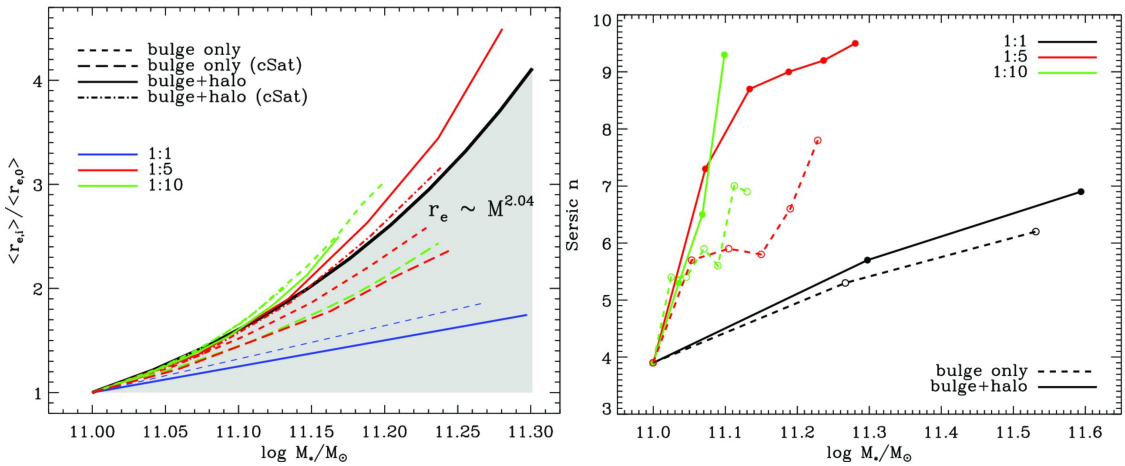

Figure 1.8: The predicted structural changes due to 1:1 (blue), 1:5 (red) and 1:10 (green) mergers from the simulations of Hilz et al. (2013), after doubling the stellar mass through merger(s). ***Left:*** Size growth is more efficient (per unit mass added) in unequal-mass mergers than equal-mass mergers. Interestingly, intermediate (1:5) mass ratio mergers are equally efficient as minor (1:10) mass ratio mergers. ***Right:*** The expected Sersic index evolution due to different mass ratio mergers. A milder increase in the Sersic index is expected for equal-mass mergers, compared to more extreme mass ratios.

Although galaxy merger is a *viable* mechanism for the size evolution of quiescent galaxies, it remains unclear whether the observed merger rates are sufficient to be fully accountable. The required size growth is most rapid at $z \sim 1-2$ (Newman et al., 2012), yet existing merger rate measurements are discrepant (Bluck et al., 2009; Williams et al., 2010; Man et al., 2012). In Chapters 2 and 3, we present two galaxy merger fraction measurements based on state-of-the-art observations.

In Chapter 2, we present measurements of the galaxy major merger fraction and rate out to $z \sim 3$ using *HST*/NICMOS data (Man et al., 2012). It was one of the largest *HST* merger samples out to $z \sim 3$, and we show that the major merger fraction of

massive galaxies has a mild redshift dependence. This is contradictory to the steep redshift evolution as claimed by Bluck et al. (2009), as well as a diminishing redshift dependence by Williams et al. (2010). The small sample size (~ 60 mergers at $z = 0 - 3$ for Bluck et al. 2009 and Man et al. 2012, respectively) precludes a conclusions as to why the measurements were discrepant with one another.

In Chapter 3, we describe a more extensive study using the UltraVISTA and CANDELS catalogs, and present the largest photometrically selected galaxy (> 1000 major + minor) mergers out to $z = 3$ (Man et al., 2014). We resolve the discrepancy of the existing galaxy merger fraction measurements at $z \gtrsim 2$. Selecting mergers by stellar mass ratio leads to a declining redshift evolution, while selecting by the H-band flux ratio leads to an increasing one. This is due to the strong redshift evolution of the mass-to-light ratios among satellite galaxies. We discuss the implications of the observed galaxy merger rates on the mass and size growth of quiescent galaxies.

1.4 Are quiescent galaxies really passively evolving, or dusty starbursts?

The quiescence of the galaxies are established through their flat ultraviolet continuum slope, as discussed in Section 1.1. However, significant dust attenuation in star-forming galaxies can mimicking the redness of evolved stellar populations, as shown in Figure 1.9. Various rest-frame color selection techniques ($U - V$ and $V - J$, Williams et al.

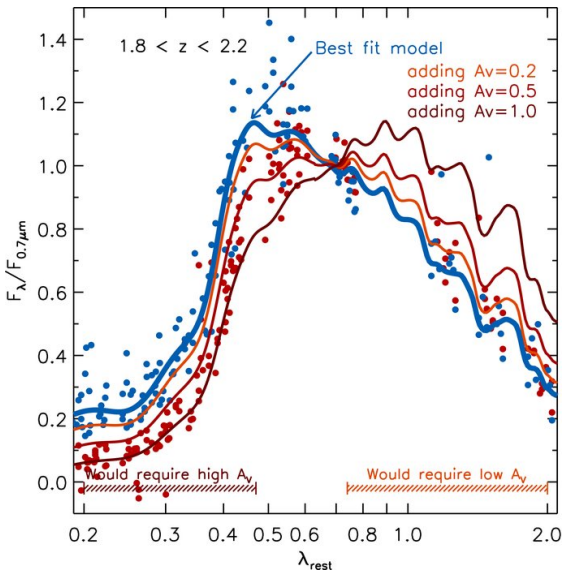

Figure 1.9: The spectral energy distribution of star-forming galaxies (blue), and the effect of applying various levels of dust extinction (orange – brown) as presented in Whitaker et al. (2010).

2010; $NUV - r$ and $r - K$, Arnouts et al. 2013; $NUV - r$ and $r - J$, Ilbert et al. 2013) are designed to separate dusty star-forming galaxies from quiescent ones. The $U - V$ and the $NUV - r$ colors trace the ultraviolet emission by young stars. The second color lies in the redder part of the spectrum, therefore is more sensitive to the underlying stellar populations and less affected by dust attenuation. As shown in Figure 1.10, the bicolor selection works considerably well in separating the two populations at least out to $z = 1.5$. However, rest-frame colors become much more uncertain at $z > 1.5$ due to cosmic dimming, and the two populations are no longer clearly distinguishable.

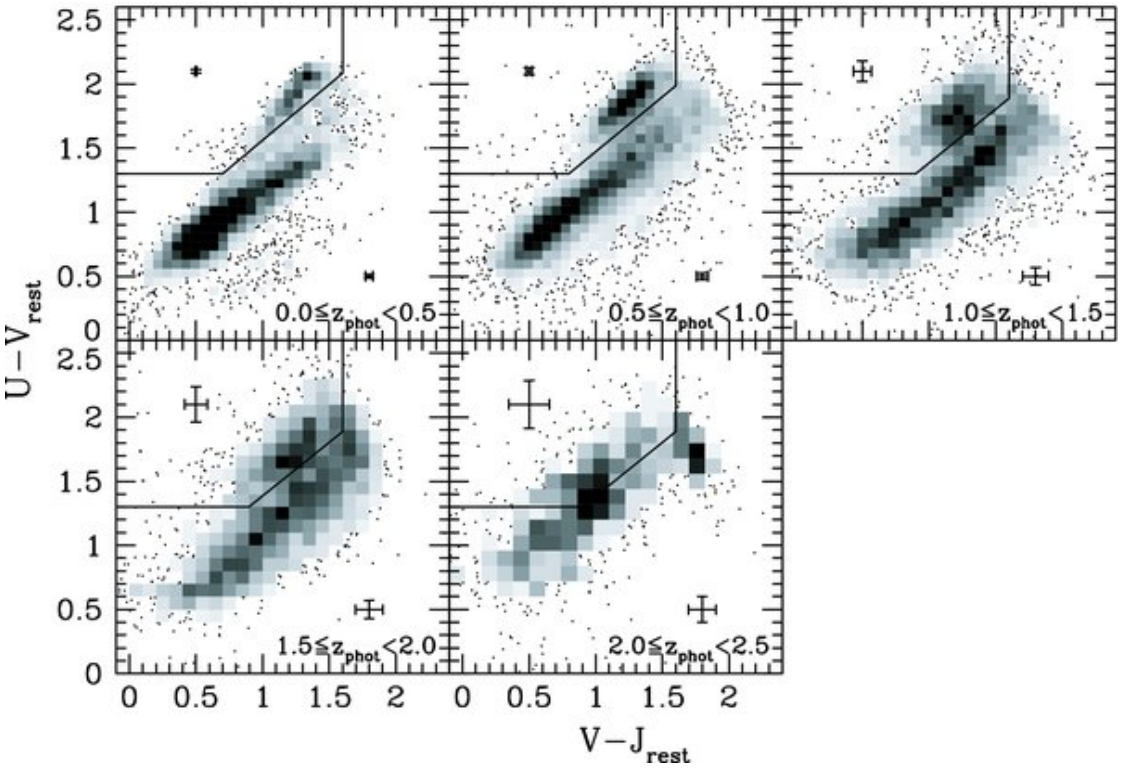

Figure 1.10: The rest-frame $U - V$ and $V - J$ colors for separating quiescent galaxies (top left corner) from star-forming galaxies (Williams et al., 2010). The top right corner is occupied by dusty star-forming galaxies that would have been selected as quiescent, if only a single $U - V$ color was used. The typical uncertainties are shown as crosses. It is apparent that the color selection clearly separates the two sequences out to $z = 1.5$. Beyond $z \sim 1.5$, the rest-frame colors become considerably more uncertain, and the two sequences are no longer easily distinguishable.

In order to verify whether the bicolor selections are successful in identifying quiescent galaxies without obscured star formation, infrared observations that probe the dust-reprocessed emission are required. Typically, the existing mid-infrared (*Spitzer* MIPS 24μm) and far-infrared maps are only deep enough to detect strong starburst

galaxies at $z > 1$. When large samples of massive galaxies become available from wide-field surveys, stacking is utilized to reduce the noise background and determine the average infrared emission in galaxies. Two teams (Fumagalli et al., 2013; Utomo et al., 2014) performed median stacking for the 24μm maps on two samples of quiescent galaxies out to $z \sim 2.5$. They found that quiescent galaxies do not host strong dust-obscured star formation (SFR $< 10 M_{\odot}\mathrm{yr}^{-1}$). However, dust heating by evolved stellar populations may contribute significantly to the infrared emission of quiescent galaxies. On the other hand, Viero et al. (2013) performed mid- and far-infrared stacking on the *Spitzer* 24μm, *Herschel* PACS+SPIRE and AzTec 1100μm maps for a larger sample of quiescent galaxies. Surprisingly, they found that massive quiescent galaxies at $z > 2$ are comparable to local starbursts on average, and have $L_{\mathrm{IR}} > 10^{12} L_{\odot}$. This contradicts the quiescence of galaxies indicated by their flat ultraviolet continua, as well as the 24μm stacking results. If quiescent galaxies were in fact dust-obscured starbursts, it would challenge the need for aggressive feedback mechanisms to suppress star formation (e.g., Bower et al., 2006; Croton et al., 2006).

In light of the discrepancy in the existing measurements and its strong implications, in Chapter 4 we present a mid-, far-infrared and radio stacking analysis for quiescent galaxies in COSMOS selected by the $NUV-r$ and $r-J$ colors. The sample contains ∼14 200 quiescent galaxies, representing the largest sample used in similar studies in order to reach higher signal-to-noise in the stacks. The simultaneous coverage by Spitzer, *Herschel* and the Very Large Array allow for three independent star formation rate measurements. The multi-wavelength coverage of COSMOS enables active galactic nuclei to be identified by their detections at X-ray, mid-infrared (IRAC power law) and radio (Very Large Array), in order to study any systematic effects.

2

How often do galaxies merge?

The Pair Fraction of Massive Galaxies at $0 \leq z \leq 3$

Allison W. S. Man[1], Sune Toft[1], Andrew W. Zirm[1], Stijn Wuyts[2], and Arjen van der Wel[3]

[1] Dark Cosmology Centre, Niels Bohr Institute, University of Copenhagen
[2] Max-Planck-Institut für Extraterrestrische Physik, Germany
[3] Max-Planck Institut für Astronomie, Germany

Published in the Astrophysical Journal, vol. 744, pp. 85–91, 2012

Abstract

Using a mass-selected ($M_\star \geq 10^{11} M_\odot$) sample of 198 galaxies at $0 \leq z \leq 3$ with *HST*/NICMOS H_{160}-band images from the COSMOS survey, we find evidence for the evolution of the pair fraction above $z \sim 2$, an epoch in which massive galaxies are believed to undergo significant structural and mass evolution. We observe that the pair fraction of massive galaxies is 0.15 ± 0.08 at $1.7 \leq z \leq 3.0$, where galaxy pairs are defined as massive galaxies having a companion of flux ratio from 1:1 to 1:4 within a projected separation of 30 kpc. This is slightly lower, but still consistent with the pair fraction measured previously in other studies, and the merger fraction predicted in halo-occupation modelling. The redshift evolution of the pair fraction is described by a power law $F(z) = (0.07 \pm 0.04) \times (1+z)^{0.6 \pm 0.5}$. The merger rate is consistent with no redshift evolution, however it is difficult to constrain due to the limited sample size and the high uncertainties in the merging timescale. Based on the merger rate calculation, we estimate that a massive galaxy undergoes on average 1.1 ± 0.5 major merger from $z = 3$ to 0. The observed merger fraction is sufficient to explain the number density evolution of massive galaxies, but insufficient to explain the size evolution. This is a hint that mechanism(s) other than major merging may be required to increase the sizes of the massive, compact quiescent galaxies from $z \sim 2$ to 0.

2.1 INTRODUCTION

The sizes of quiescent massive galaxies at $z \sim 2$ are shown to be on average 3 - 6 times smaller compared to galaxies of similar mass at $z = 0$ (Daddi et al., 2005; Trujillo et al., 2006a,b; Toft et al., 2007; Trujillo et al., 2007; Zirm et al., 2007; Buitrago et al., 2008; Cimatti et al., 2008; Franx et al., 2008; van Dokkum et al., 2008; Toft et al., 2009; van Dokkum et al., 2010; Targett et al., 2011). High-resolution cosmological simulations confirm the compactness of massive galaxies at $z \sim 2$ compared to local counterparts (Sommer-Larsen & Toft, 2010). The question is then: what are the physical processes that drive the drastic size evolution of massive quiescent galaxies between $0 < z < 2$?

At $z \sim 2$, merging is an important process for the evolution of galaxies, in terms of mass (van Dokkum et al., 2010) and size: Khochfar & Silk (2006) demonstrate with their semi-analytical model that the observed redshift-size evolution of elliptical galaxies may be a consequence of the available amount of cold gas during the major merger. Furthermore, van der Wel et al. (2009b) suggest that major merging is the most important mechanism to produce massive, quiescent galaxies through studying the distribution of the projected axial ratio of galaxies from the Sloan Digital Sky Survey. On the other hand, there is evidence from observations (Bezanson et al., 2009) and simulations (Naab et al., 2009) that minor mergers are more common than major mergers and could be the dominant driver for the inferred size evolution. Most of the luminous red elliptical galaxies at $z < 1$ are assembled through gas-poor (i.e. dry) merging (Bell et al., 2004; van Dokkum, 2005; Bell et al., 2006b). The high fraction ($\sim 50\%$, Kriek et al. 2006b, 2008; Williams et al. 2009) of massive galaxies at $z \sim 2$ that are quiescent and have old stellar populations suggests that dry mergers may be common since that epoch until $z = 0$. However, it is likely that dry mergers can only account for a factor of ~ 2 of growth in size from $z \sim 2$ to 0 (Nipoti et al., 2009).

Additionally, gas-rich mergers have been shown to drive gas towards the central supermassive black holes and possibly trigger the active galactic nuclei, releasing enough energy to expel the gas and thereby quenching star formation (Di Matteo et al., 2005). The gas inflow can also enhance star formation and even fuel starbursts (Barnes & Hernquist, 1991; Mihos & Hernquist, 1994). The merging between two disk-like galaxies can form an elliptical, as predicted in simulations (Toomre & Toomre, 1972; Barnes & Hernquist, 1996). Although if the merging is highly dissipational, a larger degree of rotation and therefore flattening of the remnant may be expected (Naab et al., 2006; Robertson et al., 2006; Wuyts et al., 2010). Recently, van der Wel et al. (2011) present evidence for the dominance of such disk-like morphologies in quiescent systems at $z \sim 2$.

Through studying the abundance of mergers of massive galaxies across redshift, we can place constraints on the current evolutionary model of these galaxies. Substantial work exists in the literature regarding the merger fraction of galaxies at $z < 1.2$: merger samples can either be constructed via pair selection (Zepf & Koo, 1989; Carlberg et al.,

1994; Le Fèvre et al., 2000; Patton et al., 2000; Lin et al., 2004; Kartaltepe et al., 2007; Lin et al., 2008; Bundy et al., 2009; Robaina et al., 2010) or morphological selection (Le Fèvre et al., 2000; Conselice et al., 2003; Lotz et al., 2008b; McIntosh et al., 2008; Heiderman et al., 2009; Jogee et al., 2009). Kinematic evidence suggests that not all irregular morphologies at high redshift are related to mergers (Förster Schreiber et al., 2009, 2011). Hence, it is not straightforward to identify mergers through morphological classification and we focus on using pair counts as a probe for merging activity in this Paper. It has been challenging to establish large samples of pairs of massive galaxies at $z > 1$. High-resolution near-infrared (NIR) imaging is required to probe the rest-frame optical emission from the stellar populations. Large-area NIR surveys have only begun recently (e.g., the CANDELS survey (Grogin et al., 2011; Koekemoer et al., 2011), the 3D-HST survey (van Dokkum et al., 2011)). There are only few spectroscopically confirmed mergers at $z > 1.5$ (Shapiro et al., 2008; Law et al., 2011). Attempts to constrain the pair fraction at higher redshifts are limited to targeted observations (Bluck et al., 2009). The selection criteria of massive galaxies and pairs vary across studies, posing a challenge to make a uniform comparison of the pair fractions.

The aforementioned observations compare the observed pair fraction with the predicted merger fraction from cosmological simulations, combined with semi-analytical models (e.g., Somerville et al. 2008; Bertone & Conselice 2009; Hopkins et al. 2010d) or semi-empirical models using the halo occupation distribution (Hopkins et al., 2010b). The potential caveat is that these simulations are closely tied to observations, often normalized to reproduce the statistical observables such as the mass function, the luminosity function, and the correlation function of galaxies.

This Paper uses a sample of 198 massive ($M_\star \geq 10^{11} M_\odot$) galaxies at $0 \leq z \leq 3$ with high-resolution NIR imaging. The sample is drawn from the Cosmic Evolution Survey (COSMOS) where parallel imaging from the Near-Infrared Camera and Multi-Object Spectrograph (NICMOS) onboard the *Hubble Space Telescope (HST)* is available, in order to probe their rest-frame optical morphology, offering the novel opportunity to derive the pair fraction of a mass-selected sample across a wide redshift range with robust photometric redshifts (photo-z's) and masses derived from spectral energy distribution (SED) fitting.

The Paper is organized as follows: in §4.2 we describe the photometric catalog, the quantities derived and the completeness of the catalog; the selection of galaxy pairs and the correction for projection contamination are also discussed. In §2.3 the results of the analysis are detailed: we compare our pair fractions with other observations and model predictions, and estimate the effect of mass completeness on the pair fraction. We also explore the impact of merging on the growth of the massive galaxy population: the merger rates are calculated and the predicted number growth is compared with the observed number densities of massive galaxies. Implications on our current under-

standing of massive galaxy formation are discussed. The conclusions are outlined in §3.5.

All magnitudes are quoted in the AB system, unless otherwise stated. A cosmology of H_0 = 70 km s^{-1} Mpc^{-1}, $\Omega_{\rm M}$ = 0.3 and Ω_Λ = 0.7 is adopted throughout the Paper.

2.2 DATA: CATALOG AND SELECTION

The COSMOS field (Scoville et al., 2007a) provides photometry in 30+ bands over an area of $>$ 2 deg^2, including imaging from the Advanced Camera for Surveys (ACS). The *HST*/NICMOS Camera 3 (NIC3) non-contiguously covers $\sim$ 5 % (332 arcmin^2) of the field, with 5σ depth of $H = 25.6$ for point sources. The NIC3 imaging is used with the $F160W$ filter, and the drizzled images have a pixel scale of 0.101″/pix and a FWHM PSF of $\sim$ 0.25″. In our analysis we use the NIC3 images from the COSMOS Archive[1] reduced by James Colbert.

2.2.1 INPUT CATALOG

The analysis of this Paper is based on the public COSMOS 30+ band catalog, combined with the H-band photometry by Gabasch et al. (2008), and the IRAC photometry from sCOSMOS. The parent catalog (Ilbert et al., 2009) is selected in the i-band (from Subaru Suprime-Cam), where fluxes are measured within apertures of 3″ in diameter and has a limiting magnitude of $i < 26$. The resulting photometric catalog is compiled from all public data in narrow-, medium- and broad-bands covering wavelengths in UV, optical, NIR and mid-IR, and has a limiting magnitude of $K < 23.86$.

2.2.2 DERIVED QUANTITIES

Photo-z's are derived on all entries using the medium- and broad-band catalog with the code EAZY (Brammer et al., 2008). The IRAC fluxes have been downweighted by EAZY in the fitting using a template error function. For sources with $K_{\rm Vega} < 22$, we model the SED in the same way as in Wuyts et al. (2007), in order to estimate the stellar masses. We make use of the BC03 (Bruzual & Charlot, 2003) stellar population synthesis model with the FAST code (Kriek et al., 2009c), assuming a Chabrier initial mass function (IMF), and fit the SEDs with three different star formation histories: a single stellar population without dust, an exponentially declining model with *e*-folding time of 300 Myr and dust attenuation allowed to be between $A_{\rm v}$ = 0-4, and a constant star formation model with the same range in attenuation. We assume solar metallicity and the Calzetti et al. (2000) extinction law.

[1] http://irsa.ipac.caltech.edu/data/COSMOS/images/nicmos/

2.2.3 SELECTION OF MASSIVE GALAXIES IN PAIRS

2.2.3.1 Parent sample of massive galaxies and mass completeness

We select galaxy pairs by searching for companions to the massive galaxies in the NICMOS parallels. The parent sample consists of 5,299 massive galaxies of $M_\star \geq 10^{11}\ M_\odot$ at $0 \leq z \leq 3$ in the COSMOS field. The photo-z's are required to have `odds` ≥ 0.95 such that they have $\geq$ 95% integrated probability of lying within Δz = 0.2 of the estimate. The χ^2-value of the SED modelling is required to be less than 10. The `odds` and the χ^2 criteria reject approximately 55% and 17% of all the sources at $0 \leq z \leq 3.0$ in the whole COSMOS catalog, ensuring robustness in the photo-z's and masses.

To estimate the completeness of our adopted mass limit of $M_\star \geq 10^{11}\ M_\odot$ from our i-band selected catalog, we compare the selected galaxies to the K-band selected FIRE-WORKS catalog (Wuyts et al., 2008) for GOODS-Chandra Deep Field South (CDFS), which has a deeper limiting magnitude of $i = 27$ (3σ). As the completeness is a strong function of redshift, we compare the magnitude distribution of massive galaxies in COSMOS and CDFS against redshift in Figure 2.1. Assuming that CDFS is 100% complete in selecting massive galaxies, the completeness limit of COSMOS are 100%, 75% and 44% for the redshift bins 0-1.7, 1.7-2.3 and 2.3-3.0 respectively. Only 7% and 14 % of the massive galaxies are rejected by the `odds` and the χ^2 criteria, so the incompleteness is mostly due to the faintness of the massive galaxies in the i-band.

There are 305 massive galaxies in the parent sample which have NICMOS H_{160} parallels, but 109 of those are in the edge region of low signal to noise, so there are 196 galaxies with usable NICMOS imaging.

Selection of galaxy pairs We run `SExtractor` Version 2.8.6 (Bertin & Arnouts, 1996) on the $10'' \times 10''$ NICMOS cutouts (or $35'' \times 35''$ for galaxies at $0 \leq z \leq 1.0$), with parameters optimized to ensure that sources are deblended properly. The isophotal fluxes are used to compute the H-magnitude of each source. Due to the large photometric aperture used in the COSMOS catalog, 22 cutouts have more than one source within the 3″-aperture, where the source-confused companions have no separate entry in the catalog. In these cases the photo-z of the companion is assigned to be the same as the primary massive galaxy, and the integrated best-fit masses are adjusted using the NICMOS H-band flux ratio from `SExtractor`. The final massive galaxy sample consists of 198 massive ($M_\star > 10^{11} M_\odot$) galaxies at $0 \leq z \leq 3$, where all of them are brighter than the depth of the NICMOS imaging described in §4.2. Note that there are two more massive galaxies compared to the 196 massive galaxies mentioned in §2.2.3.1. This is because there was source confusion in the photometry of two of the selected massive galaxies, and after mass correction there are two massive galaxies on each cutout (four massive galaxies in total).

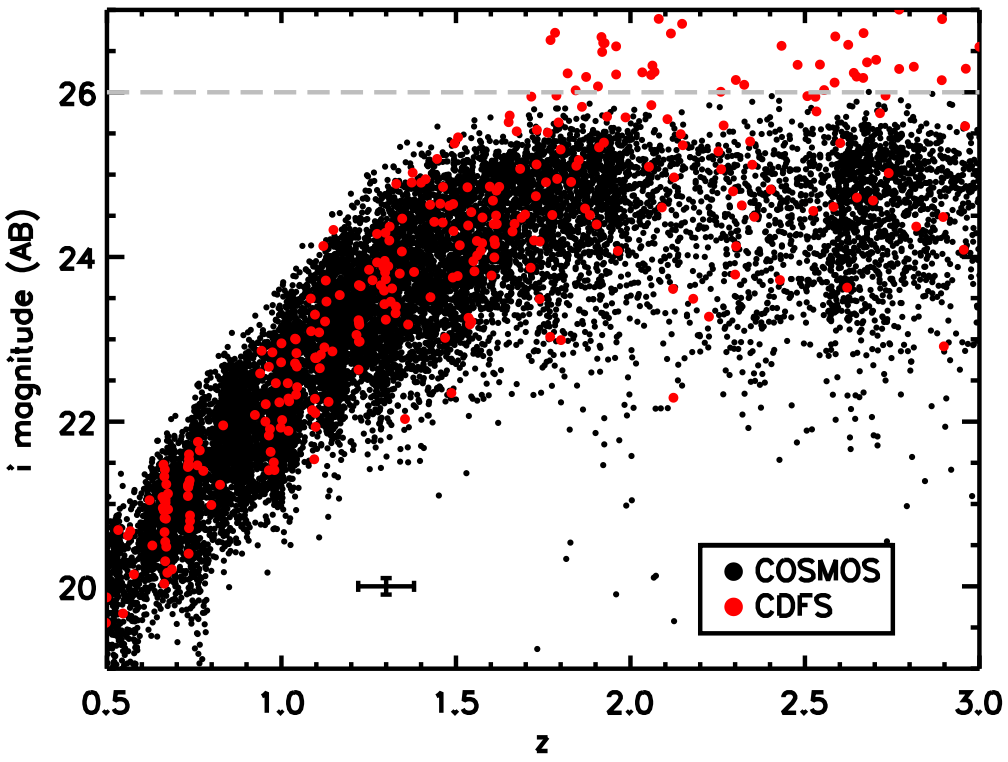

Figure 2.1: Mass completeness of the catalog. Galaxies above our mass limit of $M_\star \geq 10^{11} M_\odot$ in COSMOS (black) and CDFS (red) are plotted. The gray dashed line shows the approximate depth of the COSMOS data. The typical uncertainties in magnitudes and photo-z's are overplotted at the bottom left corner.

Galaxy pairs are selected from the massive galaxies sample using the following criteria: (1) the massive galaxy has one or more companion within a projected separation of 30 kpc; and (2) the H_{160}-flux ratio of the pair is between 1:4 to 1:1. Imposing these criteria we find 40 massive galaxies in pairs (N_{obs}), in the redshift range of $0 \leq z \leq 3$. Almost all (99%) of the massive galaxies are bright enough such that if they have 1:4 companions, the companions are brighter than the depth of NICMOS ($H = 25.6$, see §4.2). Only two massive galaxies (1%) are fainter than $H = 25.6$, but they are retained in the sample because they have companions detected with NICMOS. The number of galaxies having companions of flux ratio above 1:2 / 1:3 / 1:4 is 20 / 32 / 40 respectively. Examples of the cutouts are shown in Figure 2.2. We note that there are two galaxy pairs in which both of the merging galaxies are massive ($M_\star > 10^{11} M_\odot$).

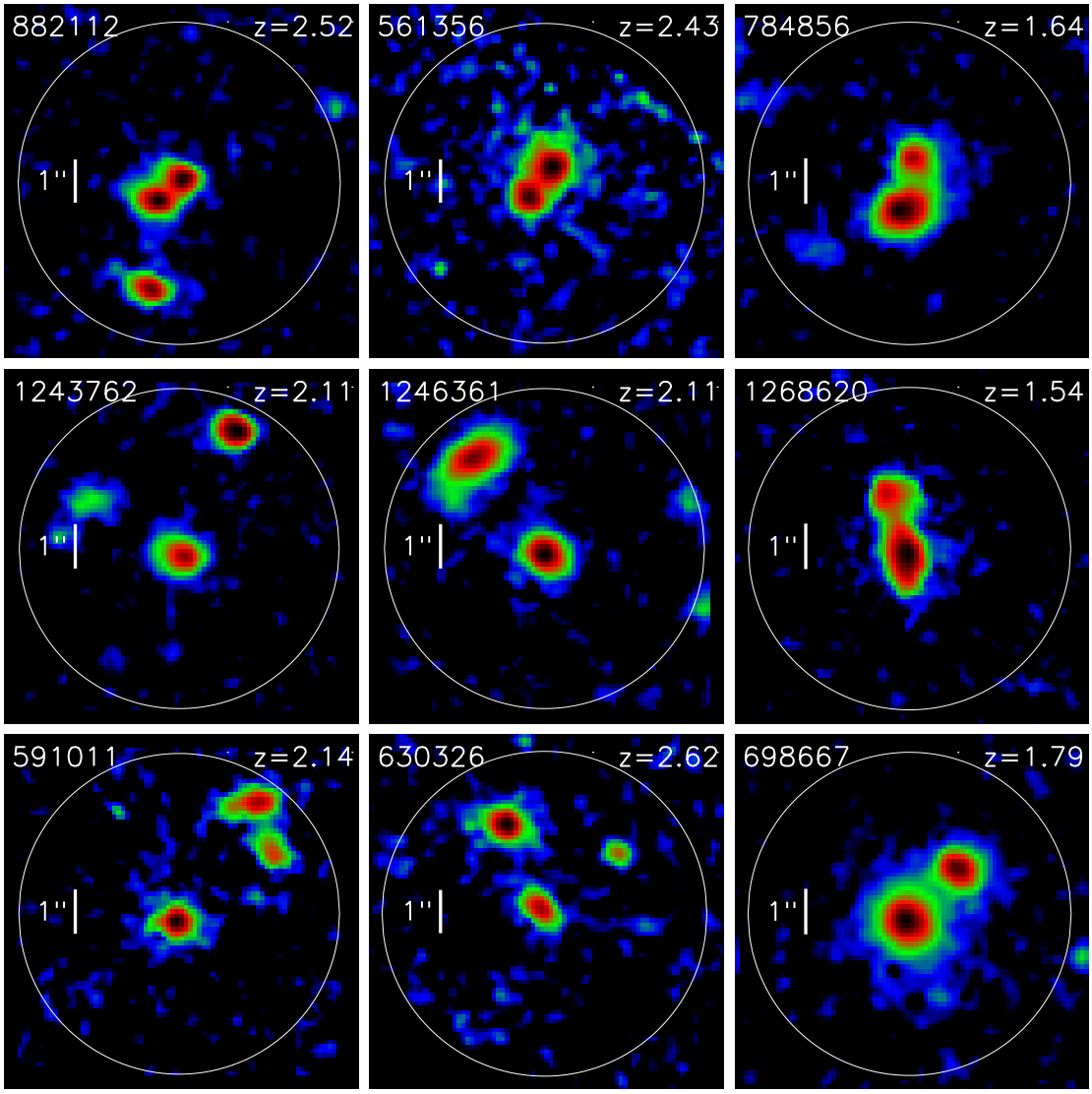

Figure 2.2: The NICMOS H_{160} postage stamps of nine examples of the selected galaxy pairs. The top row shows pairs that were source-confused in the original COSMOS catalog, but are now resolved in our analysis with the NICMOS imaging; the bottom two rows contain pairs that have individual entries in the catalog. The IDs and photo-z's of the massive galaxies are labelled on the top left and right hand corners of each panel. For illustrative purpose, the colour coding is scaled logarithmically and the images are smoothed by convolving with a Gaussian PSF of FWHM = 2 pixels ($0.202''$). The angular scale is shown with the $1''$ vertical bar. The white circle overlaid on each map indicates the 30-kpc search radius around each massive galaxy at the centre.

Table 2.1. Pair fraction and merger rate across redshifts

Redshift range	**M (N_{obs})**	**$<N_{projected}>$**	**Pair fraction**	**Merger rate $\Re(z)$** [$\times 10^4$ Gpc^{-3} Gyr^{-1}]
$0 \leq z \leq 1.0$	69 (8)	2.4	0.08 ± 0.05	12.0
$1.0 \leq z \leq 1.7$	70 (12)	5.2	0.10 ± 0.06	7.7
$1.7 \leq z \leq 2.3$	37 (12)	5.9	0.17 ± 0.11	9.2
$2.3 \leq z \leq 3.0$	22 (8)	5.4	0.12 ± 0.15	5.6
$1.7 \leq z \leq 3.0$	**59 (20)**	**11.3**	**0.15 ± 0.08**	

Note. — M is the number of massive galaxies, N_{obs} is the number of galaxies in pairs, and $<N_{projected}>$ is the expected number of galaxies in projected pairs.

2.2.3.2 Correcting for chance projection

Before comparing the pair fraction with model predictions and investigating its redshift evolution, it is necessary to subtract the contamination from projected galaxy pairs at different redshifts. We estimate the effect of chance projection by performing a Monte-Carlo simulation, assuming that there is no clustering in the sources or the massive galaxies. All COSMOS sources are redistributed randomly over the effective (unmasked) area of the COSMOS field. The 198 massive galaxies in the sample are also assigned random positions. Using their photo-z's we count, within an annulus of 5-kpc to 30-kpc, the number of close companions that have magnitudes down to 1:4 fainter. We repeat the redistribution and counting for 500 realizations. The average of the counts are taken as the expected number of galaxies in projected pairs ($< N_{projected} >$) for each redshift bin, and are listed in Table 2.1. It can be seen that approximately half of the observed pairs are random projections. We also note that the correction is more significant at higher redshift. This is because high-z galaxies are fainter and the surface number counts are higher for faint galaxies, resulting in a higher probability of chance projection. Law et al. (2011) find a similar correction for chance projection ($\sim 50\%$) using spectroscopic redshifts available for 2874 star-forming galaxies at $1.5 < z < 3.5$.

In each redshift bin, we observe M massive galaxies and N_{obs} of them are in pairs. The fraction of galaxies in pairs (f_p), or pair fraction for short, is calculated as:

$$f_p = \frac{\mathrm{N_{obs}} - < \mathrm{N_{projected}} >}{\mathrm{M}}$$

The errors in f_p are estimated by the Poisson uncertainties of $\mathrm{N_{obs}}$.

Alternatively, as photo-z's are available for 68% of the companions and all of the massive galaxies, we can use the photo-z's to reject projected pairs and identify the pairs that are physically associated. In practice, the pairs are identified by the separation and flux ratio criteria, and additionally a photo-z criterion: if the companion has a separate COSMOS entry with reliable photo-z (`odds` ≥ 0.95), the 3σ confidence intervals of the photo-z's must overlap. The number of massive galaxies in pairs is given by $\mathrm{N'_p}$, and the pair fraction is given by $f_p = \mathrm{N'_p}$ / M.

2.3 Results and discussions

2.3.1 Comparison with previous observations

In order to examine the redshift evolution of the pair fraction, we correct for chance projections in the observed pairs in COSMOS to get f_p in different redshift bins through our default approach, as listed in Table 2.1 and plotted on Figure 3.B.1. The pair fraction derived using the photo-z criterion is remarkably consistent with our default approach, except at the highest redshift bin in which photo-z's have higher uncertainties and therefore less constraining, but still marginally consistent. The Kolmogrov-Smirnov test confirms that the fraction of massive galaxies in pairs is inconsistent with no redshift evolution. We fit the observed f_p with a power law of the form $F(z) = F(0)(1+z)^m$, and find the best fit parameters to be $F(0) = 0.07 \pm 0.04$ and $m = 0.6 \pm 0.5$.

Robaina et al. (2010) (hereafter R10) use the amplitude of the projected two-point correlation function of massive galaxies to estimate the pair fraction of galaxies in the COSMOS and COMBO-17 surveys at $z = 0 - 1.2$, requiring galaxy pairs to be separated by less than 30 kpc in three-dimensional space, and each galaxy to be more massive than $5 \times 10^{10}\ M_\odot$. Applying their mass limit to both galaxies in our pairs, we find a f_p consistent with their results at $z \leq 1.2$, though we note that it is rare to find two galaxies that are both massive in a close pair. Our sample of ~ 200 massive galaxies yield relatively large uncertainties in the pair fraction due to small number counts, compared to R10's sample of ∼18,000 massive galaxies. The agreement ensures that our results are compatible with previously published f_p below $z = 1.2$ (Xu et al., 2004; Bell et al., 2006a; McIntosh et al., 2008; Bundy et al., 2009) that are consistent with R10's f_p.

Our corrected pair fractions agree to that of Law et al. (2011) within the uncertainties, though we note that their sample are based on star-forming galaxies above $10^{10} M_\odot$.

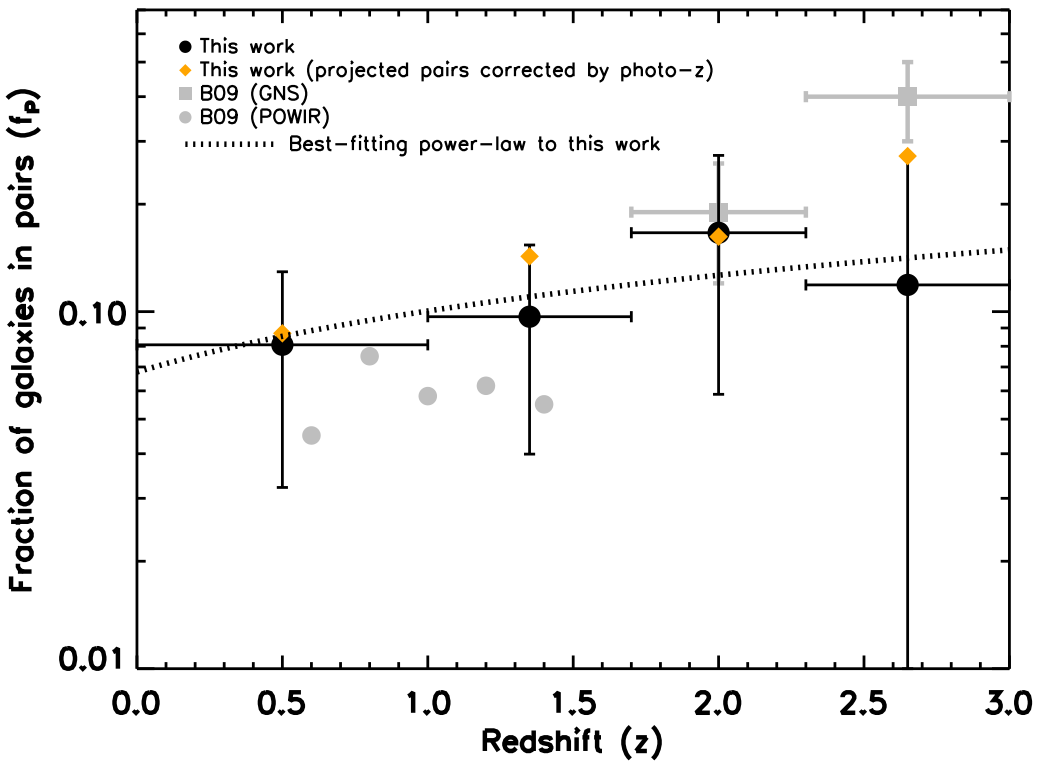

Figure 2.3: The redshift evolution of the pair fractions, compared to other observations. The black circles denote the f_p of our analysis, after statistically correcting for projection contamination. The black dotted line show the best-fitting power law to our f_p, which is of the form $F(z) = (0.07 \pm 0.04) \times (1+z)^{0.6\pm0.5}$. The orange diamonds denote our f_p, which we use an alternative approach to correct for projection contamination with the available photo-z's. The gray squares and circles represent the f_p of Bluck et al. (2009) using the GNS and POWIR data. The horizontal bars indicate the width of each bin.

Bluck et al. (2009) (hereafter B09) present a study of 82 massive galaxies with NICMOS imaging at $1.7 < z < 3$ from the GOODS NICMOS survey (GNS), and define pairs as any galaxy within 30 kpc and within a difference of ± 1.5 in H_{160}-magnitude compared to the host massive galaxy. They find the pair fraction to be 0.19 ± 0.07 at $1.7 < z < 2.3$ and 0.40 ± 0.10 at $2.3 < z < 3$. The comparison is shown in Figure 3.B.1. We also compare to the pair fraction from the POWIR survey at $z \sim 1$ from B09. Note that the COSMOS catalog is i-band selected, whereas the GNS targets are selected using three different criteria (Distant Red Galaxies, Infrared Extremely Red Objects and BzK galaxies); (Conselice et al., 2011). Despite the fact that the difference in the selection could potentially bias the results, our agreement with the Bluck et al. (2009) results is a

strong confirmation of high pair fraction at $z \sim 2$.

2.3.2 How robust is our pair fraction?

In our analysis, we quote the pair fraction based on the relative fraction of galaxies to a certain depth. When the pair fraction is translated to a merger fraction, it is necessary to account for any systematic bias of our massive galaxy sample, i.e. whether the galaxies that we miss due to the limited i-band depth have the same pair fraction. We perform a test to estimate the effect of the incompleteness on our observed pair fraction. In §2.2.3.1, we demonstrate that the adopted mass limit is 75% (44%) complete in selecting massive galaxies at $1.7 \leq z \leq 2.3$ ($2.3 \leq z \leq 3.0$). If our sample of 37 massive galaxies is 75% complete at $1.7 \leq z \leq 2.3$, we can estimate that in total there are ∼49 massive galaxies, and we miss ∼12 of them because of their faintness in the i-band. If we assume the extreme scenarios, in which all the missed galaxies are (not) in pairs, the pair fraction in $1.7 \leq z \leq 2.3$ would then be 0.37 ± 0.11 (0.12 ± 0.08). For $2.3 \leq z \leq 3.0$, a similar calculation yields f_p of 0.05 ± 0.07 and 0.61 ± 0.13 at the limits. It is apparent the conservative lower limits are within the errors of our observed f_p.

The massive galaxies fainter than $i = 26$ are likely to be at the high redshift end, and the faintness can be explained by dusty star formation or evolved stellar populations. Using the deeper, K-band selected CDFS catalog, we find that $f_p = 0.21^{+0.26}_{-0.17}$ at $1.5 \leq z \leq 3.0$ for $26 < i < 27$, in the fainter regime where the COSMOS catalog is incomplete. This is consistent with our expectation that the missed galaxies would have a similar f_p as observed in COSMOS for the i-band brighter galaxies. We note that the CDFS covers a smaller area than COSMOS, and hence statistical errors in the resulting f_p are more severe.

2.3.3 The growth of the massive galaxy population through merging

2.3.3.1 Merger rate

We calculate the merger rate as $\Re(z) = f_p(z)n(z)\tau^{-1}$, where the merging timescale (τ) is assumed to be 0.4 ± 0.2 Gyr (Lotz et al., 2008a), and the observed co-moving number density of massive galaxies is the number of massive galaxies (M) divided by the co-moving volume in that redshift range subtended by the usable area of 474 NICMOS pointings, i.e. $n(z)$ = M(z) / $V_{\rm co-moving}$. The completeness limits derived in §2.2.3.1 are used to correct M. The merger rates are listed in Table 2.1. As an estimate, the uncertainties of f_p, $n(z)$ and τ are approximately 69%, 20% and 50% respectively. This yields an uncertainty of $\sim 88\%$ in the derived merger rate. Therefore, the major merger rate, unlike the pair fraction, is consistent with no redshift evolution within the large range of uncertainties. The characteristic time between mergers (Γ) experienced by a

galaxy at a given redshift is given by $\Gamma = \tau/f_p$, and we find the best fit to its redshift evolution to be $\Gamma = 12(1+z)^{-1.6}$. By integrating Γ over our redshift range (see Equation (6) of B09), we estimate that a galaxy experiences $N_m = 1.1 \pm 0.5$ major mergers on average from $z = 3.0$ to $z = 0$, consistent with B09's $N_m = 1.7 \pm 0.5$ within the large uncertainties.

2.3.3.2 Number density evolution

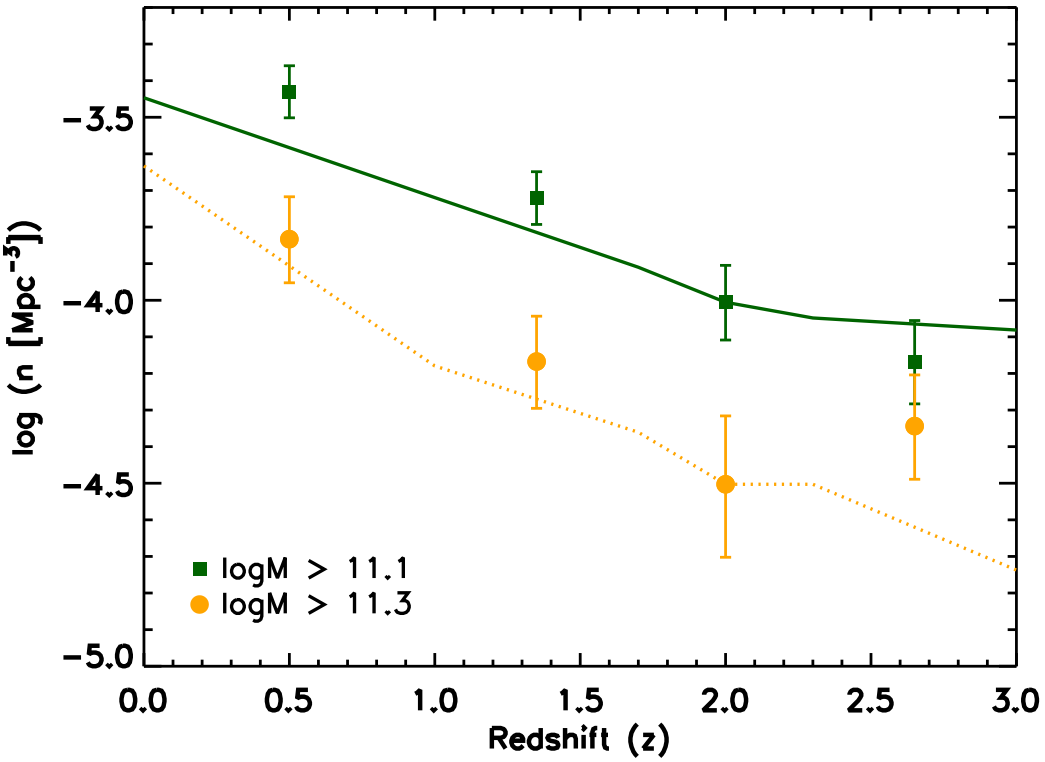

Figure 2.4: The redshift evolution of number density of massive galaxies. The filled symbols are the observed co-moving number density of massive galaxies from our sample, with mass limits shown in the legend. The lines represent the predicted number growth using the observed number density of close pairs, after correcting for projected pairs using photo-z. The lines are normalized to the observed number density at $z = 2$.

The mass function (MF) of galaxies is altered by mergers. If the merger fraction at different epochs is known, one can translate it into the evolution of the massive galaxy population assuming a merging timescale ($\tau = 0.4 \pm 0.2$ Gyr in this Paper). We estimate the number of newly created massive galaxies using the selected galaxy pairs: for each pair, we calculate the remnant mass as the sum of the SED masses of the galaxies in the

pair. In the rare case (4 pairs) where the SED mass is not available for the companion galaxy because there is no corresponding entry in the catalog, we use the flux ratio and the SED mass of the primary massive galaxy to estimate the remnant mass. Here we have assumed that the H_{160} flux ratio corresponds to the mass ratio, and we verify the assumption by finding consistent remnant masses using the flux and the mass ratios for the remaining pairs. The number of newly created massive galaxy ($N_{created}$) in each redshift bin is calculated by counting the galaxies that cross the mass limit after merging. The merger-induced increment in the co-moving number density (Δ, in units of Mpc^{-3}) is given by:

$$\Delta = \frac{N_{created} \times t_{elapsed}}{V_{co-moving} \times \tau}$$

where $t_{elapsed}$ is the time elapsed within the redshift bin. Our selected galaxy pairs consists of primary galaxies of $M_\star \geq 10^{11} M_\odot$, with companions of flux ratio down to 1:4. Therefore, the remnant mass would be at least $1.25 \times 10^{11} M_\odot$ ($logM = 11.1$). In the case of an equal-mass merger, the remnant mass will be $2 \times 10^{11} M_\odot$ ($logM = 11.3$). Normalizing the number density of massive galaxies to the observation at $z = 2$, the results are compared with the observed number density of massive galaxies above these mass limits, as shown in Figure 2.4. Considering the $\sim$ 0.2 dex uncertainty in the number density growth due to counting statistics, the slope of the number growth is remarkably consistent with the observed number density. As the highest redshift bin ($z > 2.3$) is only 44% complete, the projected number growth is highly uncertain. The agreement between our estimated merger-induced number density growth and the observed number density supports the idea that major mergers are sufficient to explain the number density evolution of massive galaxies from $z \sim 2.3$ to 0.

One potential caveat of this test is that mergers of galaxies less massive than $10^{11} M_\odot$ are not included, due to mass incompleteness of the catalog. Another caveat is the assumption that no new stars are formed in the merging, which is only valid for dry merging. This can result in an underestimation of the number density growth of $log(M) > 11.1$ galaxies, where equal-mass mergers of two galaxies of down to $log(M) > 10.8$ could contribute to the number density. The number density evolution of massive galaxies depends on several factors: a merger between less massive galaxies can create a massive galaxy above the mass limit; on the other hand, if two massive galaxies merge, the number of massive galaxies would be reduced; the merging timescale is closely related to the growth rate of the massive galaxies. The buildup of the massive galaxies can be better constrained with larger samples of galaxies down to lower masses and higher redshifts, which will be feasible with the upcoming surveys. The study of number density evolution is complimentary to the mass density evolution (Conselice

et al., 2007) and the mass evolution of a fixed number density sample across redshift (van Dokkum et al., 2010), in tracing the buildup of massive galaxies. Our observed number densities show an agreement to van Dokkum et al. (2010)'s finding that the stellar mass of massive galaxies double since z = 2. A precise measurement of the contribution of mergers to the number density evolution requires accurate determination of the merging timescale, and is beyond the scope of this Paper.

If massive galaxies undergo $\sim 1.1 \pm 0.5$ major merger between $0 < z < 3$ and this is sufficient to explain the number density evolution, then this hints that major merging can be ruled out as the main mechanism for puffing up the sizes of massive, compact and quiescent galaxies from $z \sim 2$ to 0, as this size evolution requires 2-3 major mergers (Bezanson et al., 2009; Toft et al., 2009).

2.3.3.3 Comparison with models

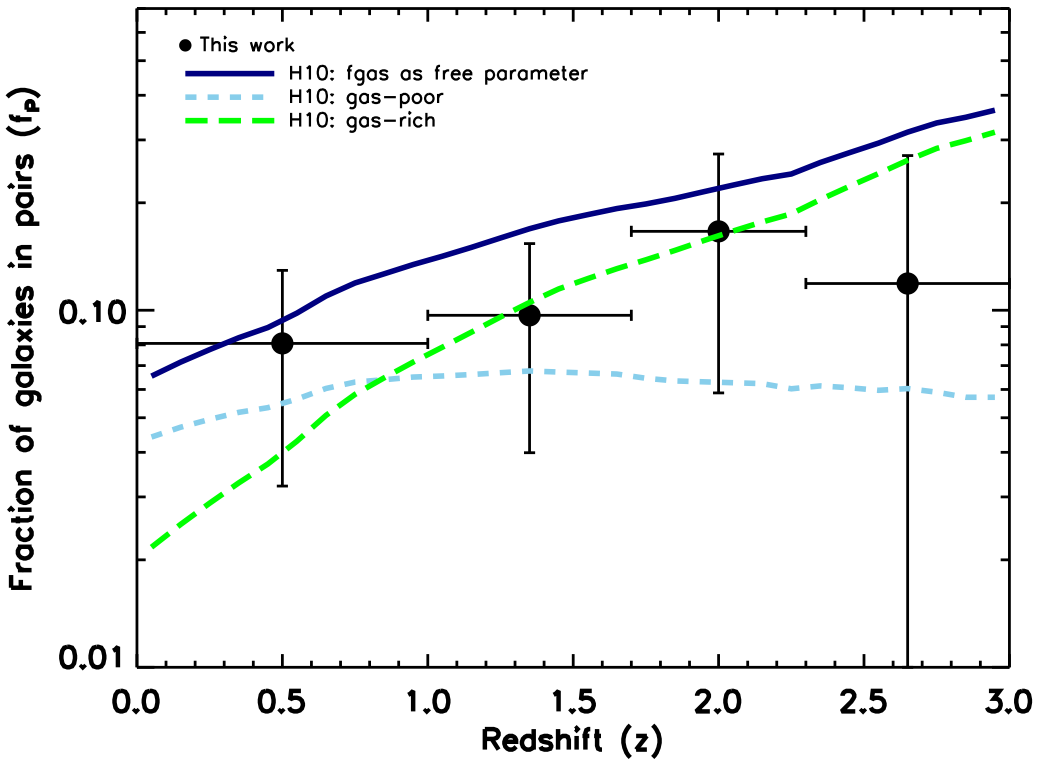

Figure 2.5: A plot similar to Figure 3.B.1 that compares our pair fractions to model predictions. The colour lines are the predicted f_p for pair-selected samples from the merger rate calculator of Hopkins et al. (2010b) assuming different sets of gas fraction.

To understand how our observations fit into the current understanding of galaxy formation in a cosmological context, we compare our observed pair fraction to the expected merger fraction in pair-selected samples computed from the "merger rate calculator" (MRC) developed by Hopkins et al. (2010b) (hereafter H10). H10 use a halo occupation model to track merger history, according to the merger trees constructed from the Millennium Simulation (Fakhouri & Ma, 2008). The galaxy-galaxy merger rate is determined by convolving the distribution of galaxies in halos with the dynamical timescale. Assuming a merging timescale of 0.35 ± 0.15 Gyr (Lotz et al., 2008a), the merger rate is then converted to a merger fraction. Using a simplified fitting function, the MRC predicts the merger fraction as a function of galaxy mass, gas fraction, redshift and mass ratio. We compute the galaxy-galaxy merger fraction at $0 \leq z \leq 3.0$ for galaxies of stellar mass between 10^{11} and 10^{12} $M_{\odot}$, the range of masses of our massive galaxies sample, and of mass ratio down to 1:4. The average gas fraction of the pair, defined as $f_{\rm gas}$ = $M_{\rm gas}$ / ($M_{\rm gas}$ + $M_{\star}$), is a free parameter in the model. Direct measurements of the gas mass fraction of massive star-forming galaxies at z ~ 1 and $z \sim 2$ give 34% and 44% respectively (Tacconi et al., 2010); and 50%-65% for similar systems at $z \sim 1.5$ in another study (Daddi et al., 2010). These systems are considered evidence for very gas-rich systems at those epochs, hence we select the critical gas fraction ($f^{\star}_{\rm gas}$) to be 20% to differentiate gas-poor ($0 \leq f_{\rm gas} \leq f^{\star}_{\rm gas}$) and gas-rich ($f^{\star}_{\rm gas} \leq f_{\rm gas} \leq 1$) mergers. Then we multiply the merger fraction, as a function of redshift, by two to get the predicted fraction of galaxies in pairs to compare with our observations in Figure 2.5. To investigate the importance of dry merging (i.e. nearly dissipationless mergers), we overplot the gas-poor and gas-rich pair fraction for comparison.

Considering that the systematic uncertainties in the predicted pair fraction are larger than a factor of two, our observed pair fraction is consistent with the prediction of H10's model. The number of gas-rich mergers are sufficient to explain the number of observed pairs at $1 \leq z \leq 3$. Gas-poor mergers are predicted to be more frequent than gas-rich mergers below $z = 1$ (see H10), and are required to explain the observed pair fraction. H10's model predicts 2.1 major mergers per galaxy from $z = 3$ to $z = 0$, which is almost twice of our result and is apparent from the predicted pair fraction in Figure 2.5. Our result is also low compared to ~ 1 major merger per galaxy at $0 < z < 1.5$ for $M_{\star} \geq 10^{10.8} M_{\odot}$ (mass limit converted from Salpeter into Chabrier IMF for comparison) predicted by Drory & Alvarez (2008), who estimate the contribution of merging by subtracting the effect of mass-dependent star formation from the galaxy stellar MF. The discrepancy is mostly due to the difference in mass limit, confirmed by a similar value of 1.1 major merger predicted by Hopkins et al. (2010b)'s MRC if we use Drory & Alvarez (2008)'s mass limit. To reproduce their results of ~ 2 major mergers we need to use a merging timescale of 0.25 Gyr, which is lower, yet still within the uncertainties of Lotz et al. (2008a)'s range of merging timescale for pairs having projected separa-

tion up to 30 kpc. The expected number of major majors from Drory & Alvarez (2008) and Hopkins et al. (2010b) are based on observations of the MF, whereas our result is a direct measurement of the pair fraction converted into the number of major mergers using the merging timescale and the number density of massive galaxies. This illustrates the need to better constrain the merging timescale, and to improve the understanding of how merging alters the MF, in order to push merger rate measurements to higher accuracy.

2.4 CONCLUSIONS

We have quantified the pair fraction of 198 massive ($M_\star \geq 10^{11} M_\odot$) galaxies at $0 \leq z \leq 3$ from COSMOS with NICMOS parallels. Our findings provide a confirmation of the evolution of pair fraction from $z = 3$ to $z = 0$, in agreement with previous observations (Bluck et al., 2009) and predictions from halo-occupation modelling (Hopkins et al., 2010b). Gas-rich mergers are sufficient to explain the observed pair fraction from $z = 3$ to 1; below $z = 1$ gas-poor mergers are also needed. The fraction of massive galaxies observed to be in pairs is 0.15 ± 0.08 from $1.7 \leq z \leq 3.0$. The redshift evolution of the pair fraction is described by a power law $F(z) = (0.07 \pm 0.04) \times (1 + z)^{0.6 \pm 0.5}$. The merger rate is consistent with no redshift evolution, though the uncertainties in pair counts and merging timescale restrict the ability to conclusively constrain the merger rate. On average, a massive galaxy undergoes $\sim 1.1 \pm 0.5$ major merger from $z = 3$ to 0, assuming a merging timescale of 0.4 Gyr. Using the inferred merger fraction, we are able to reproduce the observed number density of massive galaxies since $z \sim 2.3$. This implies that major merging can account for the number density evolution of the massive galaxies, but other mechanisms such as minor merging may be required to explain the size evolution of the massive, compact quiescent galaxies at $z \sim 2$.

Acknowledgements

The Dark Cosmology Centre is funded by the Danish National Research Foundation. S. Toft and A. W. Zirm gratefully acknowledge support from the Lundbeck Foundation. The authors thank the referee, Thomas Targett, for useful comments that helped improve the paper. A. W. S. Man thanks Kinwah Wu, Anna Gallazzi, Steen Hansen and Thomas Greve for insightful discussions.

3

WHAT GIVES RISE TO THE DISCREPANT GALAXY MERGER FRACTION?

Allison W. S. Man, Andrew W. Zirm, and Sune Toft

Dark Cosmology Centre, Niels Bohr Institute, University of Copenhagen

Submitted to the Astrophysical Journal on 18$^{\text{th}}$ July 2014
Positive referee report received on 12$^{\text{th}}$ September 2014
arXiv preprints: 1410.3479

Abstract

We measure the merger fraction of massive galaxies using the UltraVISTA/COSMOS *Ks*-band selected catalog, complemented with the deeper, higher resolution 3DHST + CANDELS catalog selected in the *HST*/WFC3 *H*-band, presenting the largest mass-complete photometric merger sample up to $z \sim 3$. We find that selecting mergers using the H_{160}-band flux ratio leads to an increasing merger fraction with redshift, while selecting mergers using the stellar mass ratio causes a diminishing redshift dependence. Defining major and minor mergers as having stellar mass ratios of 1:1 - 4:1 and 4:1 - 10:1 respectively, the results imply $\sim$1 major and $\lesssim$1 minor merger for an average massive ($\log(M_\star/M_\odot) \geqslant 10.8$) galaxy during $z = 0.1-2.5$. There may be an additional $\sim 0.5(0.3)$ major (minor) merger if we use the H-band flux ratio selection. The observed amount of major merging alone is sufficient to explain the observed number density evolution for the very massive ($\log(M_\star/M_\odot) \geqslant 11.1$) galaxies. We argue that these very massive galaxies can put on a maximum of 6% of stellar mass in addition to major and minor merging, so that their number density evolution remains consistent with observations. The observed number of major and minor mergers can increase the size of a massive quiescent galaxy by a factor of two at most. This amount of merging is enough to bring the compact quiescent galaxies formed at $z > 2$ to lie at 1σ below the mean of the stellar mass-size relation as measured in some works (e.g. Newman et al., 2012), but additional mechanisms are needed to fully explain the evolution, and to be consistent with works suggesting stronger evolution (e.g. van der Wel et al., 2014).

3.1 INTRODUCTION

For decades, galaxy merging has been a popular explanation for the observed evolution in galaxy properties. Galaxy mergers were first invoked to explain the morphological transformation of galaxies (Toomre & Toomre, 1972; Barnes & Hernquist, 1996). Merging remains the backbone in cosmological simulations in building up large galaxies (e.g. Springel et al., 2005; Bower et al., 2006). Gas-rich major mergers at high redshifts ($z > 2$) are thought to trigger starburst and active galactic nuclei (AGN) episodes, quench star formation, and lead to bulge formation, thereby building the massive ellipticals in the local Universe (Barnes & Hernquist, 1991; Mihos & Hernquist, 1994; Kartaltepe et al., 2010; Toft et al., 2014). An alternative scenario has been proposed more recently, in which massive galaxies at high redshift are clumpy disks which are very efficient in turning incoming cold gas into stars (Dekel et al., 2009). The most luminous AGNs and ultra-luminous infrared galaxies (ULIRGs) take place in major galaxy mergers (Kartaltepe et al., 2010; Treister et al., 2012; Ellison et al., 2013). Merging galaxies have enhanced star formation activity compared to isolated ones (Patton et al. 2011; Yuan et al. 2012; Patton et al. 2013; but also see Xu et al. 2012b; Lanz et al. 2013). As galaxy merging may have profound influence on how the galaxy population evolved to this day, quantifying its rate of occurrence is essential to judge whether it explains any of the observed evolutionary trends.

As the timescale for galaxy mergers is on the order of a Gyr (e.g. Lotz et al., 2010), the conventional way to measure galaxy merger rate is to divide the observed fraction of galaxies undergoing mergers by a typical merging (observability) timescale at different redshift bins. Merging galaxies can be identified as close galaxy pairs or galaxies displaying disturbed morphologies, and the timescale required to convert the merger fraction to merger rate depends on the specific selection technique. In this work we use the pair selection method, as the merger fraction measured from morphological selection (e.g. López-Sanjuan et al., 2009; Bluck et al., 2012) and the merging observability timescale are dependent on the imaging depth and resolution. The advent of multi-wavelength blank field observations in the past decade have enabled many improvements in the measurement of merger fractions, including the following: (1) the merger fraction of massive galaxies can be measured beyond $z \sim 1$; (2) the photometric redshifts allow more accurate removal of the pairs projected along the line-of-sight; (3) the stellar masses derived from the spectral energy distribution (SED) fitting provide the stellar mass ratio of galaxy pairs, which is a more physically meaningful proxy for the dynamical interaction than a single-band flux ratio; (4) deeper and wider area surveys provide larger samples, which in turn allow the dependence of merger fractions on different parameters to be explored. Multiple authors have measured the merger fraction at $z > 1$, presenting somewhat conflicting results: does the merger fraction increase with redshift (Bluck et al., 2009; Man et al., 2012), remain constant, or even di-

minish (Williams et al., 2011; Newman et al., 2012)? As shown in Lotz et al. (2011), the variation of the parent galaxy selection and mass ratio limits can contribute to some of the discrepancies across studies. On the other hand, the average merging observability timescale is hard to estimate due to the large possible variety of orbital parameters and viewing angles, as well as the lack of observed dynamical information on a galaxy-to-galaxy basis. The uncertainties in the implied merger rates are discussed thoroughly in Hopkins et al. (2010d).

In this work, we present the largest sample of photometrically selected mergers at z=0.1-3 to date from stellar mass complete catalogs. The *Ks*-band selected catalog from the UltraVISTA/COSMOS survey (Muzzin et al., 2013) covers a large area, allowing us to expand our merger sample to more than five times larger than previous studies. We complement the ground-based UltraVISTA catalog with the space-based 3DHST+CANDELS (Skelton et al., 2014) catalog, which is deeper and has higher spatial resolution, to study possible systematic effects in measuring merger fractions. The remainder of the paper is structured as follows: Section 4.2 describes the UltraVISTA and the 3DHST+CANDELS catalogs used in our study. We present the criteria for selecting massive galaxies and mergers, as well as the completeness of the catalogs. In Section 3.3 we present the method of measuring the merger fractions as a function of redshift. We compare the merger fractions measured using the two catalogs, as well as the selection using the stellar mass ratio and H_{160}-band flux ratio. We examine the stellar mass ratio distribution of the selected mergers. We discuss the two main sources of uncertainties in the merger fraction measurements. We show that we are complete to detecting minor mergers up to $z = 2.5$. Finally we convert the merger fractions to merger rates, and infer the merger contribution in the stellar mass, size, velocity dispersion and number density evolution of massive galaxies. Based on our findings, we address some broader questions in the context of galaxy evolution in Section 4.5: What do the merger rates imply for the evolution of massive quiescent galaxies? Is merging an influential process in the cosmic star formation history or not? We also discuss the future prospects of merger fraction studies. The conclusions of this work is summarized in Section 3.5. In Appendix 3.A we present the simulations we perform to test for the completeness limits of the faintest possible satellites. Appendix 3.B provides an in-depth comparison to similar merger fraction measurements in the literature.

All magnitudes are quoted in the AB system. A cosmology of H_0 = 70 km s^{-1} Mpc^{-1}, $\Omega_{\rm M}$ = 0.3 and Ω_Λ = 0.7 is adopted throughout this work.

3.2 DATA AND SAMPLE SELECTION

3.2.1 ULTRAVISTA CATALOG

We use the *Ks*-band selected catalog for the UltraVISTA Survey compiled by Muzzin et al. (2013). The UltraVISTA survey targets the COSMOS field (Scoville et al., 2007b) with the ESO VISTA survey telescope. The effective survey area of UltraVISTA is 1.62 deg^2. The catalog contains PSF-matched photometry in 30 photometric bands covering the wavelength range 0.15 - 24μm and includes the *GALEX* (Martin et al., 2005), CFHT/Subaru (Capak et al., 2007), UltraVISTA (McCracken et al., 2012), S-COSMOS (Sanders et al., 2007), and zCOSMOS (Lilly et al., 2007) datasets. The UltraVISTA source detection is performed on the *Ks*-band image with a $2.1''$ aperture, which has a limiting magnitude of 23.7 ± 0.1 ($5\sigma, 2''$-aperture). In total there are 154 803 detected sources with reliable photometry having *Ks*< 23.4, which is the 90% completeness limit and the adopted luminosity limit in this work. The stellar masses quoted in this paper are derived assuming a Chabrier IMF. Further details regarding the photometric redshifts (photo-z's) and SED fitting can be found in Muzzin et al. (2013).

3.2.2 3DHST+CANDELS CATALOG

To complement the ground-based *YJHK*$_s$ imaging from VISTA, we use the 3DHST catalog presented in Brammer et al. (2012) and Skelton et al. (2014), which includes *HST* imaging from the CANDELS survey (Grogin et al., 2011; Koekemoer et al., 2011) over five fields: COSMOS, GOODS-North and South, AEGIS, and UDS with a combined usable area of ~ 0.25 deg^2. Skelton et al. (2014) performed photometry (aperture of $0.7''$) on the PSF matched images and compiled a photometric catalog with photo-z's and SED best fits. We only use the objects marked with good photometry to ensure reliable photo-z's and stellar masses.

3.2.3 SELECTING MASSIVE GALAXIES AND MERGERS

We use close galaxy pairs as a probe for galaxy mergers following similar criteria used in the literature (Bluck et al., 2009; Williams et al., 2011; Man et al., 2012; Newman et al., 2012). In the UltraVISTA catalog, there are 9829 massive ($\log(M_\star/M_\odot) \geqslant 10.8$) galaxies in the redshift range of $0.1 < z \leqslant 3.0$, and 380 ($\sim 3.9\%$) of them are covered by the *HST*/WFC3 H-band imaging from the CANDELS and 3DHST COSMOS surveys. Around these massive galaxies, we search for galaxy satellites fulfiling the following criteria:

1. Within a projected separation of $R_{proj} = 10 - 30$ kpc h^{-1}.
2. Stellar mass ratio $\mu = M_1/M_2$ of 1:1 - 4:1 as major merger, 4:1 - 10:1 as minor merger.
3. The 1σ confidence intervals of the photo-z's of the pair overlap.

We calculate R_{proj} using the angular scale based on the photo-z's of the more massive galaxy. As the FWHM of the ground-based UltraVISTA Ks-band image is $\sim 0.8''$, corresponding to a maximum of 9.7 kpc h^{-1} at $z \sim 1.5$, we use 10 kpc h^{-1} as the lower limit of R_{proj} to ensure that no close pairs are missed due to blending. In Section 3.3.3.2 we explore the use of different R_{proj} bins up to 100 kpc h^{-1}. We explore the use of the H-band flux ratio as a probe for the stellar mass ratio in Section 3.3.1.1, which we demonstrate to have a profound impact on the merger fraction evolution at $z > 1.5$. The redshift distribution of massive galaxies and pairs are listed on Table 3.2.

3.2.4 COMPLETENESS LIMITS

We assess the completeness limit of the massive galaxies and their 4:1 and 10:1 satellites in two aspects: the stellar mass completeness and the surface brightness limits. We detail our analysis in Appendix 3.A and give the summary as follows. We find that the surface brightness limit is the constraining factor for detecting the satellites of massive galaxies. If completeness is only estimated by comparing the magnitude-redshift distribution to deeper catalogs, the completeness limits may be overstated. We find that UltraVISTA (3DHST+CANDELS) is complete to $z = 2.4$ and $z = 1.5$ ($z = 3.0$ and $z = 2.5$) for major and minor mergers respectively. In this work, the data points at redshift bins which are mass incomplete are either omitted or plotted as lower limits, to ensure that incompleteness does not affect our conclusions. Despite the fact that 3DHST+CANDELS is deeper than UltraVISTA and can probe the merger fractions to higher redshifts, we demonstrate in Section 3.3.1 that we do not get a higher merger fraction, both major and minor, with 3DHST+CANDELS compared to UltraVISTA, suggesting that there is not a significant population of mergers that have faint quiescent satellites only detectable in the 3DHST+CANDELS catalog.

3.3 METHOD AND RESULTS

The relation between the number of observed galaxy pairs ($\mathbb{N}_{\text{observed pairs}}$) and the number of ongoing physical galaxy mergers ($\mathbb{N}_{\text{physical mergers}}$) can be described as $\mathbb{N}_{\text{physical mergers}} = \mathbb{N}_{\text{observed pairs}} - \mathbb{N}_{\text{projected pairs}} - \mathbb{N}_{\text{non-merging pairs}}$. The quantity $\mathbb{N}_{\text{observed pairs}}$ is defined as the number of galaxy pairs observed that satisfy a projected separation and mass (or flux) ratio criteria, e.g. pairs fulfiling the first two criteria listed in 3.2.3. Among the observed pairs, some are galaxy pairs of physical proximity, while some pairs are galaxies projected along a similar line-of-sight. The line-of-sight projected galaxy pairs can be corrected for using redshift measurements (photometric or spectroscopic) or statistical arguments based on the galaxy mass or luminosity function. In this work we apply a photo-z criterion as listed in Section 3.2.3 to correct for projected pairs ($\mathbb{N}_{\text{projected pairs}}$). We have demonstrated in Man et al. (2012) that using the photo-z's to correct for chance

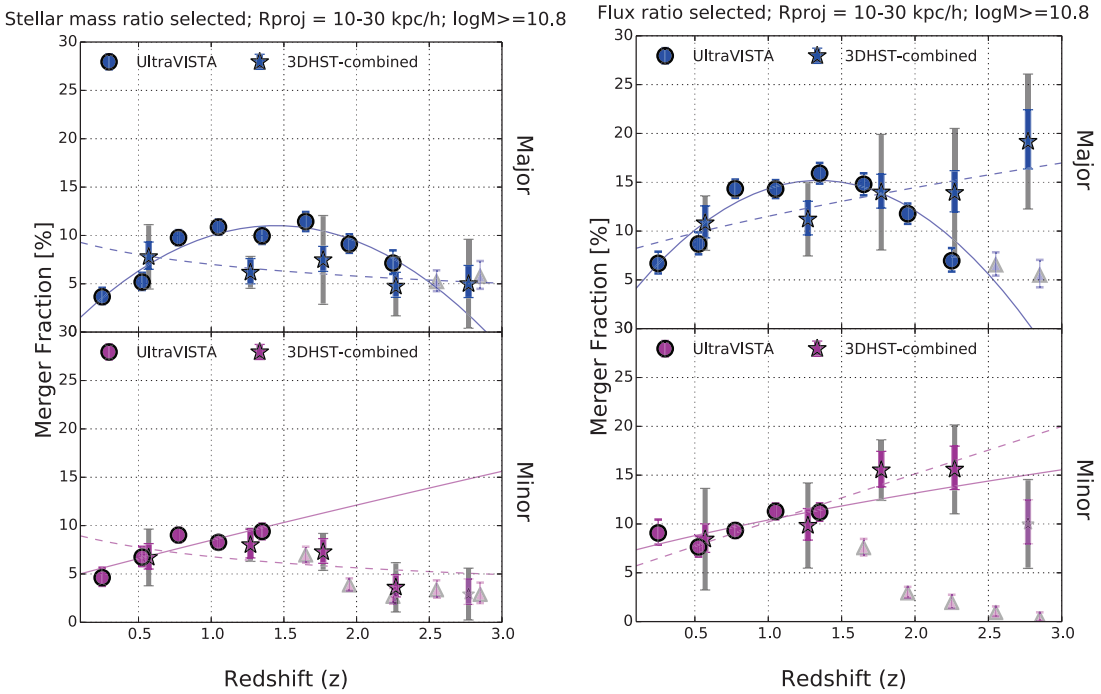

Figure 3.1: The merger fractions of the UltraVISTA (filled circles) and the combined results of the five 3DHST+CANDELS fields (filled stars). The left and right panels show the mergers selected by the stellar mass ratio and H-band flux ratio respectively, following the definitions in Section 3.2.3. The top panels show major mergers (stellar mass or flux ratio 1:1 - 4:1) and the bottom panels show minor mergers (stellar mass or flux ratio 4:1 - 10:1) around massive ($\log(M_\star/M_\odot) \geqslant 10.8$) galaxies, where the mergers have matching photo-z's and have projected separation between 10 - 30 kpc h^{-1}. For the 3DHST data points, we combine the pair counts in all five fields, and we display the Poisson errors of the combined pair counts of the five fields (colored error bars) as well as the standard deviation of individual measurements from the mean (gray error bars). The redshift bins estimated to be incomplete for low surface brightness satellites are marked with semi-transparent upward triangles (UltraVISTA) or small stars (3DHST+CANDELS) following the same color scheme. The colored solid and dashed lines are the best-fitting functions to the merger fractions of the UltraVISTA and the 3DHST+CANDELS respectively, as presented in Section 3.3.1 and Table 3.1.

alignments yield results consistent with statistical corrections at $z = 0 - 3$.

In this work we do not correct for physical galaxy pairs at matching redshifts that are not energetically bound to merge, i.e. we assume $\mathbb{N}_{\rm non-merging\ pairs} = 0$. Cosmological simulations can provide a statistical estimate of $\mathbb{N}_{\rm non-merging\ pairs}$ to account for the unbound galaxy pairs in cluster environments with high relative velocities. However, the interpretation may be complicated by the presence of a third neighbor which is not uncommon (Moreno, 2012; Moreno et al., 2013), or these pairs simply require more time

before the eventual coalescence (Kitzbichler & White, 2008). Galaxy fly-bys may be frequent (Sinha & Holley-Bockelmann, 2012) but it remains unexplored how high-speed encounters may impact the mass distribution and light profiles of galaxies. Even if the cores do not coalesce, mass from the satellite may still be deposited onto the host galaxy, and the energy exchange can lead to size growth akin to a "real" merger (Laporte et al., 2013). It is not well understood how $\mathbb{N}_{\rm non-merging\ pairs}$ evolves with the environment and redshift. At higher redshift, massive galaxies are expected to be less clustered than at the present day, so the effect is likely more dominant at low redshift. Future studies of the dynamical properties of galaxy pairs at different redshifts and environments may provide new insights into this effect, but for now we do not have enough information to correct for it. We note that by including non-energetically bound pairs in our selection, the merger fractions derived in this paper are formally upper limits. Hereafter we refer to $\mathbb{N}_{\rm physical\ mergers}$ as N_{pair} for simplicity.

3.3.1 REDSHIFT EVOLUTION OF THE MERGER FRACTION

We define the merger fraction as the fraction of massive galaxies that are merging with a less massive companion, i.e. $f = N_{pair}/N_{massive}$. The major and minor merger fractions (f_{major} and f_{minor}) in redshift bins are listed on Table 3.2 and plotted on Figure 3.1 (left). We parameterize the merger fractions within the completeness limits by a power law using least squares fitting. In the case of f_{major} declining beyond $z \sim 1.5$ in UltraVISTA, the reduced χ^2 value for the power law fit exceeds 10 indicating a bad fit so we fit the data points with a quadratic function instead. We list the best fitting parameters in Table 3.1.

Using the stellar mass ratio selection, we find that f_{major} (f_{minor}) increases from $z \sim 0.1$ to reach a peak at $z \sim 0.8$, remains relatively constant to $z \sim 1.7$ ($z \sim 1.4$) and then diminishes towards higher redshift. A comparison between the merger fractions derived from the ground-based UltraVISTA and the deeper, higher resolution 3DHST+CANDELS reveals very similar f_{major} and f_{minor} in both samples. In fact, f_{major} is slightly lower in 3DHST+CANDELS than in UltraVISTA at $z = 1 - 1.5$. If we include the pairs without photo-z information (columns 3 and 7 on Table 3.2) in our merger sample, the f_{major} of 3DHST+CANDELS at this redshift bin becomes consistent with the one from UltraVISTA. This illustrates that space-based data is not required for measuring the galaxy merger fraction. In fact, ground-based data with a large survey volume such as UltraVISTA provides the optimal dataset, as the sample is adequately large to measure the redshift dependence of the merger fractions in finer redshift bins. We elaborate on the uncertainties of merger fraction measurements in Section 3.3.1.2.

3.3.1.1 Stellar mass ratio or flux ratio?

Merger fraction measurements have led to conflicting conclusions regarding whether it increases with redshift at $z > 1.5$ (Bluck et al., 2009; Man et al., 2012) or not (Williams et al., 2011; Newman et al., 2012). The former studies use the single band flux ratio from *HST H*-band imaging to estimate the mass ratio, rather than full the stellar mass ratio from SED fits used in the latter studies. We explore the possibility of a systematic effect regarding the ratio used in the merger selection. We repeat the selection of mergers with the H_{160}-band flux ratio instead of using the stellar mass ratio on the same dataset presented in Section 4.2, namely the UltraVISTA and 3DHST+CANDELS catalogs.

The results are presented in Figure 3.1 (right). It is apparent that the combination of using the flux ratio to select mergers and the 3DHST+CANDELS catalog leads to an increasing redshift trend of f_{major} (f_{minor}) up to $z = 3$ ($z = 2.5$) where the catalog is complete for major (minor) satellites. This is in contrast to the flat or even diminishing evolution found when mergers are selected by the stellar mass ratio (Figure 3.1, left), as well as using flux ratio to select mergers from UltraVISTA (filled circles in Figure 3.1, right). Our results are in good agreement with the trends found in literature (see Appendix 3.B for details of the comparison) meaning that we are able to reproduce the increasing redshift trend of the merger fraction if mergers are selected by flux ratio.

By comparing the mergers selected in the overlapping area of the UltraVISTA and CANDELS-COSMOS surveys, we find that the flux-ratio selected satellites at $z > 2$ are close to the survey depth of UltraVISTA DR1 ($K \sim 23.4$, Muzzin et al. 2013), and therefore fainter satellites are missed due to low surface brightness. We interpret the difference between the flux ratio selected merger fraction between the UltraVISTA and the 3DHST-CANDELS samples as being due to the observation limit of the UltraVISTA DR1 data. This is expected to improve for the forthcoming data release of UltraVISTA in which the survey depth of the four ultra-deep stripes will be ~ 1 mag deeper.

In order to explain the difference between the flux and stellar mass ratio selections using the 3DHST+CANDELS catalog, we compare the stellar mass ratio and flux ratio distribution of the mergers using both selection techniques in Figure 3.3. We display the results for the redshift bin $z = 2 - 3$ where the discrepancy in the merger fraction is most significant between the two selection techniques. We find that almost all of the stellar mass ratio (1:1-10:1) selected mergers have H-band flux ratio in the same range. On the other hand, flux ratio selected mergers (1:1-10:1) include mergers with stellar mass ratios in the same range, as well as mergers with more extreme stellar mass ratios (>10:1). Among the major *flux ratio* pairs at $z = 2 - 3$ in 3DHST+CANDELS, only 29% have major *stellar mass* ratios. The remaining pairs consist of minor *stellar mass* ratio (19%) and mostly very minor *stellar mass* ratio (52%) with M_1/M_2 >10:1. This demonstrates that the observed H-band flux is a biased tracer of the stellar mass at $z > 2$. Using the H-band flux ratio as a probe for the stellar mass ratio leads to the inclusion of

bluer, less massive galaxies as satellites. In another words, at $z > 2$ most of the satellites are star-forming blue galaxies that are bright in the rest-frame optical B- or V-bands. We conclude that the flux ratio selection yields a higher merger fraction than mass ratio selection at all redshifts for two reasons: (1) the observed H-band probes bluer rest-frame bands at higher z; (2) lower $M_\star/L_V$ satellites enter the sample (Bundy et al., 2004; Newman et al., 2012), where $M_\star/L_V$ is the ratio of the stellar mass to the rest-frame V-band luminosity. We illustrate the redshift dependence of $M_\star/L_V$ in Figure 3.2. There is overall $M_\star/L_V$ redshift evolution in both the massive galaxies and their satellites, in which the ratio increases over cosmic time. Both catalogs show a similar $M_\star/L_V$ evolution except for the H-band flux ratio selected pairs in the CANDELS+3DHST sample, where the evolution is steeper implying the inclusion of lower $M_\star/L_V$ at $z > 2$ than for the stellar mass ratio selection. At $2 < z \leqslant 3$ the observed H_{160}-band roughly corresponds to the rest-frame B and V bands. Our simulations in Appendix 3.A.2 indicate that we are complete to $z = 3(2.5)$ for major (minor) mergers in 3DHST+CANDELS, therefore the $M_\star/L_V$ evolution cannot be explained by observational effects and is intrinsic. The $M_\star/L_V$ evolution reflects the higher star formation activity at $z \sim 2$ compared to that of the present day (e.g. Lilly et al., 1996; Madau et al., 1996).

Having shown that the use of the flux and stellar mass ratio can reproduce the discrepancy in merger fraction in literature, we proceed to find the ratio that best describes the dynamics and future evolution of the merging galaxies. Although using the H-band flux ratio selection is biased towards star-forming but low stellar mass satellites, the use of the stellar mass ratio may be biased against gas-rich satellites at $z > 1$. Galaxies appear to be more gas-rich at higher redshift and at lower masses (Erb et al., 2006; Mannucci et al., 2009; Stewart et al., 2009a; Conselice et al., 2013). Such dependence implies that the baryon mass ratio is closer to unity than the stellar mass ratio, since cold gas mass is included into the baryon mass calculation. The baryon mass of a galaxy is a better probe of its total mass (which also includes dark matter) than the stellar mass alone, as shown in cosmological simulations (Stewart et al., 2009a; Hopkins et al., 2010d). A merger can be *major* or *minor* depending on whether the stellar mass, baryon mass or total mass is considered for the mass ratio (Stewart et al., 2009a; Lotz et al., 2011). Intermediate mass galaxies of $\log(M_\star/M_\odot) \sim 9.8 - 10.8$ are the satellites to the massive galaxies studied here, and their molecular gas mass may not be negligible in the total mass budget that governs the dynamics of the galaxies, especially at $z \sim 2$. If the cold gas fraction increases with redshift and decreases with stellar mass as previously claimed (Stewart et al., 2009b), there is a redshift-dependent underestimation if we use the stellar mass to trace the baryon mass. The correction is likely larger at higher redshift due to the higher gas fraction. Therefore merging with these gas-rich satellites with stellar mass ratios more extreme than 10:1 may contribute to the star formation budget of the massive galaxies (Conselice et al., 2013), in the form of gas accretion or

very minor mergers if characterized by the stellar mass ratio. We note that gas-rich satellites are not equivalent to gas-rich mergers (e.g. Tadaki et al., 2014), which is usually defined as the average gas fraction of both galaxies. Despite the importance of the gas content in the merger definition as well as its contribution to star formation activity, direct measurements of the molecular gas mass are so far only available for limited samples of galaxies (Daddi et al., 2010; Tacconi et al., 2010; Bothwell et al., 2013; Tacconi et al., 2013), mostly starbursting sub-millimeter galaxies. ALMA surveys of large samples of “normal" star-forming galaxies will shed light on this topic in the future (Scoville et al., 2014).

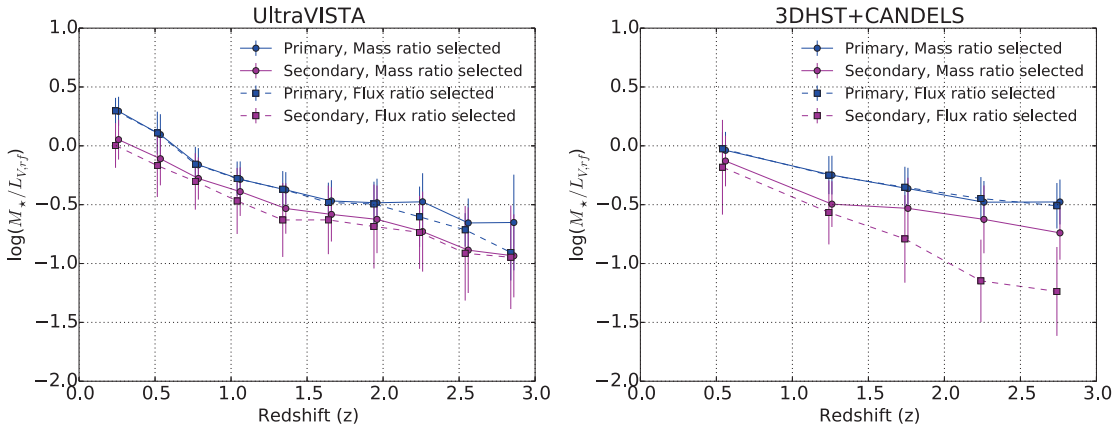

Figure 3.2: We plot the median stellar mass-to-light ratio against redshift for the UltraVISTA and the 3DHST+CANDELS merger samples. The stellar mass-to-light ratio ($M_\star/L_V$) is the stellar mass divided by the luminosity of the rest-frame V-band from InterRest. The primary (secondary) galaxies refer to the massive galaxies (satellites), and are plotted in blue (magenta). We compare the stellar mass ratio (solid) and flux ratio (dotted) selected mergers. The error bars show the standard deviation of the $M_\star/L_V$ in each redshift bin. We confirm that for flux ratio selected mergers from 3DHST+CANDELS, the $M_\star/L_V$ of the satellites evolve more steeply than mass ratio selected mergers. This supports our finding that the H-band flux ratio selection includes satellites with comparable brightness as the massive galaxies, but much lower stellar masses. The varying $M_\star/L_V$ evolution provides the explanation for the discrepancy in the measured merger fractions at $z > 2$.

Table 3.1. Best fitting functions to merger fractions and rates

Catalog	Selection	Merger fraction	Merger rate
		Major	
UltraVISTA	Stellar mass ratio	$(-5.25 \pm 0.74)(1+z)^2 + (25.67 \pm 3.50)(1+z) + (-20.36 \pm 3.88)$	$(0.06 \pm 0.02)(1+z)^{0.41 \pm 0.33}$
UltraVISTA	H_{160} flux ratio	$(-7.16 \pm 1.08)(1+z)^2 + (33.54 \pm 5.22)(1+z) + (-24.09 \pm 5.88)$	$(0.13 \pm 0.04)(1+z)^{-0.03 \pm 0.32}$
3DHST	Stellar mass ratio	$(9.71 \pm 2.14)(1+z)^{-0.47 \pm 0.24}$	$(0.14 \pm 0.03)(1+z)^{-0.53 \pm 0.22}$
3DHST	H_{160} flux ratio	$(7.81 \pm 1.44)(1+z)^{0.56 \pm 0.19}$	$(0.11 \pm 0.02)(1+z)^{0.57 \pm 0.19}$
		Minor	
UltraVISTA	Stellar mass ratio	$(4.61 \pm 0.99)(1+z)^{0.88 \pm 0.31}$	$(0.04 \pm 0.01)(1+z)^{1.07 \pm 0.26}$
UltraVISTA	H_{160} flux ratio	$(6.96 \pm 1.11)(1+z)^{0.58 \pm 0.24}$	$(0.07 \pm 0.01)(1+z)^{0.55 \pm 0.27}$
3DHST	Stellar mass ratio	$(9.34 \pm 4.6)(1+z)^{-0.46 \pm 0.57}$	$(0.11 \pm 0.05)(1+z)^{-0.69 \pm 0.56}$
3DHST	H_{160} flux ratio	$(5.21 \pm 1.51)(1+z)^{0.97 \pm 0.3}$	$(0.06 \pm 0.01)(1+z)^{0.92 \pm 0.27}$

Note. — The best fitting functions of the measured merger fractions and rates. We quote the power law as long as the reduced χ^2 is less than 10, and otherwise we use the quadratic function as it proves to be a better fit for the concave shape of the UltraVISTA major merger fractions. The parameters are determined by a least square fit to the data points which are complete to low surface brightness satellites. We note that the $(1+z)$ dependence are similar for the merger fractions and rates, since a constant observability timescale from Lotz et al. (2010) is applied for the conversion.

Table 3.2. Merger fraction: Stellar mass ratio selected

		Major				Minor			
Redshift range	$N_{\rm massive}$	$N_{\rm match\ z}$	$N_{\rm missing\ z}$	$N_{\rm not\ match\ z}$	$f_{\rm major}[\%]$	$N_{\rm match\ z}$	$N_{\rm missing\ z}$	$N_{\rm not\ match\ z}$	$f_{\rm minor}[\%]$
UltraVISTA DR1									
$0.1 < z \leq 0.4$	628	23	12	201	$3.66^{+0.93}_{-0.76}$	29	6	170	$4.62^{+1.03}_{-0.85}$
$0.4 < z \leq 0.65$	772	40	4	99	$5.18^{+0.96}_{-0.82}$	52	3	117	$6.74^{+1.07}_{-0.93}$
$0.65 < z \leq 0.9$	1618	158	2	170	$9.77^{+0.78}_{-0.78}$	146	6	179	$9.02^{+0.75}_{-0.75}$
$0.9 < z \leq 1.2$	1692	184	6	169	$10.87^{+0.8}_{-0.8}$	140	9	140	$8.27^{+0.7}_{-0.7}$
$1.2 < z \leq 1.5$	1426	142	5	133	$9.96^{+0.84}_{-0.84}$	134	10	143	$9.4^{+0.81}_{-0.81}$
$1.5 < z \leq 1.8$	1163	133	8	99	$11.44^{+0.99}_{-0.99}$	81	13	102	$\dagger 6.96^{+0.86}_{-0.77}$
$1.8 < z \leq 2.1$	1087	99	9	97	$9.11^{+1.01}_{-0.91}$	42	20	125	$\dagger 3.86^{+0.69}_{-0.59}$
$2.1 < z \leq 2.4$	560	40	9	63	$7.14^{+1.32}_{-1.12}$	15	4	63	$\dagger 2.68^{+0.88}_{-0.68}$
$2.4 < z \leq 2.7$	536	28	13	56	$\dagger 5.22^{+1.18}_{-0.98}$	18	9	73	$\dagger 3.36^{+0.99}_{-0.78}$
$2.7 < z \leq 3.0$	347	20	3	31	$\dagger 5.76^{+1.6}_{-1.28}$	10	4	46	$\dagger 2.88^{+1.23}_{-0.89}$
3DHST COSMOS									
$0.1 < z \leq 1.0$	123	10	1	43	$8.13^{+3.46}_{-2.52}$	7	1	44	$5.69^{+3.06}_{-2.09}$
$1.0 < z \leq 1.5$	61	3	0	9	$4.92^{+4.79}_{-2.69}$	5	0	14	$8.2^{+5.54}_{-3.54}$
$1.5 < z \leq 2.0$	88	5	0	14	$5.68^{+3.84}_{-2.45}$	9	1	16	$10.23^{+4.66}_{-3.34}$
$2.0 < z \leq 2.5$	63	6	0	20	$9.52^{+5.68}_{-3.77}$	5	1	18	$7.94^{+5.37}_{-3.43}$
$2.5 < z \leq 3.0$	45	0	0	7	$0.0^{+0.0}_{0.0}$	3	1	7	$\dagger 6.67^{+6.49}_{-3.64}$
3DHST GOODS-N									
$0.1 < z \leq 1.0$	84	3	2	22	$3.57^{+3.48}_{-1.95}$	6	5	35	$7.14^{+4.26}_{-2.83}$
$1.0 < z \leq 1.5$	72	6	2	13	$8.33^{+4.97}_{-3.3}$	7	2	13	$9.72^{+5.23}_{-3.58}$
$1.5 < z \leq 2.0$	57	1	2	7	$1.75^{+4.04}_{-1.45}$	3	2	4	$5.26^{+5.12}_{-2.88}$
$2.0 < z \leq 2.5$	65	1	0	6	$1.54^{+3.54}_{-1.27}$	1	3	13	$1.54^{+3.54}_{-1.27}$
$2.5 < z \leq 3.0$	37	0	0	6	$0.0^{+0.0}_{0.0}$	1	0	9	$\dagger 2.7^{+6.22}_{-2.24}$
3DHST GOODS-S									
$0.1 < z \leq 1.0$	66	4	0	11	$6.06^{+4.79}_{-2.89}$	6	2	25	$9.09^{+5.42}_{-3.6}$
$1.0 < z \leq 1.5$	77	6	1	9	$7.79^{+4.64}_{-3.08}$	4	1	11	$5.19^{+4.1}_{-2.48}$
$1.5 < z \leq 2.0$	74	3	0	9	$4.05^{+3.95}_{-2.22}$	6	5	12	$8.11^{+4.83}_{-3.21}$
$2.0 < z \leq 2.5$	47	2	0	7	$4.26^{+5.62}_{-2.77}$	2	0	8	$4.26^{+5.62}_{-2.77}$
$2.5 < z \leq 3.0$	39	4	0	6	$10.26^{+8.1}_{-4.9}$	2	1	7	$\dagger 5.13^{+6.77}_{-3.33}$
3DHST AEGIS									
$0.1 < z \leq 1.0$	102	8	3	54	$7.84^{+3.86}_{-2.71}$	3	5	76	$2.94^{+2.86}_{-1.61}$
$1.0 < z \leq 1.5$	124	7	4	23	$5.65^{+3.04}_{-2.08}$	11	10	38	$8.87^{+3.56}_{-2.63}$
$1.5 < z \leq 2.0$	141	19	1	31	$13.48^{+3.85}_{-3.06}$	9	5	22	$6.38^{+2.91}_{-2.08}$
$2.0 < z \leq 2.5$	86	5	3	16	$5.81^{+3.93}_{-2.51}$	3	1	21	$3.49^{+3.4}_{-1.91}$
$2.5 < z \leq 3.0$	54	4	1	8	$7.41^{+5.85}_{-3.54}$	1	3	14	$\dagger 1.85^{+4.26}_{-1.53}$
3DHST UDS									
$0.1 < z \leq 1.0$	87	11	6	29	$12.64^{+5.07}_{-3.75}$	9	6	19	$10.34^{+4.72}_{-3.38}$
$1.0 < z \leq 1.5$	103	5	2	13	$4.85^{+3.28}_{-2.1}$	8	4	17	$7.77^{+3.82}_{-2.68}$
$1.5 < z \leq 2.0$	162	11	2	15	$6.79^{+2.72}_{-2.01}$	11	2	38	$6.79^{+2.72}_{-2.01}$
$2.0 < z \leq 2.5$	98	3	0	12	$3.06^{+2.98}_{-1.67}$	2	2	10	$2.04^{+2.69}_{-1.33}$
$2.5 < z \leq 3.0$	65	4	0	11	$6.15^{+4.86}_{-2.94}$	0	2	16	$\dagger 0.0^{+0.0}_{0.0}$

Note. — This table presents the number counts of massive galaxies and mergers, as well as the merger fractions in different redshift bins for the UltraVISTA catalog and the five individual fields of the 3DHST+CANDELS catalog. The number of massive galaxies is denoted by $N_{\rm massive}$. The numbers of major (stellar mass ratio 1:1 - 4:1) and minor (stellar mass ratio 4:1 - 10:1) pairs with projected separation $R_{proj} = 10 - 30$ kpc h^{-1} are further separated according to their photo-z information: $N_{\rm match\ z}$ ($N_{\rm not\ match\ z}$) is the number of pairs with photo-z's (not) matching within their 1σ uncertainties as described in Section 3.2.3; $N_{\rm missing\ z}$ is the number of pairs with one or both galaxies not having accurate photo-z's (`odds` < 0.95). The major and minor merger fractions are calculated as $f = N_{\rm match\ z}/N_{\rm massive}$ in percentages, and their uncertainties are propagated from the Poisson errors of $N_{\rm match\ z}$. The † symbols on the merger fractions indicate the redshift bins in which faint, low surface brightness satellites may be incomplete according to Appendix 3.A.2.

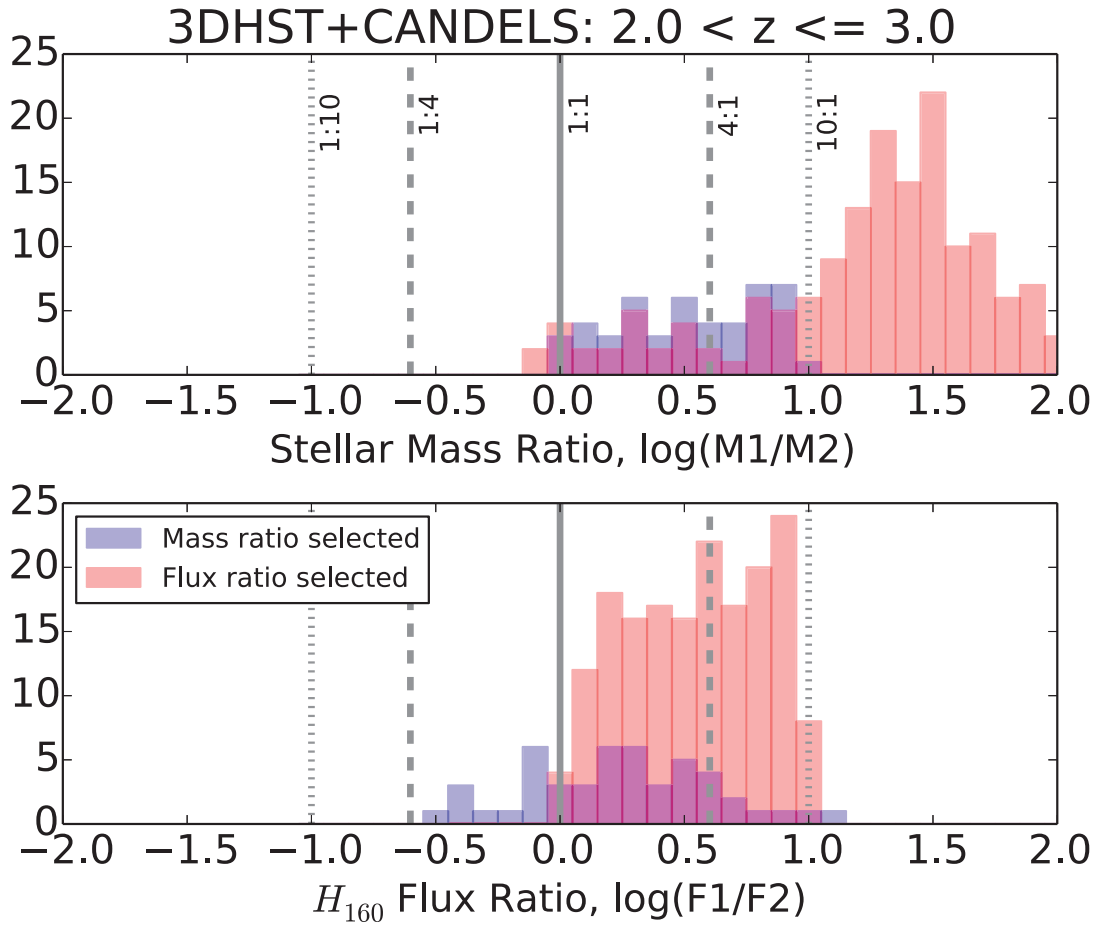

Figure 3.3: These histograms compare the mergers at $2 < z \leqslant 3$ selected by stellar mass ratio (blue) or H_{160} flux ratio (red) from the 3DHST+CANDELS catalog. The ratios are defined such that the mass- (flux-)ratio selected mergers will have ratios of 1 - 10. On the top panel we show the histogram of the stellar mass ratios, and at bottom the histogram of the H_{160} flux ratios. The solid, dashed and dotted gray lines represent the 1:1, 1:4 & 4:1, 1:10 & 10:1 ratios respectively. From the top panel, we observe that a large excess of flux ratio selected mergers in 3DHST+CANDELS have H_{160} flux ratios between 1 and 10, but have stellar mass ratios between 10 and 100. This explains the rising merger fractions observed in Figure 3.1 (right) due to bright satellites with $\log(M_\star/M_\odot) < 9.8$ being included in the flux ratio selected sample.

3.3.1.2 Cosmic variance

It is apparent from Figure 3.4 that a considerable scatter exists for the merger fractions measured in the individual fields of the 3DHST+CANDELS. The small survey area ($\sim$0.05deg^2 for each of the five fields) could lead to systematic uncertainties com-

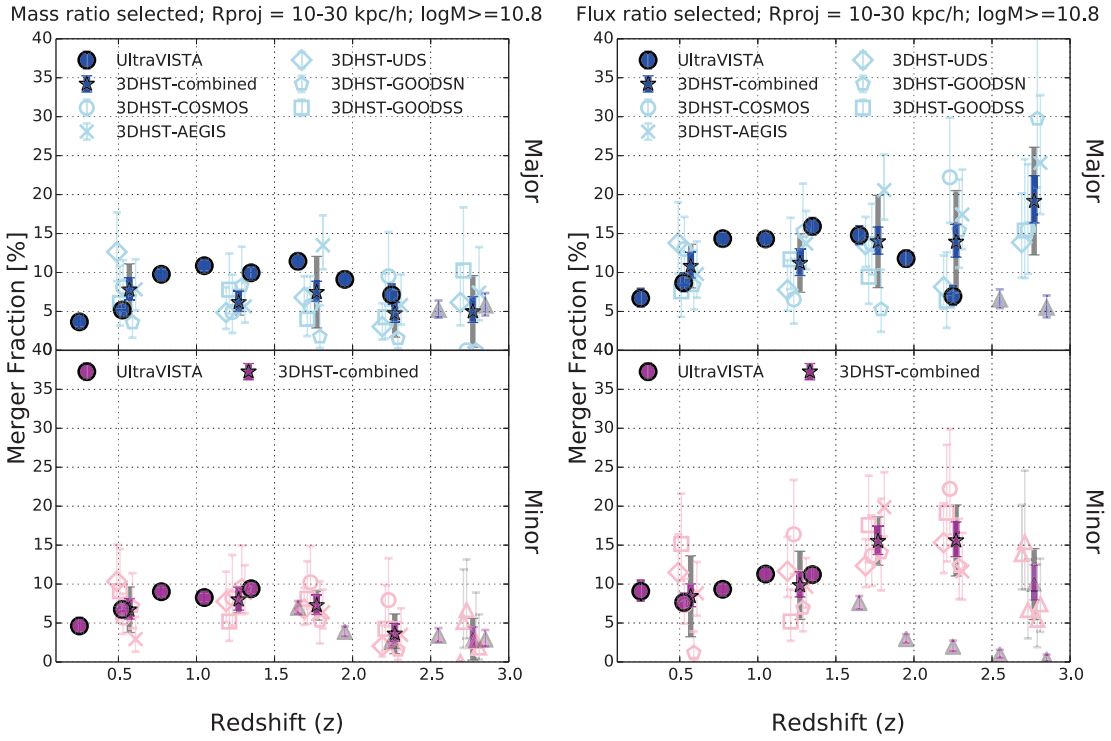

Figure 3.4: The merger fraction measured individually from each of the five 3DHST+CANDELS fields (COSMOS, GOODS-N & GOODS-S, AEGIS, and UDS) plotted in light blue (major) and pink (minor) with open symbols as indicated in the legend. The combined mean from the five fields are plotted as filled stars. The Poisson uncertainties of the combined number of pairs are plotted as the blue / magenta error bars, and the standard deviation of the merger fraction of individual fields from the combined mean is shown as gray error bars. We can see that cosmic variance is a prominent source of uncertainty for the 3DHST+CANDELS merger fractions. The UltraVISTA merger fractions are shown for comparison in filled circles. For both catalogs we use triangles to indicate the high redshift regimes in which the catalogs are estimated to be incomplete for low surface brightness satellites. As in the preceding plots, the top panels show major mergers (mass ratio 1:1 - 4:1) and the bottom panels show minor mergers (mass ratio 4:1 - 10:1) around massive ($\log(M_\star/M_\odot) \geqslant 10.8$) galaxies. The left plots show the stellar mass ratio selected mergers, and the right plots show the H-band flux ratio selected mergers. The mergers are selected to have overlapping photo-z's and projected separation between 10 - 30 kpc h^{-1} as described in Section 3.2.3.

parable to or larger than the Poisson uncertainties. We list the fractional errors ($\sigma = \delta f/f$) of the merger fraction measurements of the CANDELS+3DHST sample in Table 3.3. The Poisson uncertainties of the merger fractions are calculated as $\delta f_{Poisson} = \delta N_{pair,Poisson}/N_{massive}$. We compute the standard deviation of the merger fraction in each field from the combined mean as $\delta f_{total} = \sqrt{\sum_{i=1}^{5}(f_i - \overline{f})^2/(5-1)}$, where i repre-

Table 3.3. Error budget for merger fraction measurements in 3DHST+CANDELS

Redshift range	$f_{\rm major}[\%]$	$\sigma_{major,Poisson}$	$\sigma_{major,CV}$	$\sigma_{major,total}$	$f_{\rm minor}[\%]$	$\sigma_{minor,Poisson}$	$\sigma_{minor,CV}$	$\sigma_{minor,total}$
$0.1 < z \leq 1.0$	7.8	0.18	0.39	0.43	6.7	0.20	0.39	0.44
$1.0 < z \leq 1.5$	6.2	0.21	0.16	0.27	8.0	0.18	0.11	0.21
$1.5 < z \leq 2.0$	7.5	0.17	0.59	0.61	7.3	0.18	0.19	0.26
$2.0 < z \leq 2.5$	4.7	0.27	0.58	0.64	3.6	0.32	0.63	0.70
$2.5 < z \leq 3.0$	5.0	0.33	0.86	0.92	2.9	0.45	0.80	0.92

Note. — A table comparing the dominant sources of uncertainties of the merger fractions for the stellar mass ratio selected mergers in 3DHST+CANDELS fields. The fractional error is calculated by the ratio of the error to the merger fraction ($\sigma = \delta f/f$). Here we compute the Poisson error of the total pair counts combining the five 3DHST fields ($\delta f_{\rm Poisson} = \delta N_{\rm pair,Poisson}/N_{\rm massive}$). The total error is the standard deviation of the merger fraction of each field compared to the combined merger fraction ($\delta f_{total} = \sqrt{\sum_{i=1}^{5}(f_i - \overline{f})^2/(5-1)}$). The cosmic variance (CV) is calculated by the errors in excess to the expected Poisson errors of the merger fraction in the five fields, i.e. $\sigma^2_{CV} = \sigma^2_{total} - \sigma^2_{Poisson}$. The cosmic variance is a dominant source of uncertainty for merger fraction measurements using 3DHST+CANDELS, having comparable to or sometimes larger contribution than than the Poisson uncertainty.

sents the measurement of each of the five fields. The cosmic variance is simply the observed variance in excess of the Poisson random noise, given by $\sigma^2_{CV} = \sigma^2_{total} - \sigma^2_{Poisson}$. The cosmic variance is a comparable or sometimes larger contributor to the total error budget of the merger fraction measurements than the Poisson uncertainty, as visualized in Figure 3.4. More specifically, in the redshift range of $z = 1.5 - 2.0$ the f_{major} measured from AEGIS is $13.5^{+3.9}_{-3.1}\%$, whereas the same quantity is measured to be $1.8^{+4.0}_{-1.5}\%$ in GOODS-N. While each of these quantities are $\sim 1.5\sigma$ from the $\overline{f}$ averaged over the five CANDELS fields, if the individual measurements are taken at face value without including the cosmic variance in the error budget, the results can differ by a maximum of $\sim 7.7\times$ depending on the field used. Combining the measurements from the five CANDELS fields is crucial to mitigate cosmic variance, also known as the field-to-field variance (Grogin et al., 2011).

The cosmic variance affecting the merger fraction measurements depends primarily on the number densities of the massive galaxies and their satellites, as well as the cosmic volume probed, as shown by López-Sanjuan et al. (2014). Here we use their parameterization to estimate the relative cosmic variance for the UltraVISTA and 3DHST+CANDELS samples. If we assume that the number densities of the massive galaxies and their satellites are not different in UltraVISTA than in the combined five fields of 3DHST+CANDELS, the cosmic variance has a dependence on the comoving

volume as $\sigma_{CV} \propto V_c^{-0.48}$. Since the comoving volume is proportional to the survey area, and UltraVISTA covers $\sim 6.5\times$ larger area than the fields of 3DHST+CANDELS combined, we expect the σ_{CV} of UltraVISTA to be $\sim 0.41\times$ that of 3DHST+CANDELS. Another prominent error of the merger fraction is the Poisson number count of pairs. As $\sigma_{\rm Poisson}$ is proportional to $1/\sqrt{N_{\rm pair}}$, and again assuming similar number densities of satellites in both fields, we expect $N_{\rm pair} \propto Area$ and therefore the Poisson errors should be $\sim 0.39\times$ smaller in UltraVISTA than that in 3DHST+CANDELS. This implies that the total fractional error of merger fraction measured from UltraVISTA to be 56% that of 3DHST+CANDELS.

To summarize, we caution against drawing conclusions from merger fraction measurements based on individual CANDELS-sized fields. The merger fraction measurements from the five 3DHST+CANDELS fields combined are comparable to those from UltraVISTA which covers $\sim 6.5\times$ larger area, albeit with larger Poisson uncertainties and in coarser redshift bins. We call for including cosmic variance as a systematic uncertainty for pencil beam surveys such as 3DHST+CANDELS for merger fraction measurements (Somerville et al., 2004; Moster et al., 2011; Xu et al., 2012a).

3.3.2 WHY ARE THERE SO FEW MINOR MERGERS?

Minor dry mergers are often invoked as the primary driver of the observed size evolution of quiescent massive galaxies from $z \sim 2$ to 0. Predictions from numerical simulations and virial arguments (Bezanson et al., 2009; Naab et al., 2009; Laporte et al., 2013) suggest that they are more efficient than major dry mergers in puffing up the sizes of quiescent galaxies per unit mass added. From previous minor merger fraction measurements (Williams et al., 2010; Newman et al., 2012) and this work (see Section 3.3.3) it is inferred that massive galaxies undergo less than one minor merger since $z \sim 2$. However, if the sole explanation of the observed size evolution is minor merging, multiple minor mergers are required (e.g. Hilz et al., 2012; Oser et al., 2012; Hilz et al., 2013). Here we investigate the possibilities of missing faint satellites to massive galaxies at $z > 1.5$.

3.3.2.1 Are we missing minor mergers because of observational bias?

As discussed in Section 3.3.1.1, we find that neither the major nor minor merger fractions in the CANDELS deep fields are higher than those in the CANDELS wide fields, although measurements from individual fields are subject to high cosmic variance (see Section 3.3.1.2). Additionally, the merger fractions from stellar mass ratio selected mergers of UltraVISTA and 3DHST+CANDELS are remarkably consistent (Figure 3.1, left), even in the redshift bins where UltraVISTA is incomplete for low surface brightness galaxies. Even though the CANDELS *H*-band imaging is >3 magnitudes deeper and has $> 4\times$ smaller PSF compared to UltraVISTA, UltraVISTA has the advantage that

it probes a redder band (*Ks*) where high redshift galaxies are brighter.

To make a robust claim that we do not miss minor mergers lying just below the surface brightness limits (SB) of our surveys, we refer to the simulation performed for the completeness limits as introduced in Appendix 3.A.2. In short, we confirm that we do not miss minor mergers up to $z = 2.5$ in 3DHST+CANDELS. We arrive at this conclusion by making the most conservative assumption that the faintest possible satellite is a maximally old, dust-free galaxy of $\log(M_\star/M_\odot) = 9.8$ for a range of light profiles. The completeness limits hold except for the extreme cases not simulated: (1) they have very compact sizes ($R_e < 0.39$ kpc) and Sersic index $n > 4$ so that they have insufficient contiguous pixels above the detection threshold; (2) they have very large sizes ($R_e > 1.95$ kpc) and low $n < 0.5$ so they have low SB; (3) their dust extinction causes them to be fainter than a dust-free maximally old galaxy. These size limits are motivated by the scaling relations for quiescent or early-type galaxies (Williams et al., 2010; Newman et al., 2012; Cassata et al., 2013) and simulation assumptions regarding the size of the stellar halo (Hilz et al., 2012). Unless these intermediate mass galaxies have light profiles very different from the more massive galaxies at similar redshift and similar mass galaxies at lower redshifts, (1) and (2) are not likely explanations. The rest-frame optical faintest galaxies at $z > 2$ should be quiescent and therefore should be dust-free, therefore (3) is not a likely explanation either.

From binary merger simulations (Lotz et al., 2010), the observability timescales of major and minor mergers are very short at $R_{proj} < 15$ kpc h^{-1} (< 0.1 Gyr) and therefore we do not expect many close pairs blended by the PSF. As long as the lower R_{proj} limit for the close pair search is set according to the seeing and SB limit of the data, the resolution is not expected to cause a bias in the merger fraction.

3.3.2.2 What do we expect for the minor merger fraction?

As lower mass galaxies are more abundant than massive galaxies, one may expect that minor mergers are more frequent than major mergers from a statistical argument. Minor mergers are expected to be visible as pairs for longer than major mergers, according to dynamical friction timescales arguments and binary simulations (Lotz et al., 2010). Therefore one intuitively expects the minor merger fraction and rate to be higher than the major ones. However, cosmological simulations indicate that the major and minor merger rates are comparable in the stellar mass range probed in this work (Croton et al., 2006; Maller et al., 2006; Somerville et al., 2008; Stewart et al., 2009a; Hopkins et al., 2010d; Cattaneo et al., 2011) due to the stellar mass dependence on the $M_\star - M_{halo}$ relation.

With our large complete sample of mergers, we can study the relative fractions of mergers of different stellar mass ratios (μ). We present our merger fractions in various μ bins in Figure 3.5. The merger fraction decreases as the μ gets more extreme. The minor

($4 \leqslant \mu \leqslant 10$) merger fractions are comparable to the major merger ($1 \leqslant \mu \leqslant 4$) fractions at all redshifts. This is in qualitative agreement with previous observations (López-Sanjuan et al., 2010; Newman et al., 2012; Williams et al., 2011). For our sample of stellar mass ratio selected mergers from both datasets, the geometric number-weighted mean stellar mass ratio is $< \mu_n > \sim$ 4:1 - 5:1 and the mass-weighted mean stellar mass ratio is $< \mu_m > \sim$ 3:1 - 4:1. This is in consistency with various model predictions (Cattaneo et al., 2011; Lackner et al., 2012; Gabor & Davé, 2012) except Oser et al. (2012), who find $< \mu_m > \sim$ 5:1 but $< \mu_n > \sim$ 16:1. Their simulation is able to resolve down to 100:1 mergers, whereas we impose a cut at 10:1 mergers. We attribute the discrepancy to a higher minor merger rate of their simulated massive galaxies, as well as our imposed cutoff at μ=10:1.

3.3.3 Converting merger fractions to merger rates

The goal of measuring the galaxy merger fraction is to determine the time integral of the merger rate, defined as the number of mergers ($\mathbb{N}$) that a massive galaxy experiences on average over a time span. The merger rate can be compared to the observed evolution of the galaxy population, such as in numbers, mass, size, etc., so that we can infer if galaxy merging is likely a driver.

Merger rates scale as the number of mergers ($N_{merge,actual}$) occurred during the time span (Δt) defined by the redshift bin, divided by the time span, (Rate $\propto N_{merge,actual}/\Delta t$). We measure Γ as the number of observed merging galaxies ($N_{merge,obs}$) divided by the observability timescale of mergers (τ_{obs}), i.e. Rate $\propto N_{merge,actual}/\Delta t = N_{merge,obs}/\tau_{obs}$. The two common definitions of merger rates can be generalized as follows (Lotz et al., 2011, and references therein):

(1) The number of merger events per unit time per unit volume (Γ):

$$\Gamma(z)[Gyr^{-1}Mpc^{-3}] = \frac{N_{merge,obs}(z)/\tau_{\rm obs}}{V_{\rm comoving}(z)} = \frac{n_{\rm merge}}{\tau_{\rm obs}} \tag{3.3.1}$$

where $N_{merge,obs}(z)$ refers to the number of major (or minor) satellites around massive galaxies in that redshift, $\tau_{\rm obs}$ is the average observable timescale for the mergers of the mass ratio range observed to be within R_{proj}, and $V_{\rm comoving}$ is the comoving volume projected by the survey area within the concerned redshift interval.

(2) The number of merger events per galaxy per unit time ($\mathbb{R}$) is defined as:

$$\mathbb{R}(z)[Gyr^{-1}] = \frac{\Gamma(z)}{n_{\rm massive}(z)} = \frac{n_{\rm merge}}{n_{\rm massive}\tau_{\rm obs}} = \frac{f_{\rm merge}}{\tau_{\rm obs}} \tag{3.3.2}$$

where $n_{\rm massive}$ is the number density of massive galaxies per unit volume.

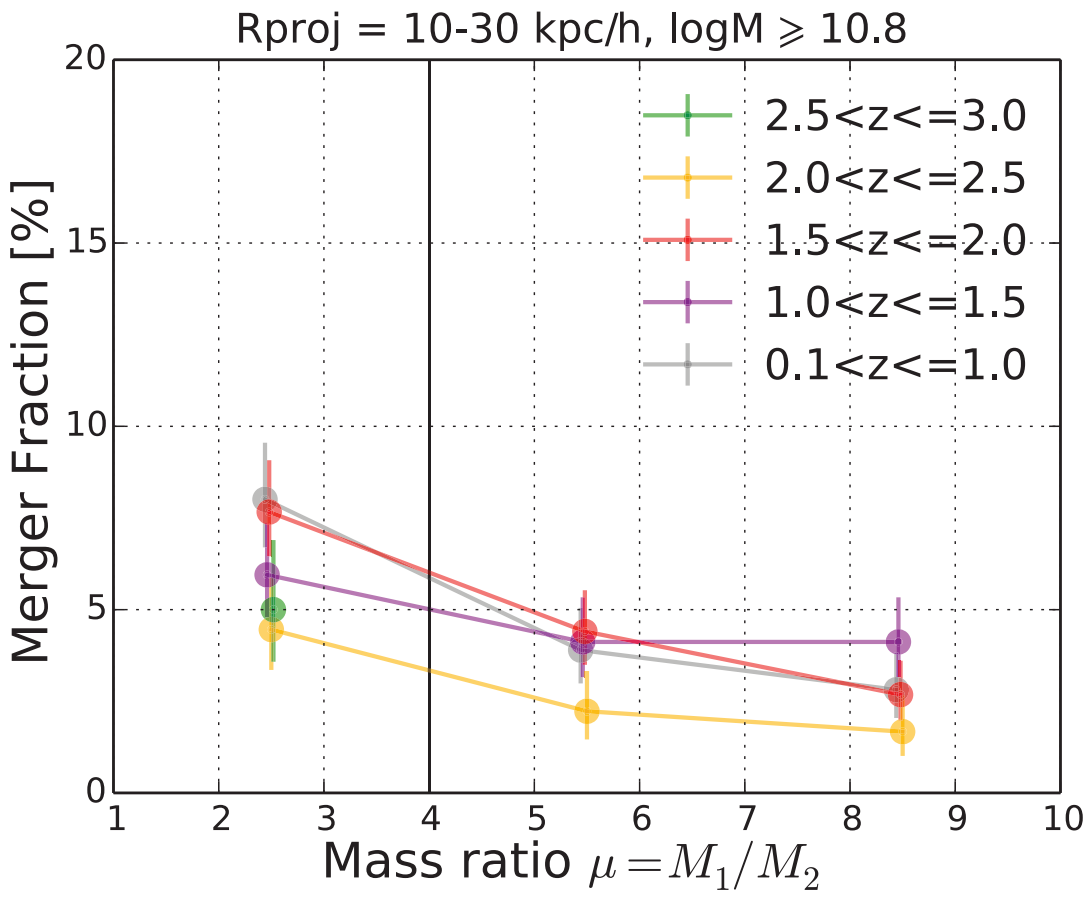

Figure 3.5: The dependence of stellar mass ratio selected merger fractions on the stellar mass ratio at different redshifts. We note that the distribution of stellar mass ratios is remarkably insensitive to the catalog used (UltraVISTA or 3DHST+CANDELS) and the selection method (stellar mass ratio or H-band flux ratio), except for a declining tail towards lower stellar mass ratios for the H-band flux ratio selection as discussed in Section 3.3.1.1. On this plot we display the stellar mass selected ratio mergers from 3DHST+CANDELS for illustration. Only the data points in which they are complete in stellar mass and surface brightness are shown (see Table 3.A.1). The major merger fractions appear to be comparable to the minor merger fractions at all redshifts.

The number of mergers a massive galaxy undergoes on average (N_{merger}) is simply the time integral of the merger rate per galaxy:

$$N_{merger} = \int_{t_1}^{t_2} \mathbb{R}(z) dt = \int_{z_1}^{z_2} \frac{\mathbb{R}(z)\ t_H}{(1+z)\ E(z)} dz \tag{3.3.3}$$

where t_H is the Hubble time, and $E(z) = H(z)/H(0) = [\Omega_M(1+z)^3 + \Omega_k(1+z)^2 + \Omega_\Lambda]^{1/2}$ (Peebles, 1993) with the Ω's denoting the density parameters.

3.3.3.1 Merger (observability) timescales

Merger rates can be inferred by observing the merger fraction as a function of redshift, and then a merging timescale is assumed to convert the fraction to a rate. The assumed merging timescale either comes from binary merger simulations (Lotz et al., 2010), cosmological simulations (Kitzbichler & White, 2008), or approximation using the dynamical friction timescale. Here we briefly discuss the various options and justify the merger timescales used in this work.

The dynamical friction timescale (Bell et al., 2006a; Boylan-Kolchin et al., 2008; Jiang et al., 2008) is a suitable approximation for dark matter halo mergers of large mass ratios (i.e. minor mergers). However, it remains uncertain whether it can describe mergers with baryons or major mergers in which violent relaxation is the dominant mechanism determining the duration of the merger.

The timescales from binary simulations and cosmological simulations are conceptually distinct. In binary merger simulations (e.g. Lotz et al., 2010), two galaxies are set on approaching orbits, and the observability timescale (τ_{obs}) samples the distribution of pre-coalescence pairs as a function of R_{proj}. The timescale τ_{obs} is a well-defined quantity which is directly applicable to the merger fraction to rate conversion. This direct simulation method provides an accurate and comprehensible description of merging for the assumed conditions of relative velocity, gas fraction, morphology, etc. On the other hand, merging timescale (τ_{merge}) defined in cosmological simulations (Kitzbichler & White, 2008) depends on how the start and end of merging are defined, for example whether the end is the final coalescence of the two galaxy cores or when most of the mass of the satellite galaxy is deposited onto the massive one. Another complication is that there are different treatments of mapping stellar masses to the DM halos in cosmological simulations (e.g. Berrier et al., 2006; Kitzbichler & White, 2008). We note that merging timescales for major mergers derived using cosmological simulations are shown to be $\sim 1-2$Gyr longer compared with simulations that include baryons (McCavana et al., 2012). Most importantly, τ_{obs} instead of τ_{merge} should be used to convert the observed fractions into rates. Therefore in this work we use the τ_{obs} from Lotz et al. (2010). The cosmological simulations are useful to weigh the timescales of mergers from binary simulations with different assumptions, such as gas fraction, orbital parameters, as discussed in details in Lotz et al. (2011). Due to the systematic uncertainties in these assumptions, as well as random uncertainties due to viewing angles of pairs projected in 2D, the merging (observability) timescale can only be determined at best to 50% accuracy (Hopkins et al., 2010d, and references therein).

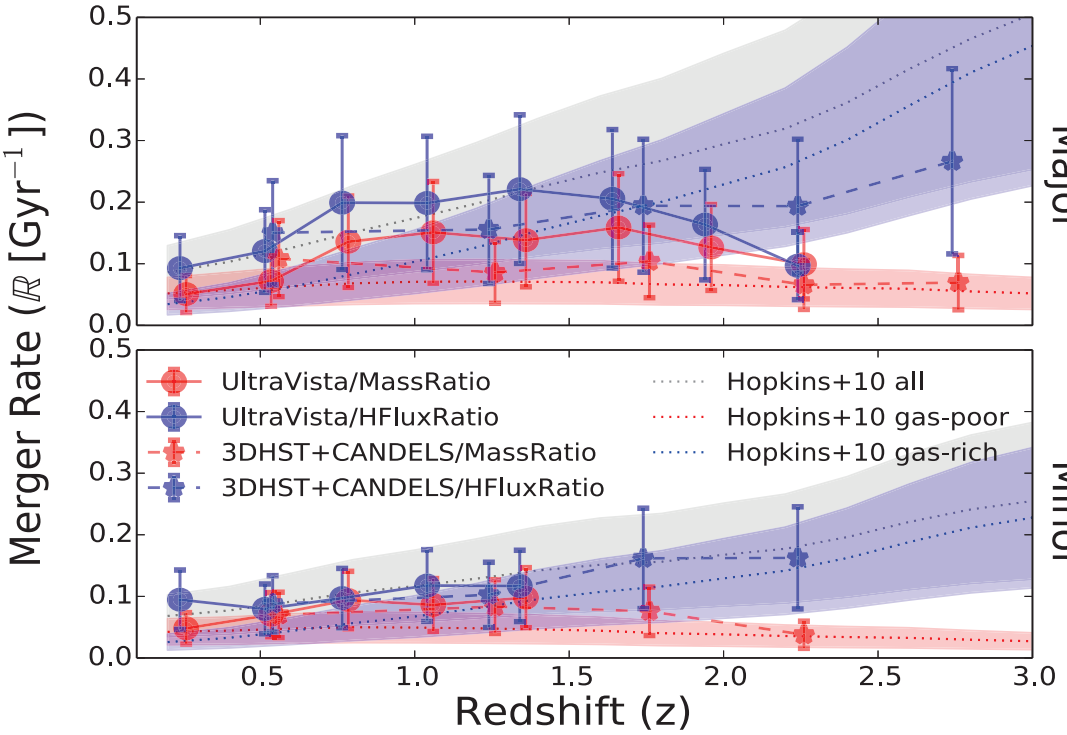

Figure 3.6: The redshift evolution of the major (top) and minor (bottom) merger rates ($\mathbb{R}$) based on our observed merger fractions of UltraVISTA (filled circles, solid lines) and 3DHST+CANDELS (filled stars, dashed lines). We compare the merger selections using the stellar mass ratios (red) and H_{160}-band flux ratios (blue). The merger rates are computed following Equation (3.3.2) using the 10-30 kpc h^{-1} close pairs and the observability timescale of Lotz et al. (2010). The data points are only plotted in the redshift range in which we are complete in detecting the faintest possible satellites. We overplot the predicted galaxy merger rates from the simulation of Hopkins et al. (2010c) for comparison. The predicted merger rates are plotted as dotted lines with the shades indicating the 50% uncertainties, where gray represents mergers of all gas fractions (f_{gas}), and red and blue represents gas-poor ($f_{gas} = 0 - 20\%$) and gas-rich ($f_{gas} = 20 - 100\%$) merger rates.

3.3.3.2 Merger rates

The merger rates derived using Equations (3.3.2) and (3.3.3) normalized to timescales of 1 Gyr are shown in Table 3.4. We plot the inferred merger rates on Figure 3.6. As expected from the merger fractions, we find the merger rates from UltraVISTA are consistent with those from 3DHST+CANDELS within the completeness range, and that the flux ratio selection method gives an increasing trend while the stellar mass ratio selection method gives a flat or diminishing trend for the 3DHST+CANDELS catalog. We list the best fitting parameters for the observed merger rates to a power law in Table 3.1

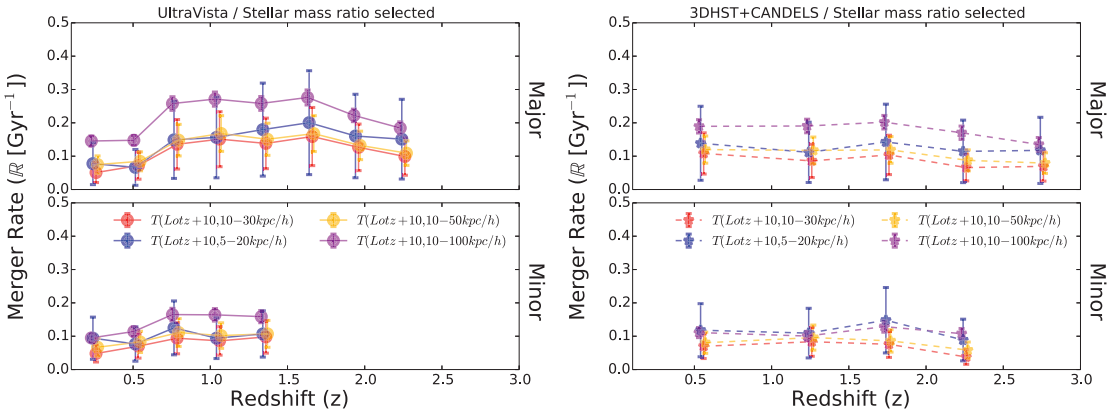

Figure 3.7: Similar to Figure 3.6, these figures present the major (top) and minor (bottom) merger rate evolution. We compare the merger rates inferred from galaxy pairs of different R_{proj} bins: 10-30 kpc h^{-1} (red, default), 5-20 kpc h^{-1} (blue), 10-50 kpc h^{-1} (yellow) and 10-100 kpc h^{-1} (purple). The left and right figures show the results of the stellar mass ratio selected mergers in UltraVISTA and 3DHST+CANDELS respectively. Only the redshift bins in which the satellites are complete are plotted. We demonstrate that the inferred merger rates are consistent within the uncertainties as long as the appropriate observability timescale (τ_{obs}) is applied for the R_{proj} range (Lotz et al., 2010). We note that the merger rates appear to be systematically higher for the widest R_{proj} bin (10-100 kpc h^{-1}) compared to the others, which we interpret as being due to the wide pairs at $\sim 50-100$ kpc h^{-1} probing the large-scale environment in which pairs at similar redshifts may not necessarily merge within the τ_{obs} predicted in binary merger simulations.

for easy comparison to literature. As the merger rate uncertainties are considerably larger than the measured merger fractions due to the 50% uncertainty in τ_{obs}, the redshift dependence is weaker and we therefore deem a quadratic fit which has one more degree of freedom than the power law unnecessary. We show the integrated number of major and minor mergers in Table 3.5 for the two catalogs and selection methods.

We find that at $z > 2$ the observed merger rates using the stellar mass ratio selection are lower than predicted from the semi-analytical models (SAMs) of Hopkins et al. (2010c,d) as shown in Figure 3.6, but are consistent with the gas-poor merger rate ($f_{gas} < 20\%$, where the gas fraction f_{gas} is defined as the ratio of the total gas mass to the total baryon mass of the merging galaxies). In general the SAMs predict that the galaxy merger rates increase monotonically with redshift. Our measurements using the H-band flux ratio selection show an increasing trend similar to the gas-rich merger rate of Hopkins et al. (2010d) ($f_{gas} \geqslant 20\%$), even though the H-band flux is not a direct tracer of cold gas mass or star formation rate. This lends support to our claim in Section 3.3.1.1 that using the stellar mass ratio as a probe for the baryon mass ratio may be subject to a bias against gas-rich mergers at $z > 2$, an epoch at which cold gas fraction is

non-negligible especially for intermediate mass galaxies (Stewart et al., 2009a; Hopkins et al., 2010c).

We also compare the merger rates inferred from the merger fractions of various R_{proj} bins in Figure 3.7. We only show results for the stellar mass ratio selection, but the following conclusions also hold for the H-band flux ratio selection. We find that the merger rates are consistent for different R_{proj} bins once the suitable observability timescales from Lotz et al. (2010) are applied. On average, the merger rates derived from mergers with R_{proj} = 10-100 kpc h^{-1}[1] are up to 40% higher than for smaller R_{proj} bins, although still consistent within the large uncertainties due to the 50% uncertainty in the merger observability timescale. This implies that there are more widely separated mergers ($R_{proj} = 50 - 100$ kpc h^{-1}) than expected from the timescales of binary merger simulations. Possible explanations could be: (1) the large scale environment of galaxies are probed at separations of > 50 kpc h^{-1}, therefore we may include galaxies in the same over-densities that are not bound to merge; (2) the merging observability timescales for wide pairs may be systematically longer than the assumed tilted polar orbit for close pairs, e.g. relative velocities of merging pairs are higher than assumed in the binary simulations (typically < 500km s^{-1}) which may be true in over-densities, or if the merger orbit is more like a circular orbit the merging timescale can be up to $> 40\%$ longer (Lotz et al., 2010). We note that the discrepancy is larger at lower redshift, hinting that the effect could be related to large-scale structure formation. Cosmological simulations may provide estimates of these effects. Although we do not use the timescale of Kitzbichler & White (2008) for galaxy merger fraction measurements for the reasons explained in Section 3.3.3.1, for comparison we note that using it leads to lower merger rates than those derived using the shorter timescales of Lotz et al. (2010) as expected from the inverse scaling between timescale and rate.

3.3.3.3 Merger-driven stellar mass accretion rate

We compute the merger-driven stellar mass accretion rate as $\dot{M}_\star$ [$M_\odot$ / Gyr / galaxy] = $\bar{M}_1 \mathbb{R}/\bar{\mu}$, where $\bar{M}_1$ is the median stellar mass of the massive galaxies, $\mathbb{R}$ is the major (minor) merger rate, and $\bar{\mu}$ is the median stellar mass ratio of the major (minor) mergers. All these quantities are redshift dependent so we are able to calculate the merger-driven stellar mass growth as a function of time.

There is controversy regarding whether merging triggers significant star formation episodes compared to isolated galaxies (e.g. Patton et al., 2011; Xu et al., 2012b; Yuan et al., 2012; Lanz et al., 2013; Patton et al., 2013; Lackner et al., 2014; Puech et al., 2014). Gallazzi et al. (2014) study the evolution of the age-, mass-metallicity relation of mas-

[1] An upper limit of $R_{proj} < 100$ kpc h^{-1} is still small compared to the typical photo-z uncertainty. The typical photo-z error at $z = 0 - 4$ is $\delta z/(1+z) = 0.026$ (Muzzin et al., 2013), corresponding to 84 Mpc/h at $z = 1.5$. Therefore we do not expect the photo-z uncertainty to constrain widely separated pairs.

Table 3.4. Merger number densities and rates

	Major merger		Minor merger	
Redshift range	$n_{merge} = \Gamma \times \tau_{obs}$[Gyr] [$\times 10^{-3}$ Mpc$^{-3}h^3$]	$\Delta N_{merger} \times \tau_{obs}$	$n_{merge} = \Gamma \times \tau_{obs}$[Gyr] [$\times 10^{-3}$ Mpc$^{-3}h^3$]	$\Delta N_{merger} \times \tau_{obs}$
		UltraVISTA		
$0.1 < z \leq 0.4$	0.111±0.026	0.109±0.025	0.14±0.029	0.138±0.028
$0.4 < z \leq 0.65$	0.076±0.013	0.09±0.015	0.098±0.015	0.117±0.017
$0.65 < z \leq 0.9$	0.182±0.015	0.125±0.01	0.169±0.014	0.116±0.01
$0.9 < z \leq 1.2$	0.131±0.01	0.123±0.009	0.1±0.008	0.094±0.008
$1.2 < z \leq 1.5$	0.084±0.007	0.083±0.007	0.08±0.007	0.079±0.007
$1.5 < z \leq 1.8$	0.072±0.006	0.072±0.006	0.044±0.005	0.044±0.005
$1.8 < z \leq 2.1$	0.051±0.005	0.045±0.005	0.021±0.004	0.019±0.003
$2.1 < z \leq 2.4$	0.02±0.003	0.028±0.005	0.008±0.002	0.01±0.003
$2.4 < z \leq 2.7$	0.014±0.003	0.016±0.003	0.009±0.002	0.011±0.003
$2.7 < z \leq 3.0$	0.01±0.003	0.015±0.004	0.005±0.002	0.007±0.003
		3DHST+CANDELS		
$0.1 < z \leq 1.0$	0.115±0.021	0.5±0.09	0.099±0.019	0.43±0.084
$1.0 < z \leq 1.5$	0.066±0.014	0.096±0.02	0.086±0.016	0.124±0.023
$1.5 < z \leq 2.0$	0.08±0.014	0.073±0.013	0.078±0.014	0.071±0.012
$2.0 < z \leq 2.5$	0.033±0.009	0.031±0.008	0.025±0.008	0.024±0.008
$2.5 < z \leq 3.0$	0.024±0.008	0.023±0.008	0.014±0.006	0.013±0.006

Note. — This table lists the number density of the stellar mass ratio selected major and minor mergers using the UltraVISTA and 3DHST+CANDELS catalogs. The number density n_{merger} is related to Γ (number of mergers per unit volume per unit time) and the merger observability timescale τ_{obs} by $\Gamma(z) = n_{merger}(z)/\tau_{obs}$ as explained in Equation (3.3.1). Therefore n_{merger} can be interpreted as the merger rate Γ normalized to τ_{obs} of 1 Gyr. The average number of merger experienced in the redshift bin is ΔN_{merger}, calculated by integrating the volume-averaged merger rate $\mathbb{R}$ over the elapsed time ($\Delta N_{merger} = \int_{t_1}^{t_2} \mathbb{R}(z)dt = \int_{t_1}^{t_2} f_{merge}dt/\tau_{obs}$ if constant τ_{obs} is assumed) as described in Equation (3.3.3).

sive galaxies since $z \sim 0.7$ to $z \sim 0$, and report that neither new star formation nor chemical enrichment is needed for the evolution of massive quiescent galaxies. Additionally, we do not have measurements of the gas fraction of our merger sample. Therefore we note that our analysis only accounts for the accretion of existing stars and ignores stars formed during mergers, setting the lower limit on the merger contribution to the stellar mass growth.

We show the stellar mass accretion rate as a function of redshift in Figure 3.8. For the average massive galaxy of $\log(M_\star/M_\odot) \geqslant 10.8$, we find that major (minor) merging

Table 3.5. The average number of mergers experienced by a massive galaxy during $z = 0.1 - 2.5$

R_{proj}	Stellar mass ratio selected		H-band flux ratio selected	
	Major merger	Minor merger	Major merger	Minor merger
		UltraVISTA		
10-30 kpc h^{-1}	0.9 ± 0.2	0.7 ± 0.1	1.4 ± 0.3	0.9 ± 0.2
10-100 kpc h^{-1}	1.9 ± 0.1	1.2 ± 0.1	3.2 ± 0.1	1.8 ± 0.1
		3DHST+CANDELS		
10-30 kpc h^{-1}	1.0 ± 0.4	0.7 ± 0.2	1.5 ± 0.6	1.0 ± 0.3
10-100 kpc h^{-1}	1.8 ± 0.1	1.1 ± 0.1	2.8 ± 0.2	2.2 ± 0.2

Note. — The average number of mergers (N_{merger}) experienced by a massive galaxy. We calculate N_{merger} by measuring the galaxy merger fraction using galaxy mergers within the stated R_{proj} bins, converting the merger fraction into merger rate using a observability timescale for that R_{proj} bin (Lotz et al., 2010) and integrating over cosmic time. The N_{merger} derived from all the R_{proj} bins are consistent within the uncertainties except for the widest bin of $R_{proj} = 10 - 100$ kpc h^{-1}, therefore we show the N_{merger} for 10-30 kpc h^{-1} as default and omit the other two bins (5-20 kpc h^{-1} and 10-50 kpc h^{-1}) that give consistent results.

leads to an average stellar mass growth of and $4.0(0.9) \times 10^{10} M_{\odot}$ during $z = 0.1 - 2.5$. This amounts to a total of $4.9 \times 10^{10} M_{\odot}$ being accreted via 1:1 - 10:1 mergers, implying that the average $10^{11} M_{\odot}$ galaxies increase their stellar masses by at least $\sim 50\%$ through accreting existing stars from satellite galaxies from $z = 2.5$ to 0.1.

Our results are in agreement with similar observations for bright central galaxies in galaxy clusters (Lidman et al., 2013) and field galaxies (Bundy et al., 2004; Ferreras et al., 2013) up to $z \sim 1$, showing that major merging plays a significant role in the mass assembly of massive galaxies (and therefore its number density evolution) independent of the environment. Our stellar mass accretion rates are also consistent with simulation predictions (Stewart et al., 2009b; Cattaneo et al., 2011; Lackner et al., 2012; Laporte et al., 2013) with the exception of Oser et al. (2010). Oser et al. (2010) follow the history of simulated massive galaxies and find that by $z = 0$, 80% of the stars in massive galaxies are formed at $z = 3 - 4$ ex-situ of the original halo at $z = 7$, and are accreted at $z < 2$ with an average rate of $\sim 17 M_{\odot}$/yr. Their average mass accretion rate stays relatively flat at $z > 2$ and decreases at lower redshift, which is qualitatively similar to our observed trends but on average $\geqslant 2\times$ higher, as seen in Fig. 3.8. As we discussed in Section 3.3.2.2, this is explained by the higher minor merger rates in their

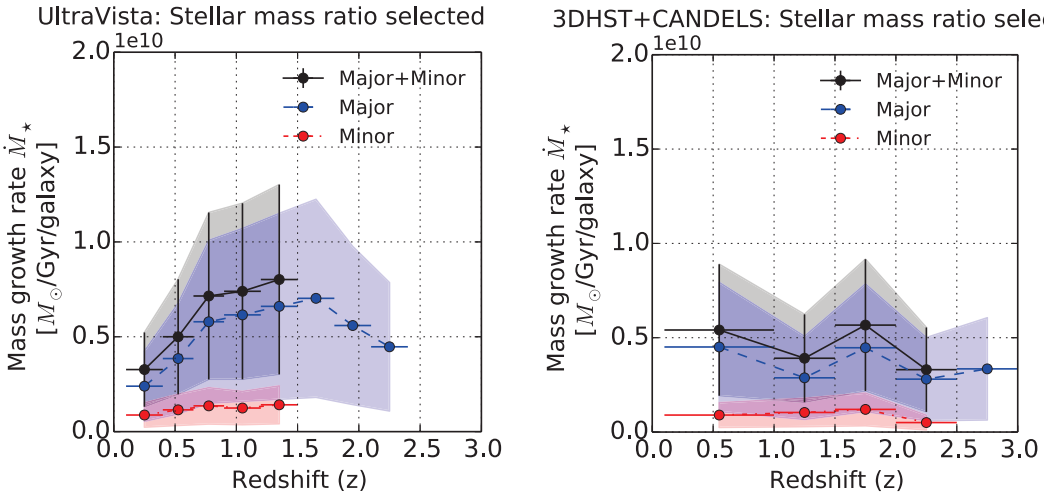

Figure 3.8: The stellar mass growth rate ($\dot{M}_\star$) due to the accretion of existing stars via merging is computed as $\dot{M}_\star$ [$M_\odot$ / Gyr / galaxy] = $\bar{M}_1 \mathbb{R}/\bar{\mu}$, where $\bar{M}_1$ is the median stellar mass of the massive galaxies, $\mathbb{R}$ is the major (minor) merger rate and $\bar{\mu}$ is the median stellar mass ratio of the major (minor) mergers. The results from both the UltraVISTA (left) and 3DHST+CANDELS (right) surveys are shown. The blue, red, and black circles denote the stellar mass accretion rate via major, minor merging, and the two combined. The shaded regions indicate the uncertainties propagated from the merger rates and stellar masses. Only the redshift bins which are complete are plotted. We observe that major merging is the primary mechanism for driving the stellar mass accretion of massive galaxies. Following the trend of the merger fractions, the stellar mass growth rate rises from $z \sim 0.1$ to $z \sim 0.8$ and remains relatively flat thereafter, as seen on the results from UltraVISTA (left). There are insufficient galaxies to probe any redshift trend below $z \sim 1$ in 3DHST+CANDELS.

simulations compared to the observations of this works and others. We emphasize that the stellar mass accretion rate presented here does not include new stars formed due to merger-triggered star formation episodes, and therefore represents a lower limit of the true merger-driven stellar mass growth rate (see also the discussion in Section 3.3.1.1).

3.3.4 Maximum merger-driven size and velocity dispersion evolution

Dry merging provides a channel to increase the sizes of compact (~ 1 kpc) massive quiescent galaxies (QGs) at $z > 2$ by a few factors to $z \sim 0$ (e.g. Bezanson et al., 2009; Naab et al., 2009; Oser et al., 2012; Hilz et al., 2012, 2013), as discussed in Section 3.3.2. We use our measured stellar mass accretion rate to infer an upper limit on the size evolution due to "dry" dissipationless merging. Since QGs are expected to remain quiescent for the build-up of the red sequence, and the dissipation from gas in merging galaxies can reduce the efficiency of puffing up sizes of galaxies, for this exercise we make the

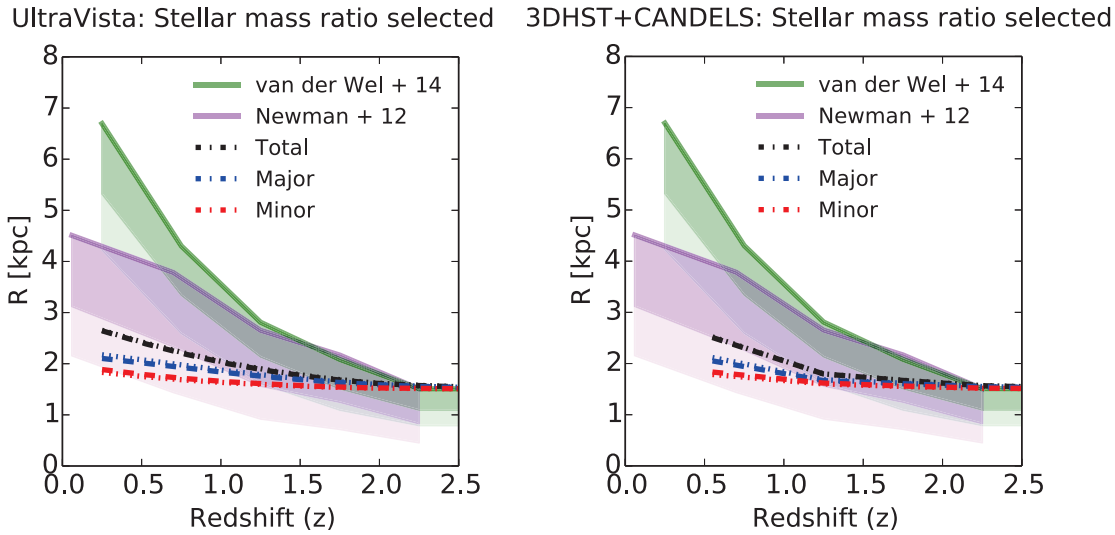

Figure 3.9: The size evolution inferred from the merger-driven stellar mass accretion rate. The results from both the UltraVISTA (left) and 3DHST+CANDELS (right) surveys are shown. The blue and red lines show the predicted size evolution from major and minor mergers respectively, and the black lines are the combined contribution from major and minor mergers. We have used two size evolution models: the dotted lines represent the virial argument (Naab et al., 2009) and the dashed lines represent the model of Hilz et al. 2013. The size evolutions predicted from both models nearly overlap each other, illustrating that the virial theorem is an adequate approximation. The models are normalized to a $M_\star = 10^{11} M_\odot$ galaxy of 1.5 kpc at $z = 2.5$. We compare the predicted merger-driven size evolution with observations: the green and orchid lines denote the observed size evolution of early-type / quiescent massive galaxies measured by van der Wel et al. 2014 and Newman et al. 2012 respectively. The lower 1σ and 2σ scatters of the relations are shown by the darker/lighter shades. As the merger fractions are consistent between the UltraVISTA and the 3DHST+CANDELS surveys, the predicted size evolution are very similar as expected. We claim that major and minor merging can increase the sizes of massive QGs by a factor of ~ 2 at most from $z \sim 2.5$ to 0. While this amount of merging is insufficient to explain the observed evolution of the average sizes of massive QGs, it is enough to bring the sizes to 1σ below the mean sizes if the size scales with redshift as $R \propto (1+z)^{-1}$ (Newman et al. 2012, see also Toft et al. 2009; Williams et al. 2010; Toft et al. 2012; Krogager et al. 2013).

simplistic assumption that all observed mergers are dissipationless. The aim of the test is to investigate to what extend the observed frequency of galaxy merging can explain the size evolution of QGs. We find that the merger fractions of massive galaxies and the quiescent subset are consistent within their uncertainties, therefore we simply use the merger fractions of the overall massive galaxy population in the following analysis.

The virial theorem and more sophisticated merger simulations have been used to predict the size evolution due to dry merging. The size evolution can be parameterized

as $R \propto M^{\alpha}$, where $\alpha \sim 1$ for major merging and $\alpha \sim 2$ for minor merging predicted using the virial theorem (Bezanson et al., 2009; Naab et al., 2009), or alternatively $\alpha \sim 0.91$ for major merging and $\alpha \sim 2.3$ for minor merging according to the simulations of Hilz et al. (2012, 2013). The high value of α for minor merging in Hilz et al. (2013) implies that it is very efficient in increasing the sizes of galaxies, and likely represents an upper limit due to the high dark matter content and extended stellar haloes of the satellites assumed in their simulation. For each redshift bin, we multiply the average stellar mass accretion rate (see Section 3.3.3.3) with the time elapsed in the redshift bin to get the stellar mass accreted, and scale the predicted size growth to the stellar mass accretion using the α values as discussed above. The maximum merger-driven size growth using both catalogs are plotted in Figure 3.9. We observe that the total amount of merging can only increase the size of massive QGs by a factor of two, from 1.5 kpc at $z = 2.5$ to ~ 3 kpc at $z \sim 0$. This result is insensitive to the size growth model used, meaning that the virial theorem provides a good approximation of the size evolution due to dissipationless merging.

The observed size evolution of massive QGs (or early-type galaxies) has been presented in various works. On Figure 3.9 we compare our predicted merger-driven size evolution to two recent measurements using CANDELS. Newman et al. (2012) report an average size growth of ~ 3.5 from $z = 2.5$ to 0, with a redshift dependence of $R \propto (1+z)^{-1.0}$, consistent with previous works including Toft et al. (2009); Williams et al. (2010); Toft et al. (2012) and Krogager et al. (2013). On the other hand, van der Wel et al. (2014) report a consistent but slightly stronger size growth of ~ 5 times in the same redshift range, with a redshift dependence of $R \propto (1+z)^{-1.3}$, similar to the finding of Cassata et al. (2013). Both works report the scatter of the stellar-mass size relation to be consistent with being constant. The difference of the observed size evolution may be due to the stellar mass threshold, as well as the size measurement technique. As the primary focus of this paper is not the observed size evolution, we can only conclude that merging increases the sizes of a $10^{11} M_{\odot}$ QG by a factor of two at most from $z \sim 2.5$ to 0. While this is insufficient to explain the observed average size growth of a factor of 3-5, it is enough to bring the average sizes of massive QGs to 1σ below the local mean stellar mass-size relation if the redshift dependence is on the milder end of the observations ($R \propto (1+z)^{-1.0}$) like in Newman et al. (2012). If the sizes follow a normal distribution, the massive QGs already formed and quenched since $z \sim 2.5$ evolve through merging to form the smallest 16% (2%) of local massive QGs since they lie at 1σ (2σ) below the mean. If the sizes follow a skewed distribution instead, as shown by Newman et al. (2012), the fraction can be even higher (e.g. up to the smallest 12.5% for 2σ below mean following Chebyshev's inequality). This may be a more relevant representation if these compact QGs end up to lie below the local mass-size relation, while the majority of later quenched QGs occupy the upper part of the relation. Recent measurements of

compact massive QGs reveal that their number densities peak at $z \sim 1.8$, and decrease at lower redshifts (van der Wel et al., 2014; van Dokkum et al., 2014), therefore they must undergo structural changes. Incidentally this is the same redshift range in which our merger rate peaks (major: $z \sim 0.7 - 1.7$, minor: $z \sim 0.7 - 1.5$, see Fig. 3.6). We will further the discussion on the observed size evolution in Section 3.4.1.

Even though there may be a significant number of minor mergers rejected by the stellar mass ratio criterion (flux ratio between 1:1 and 10:1, but stellar mass ratio more extreme than 10:1), these mergers are more likely to have non-negligible gas mass and more dissipation so it does not help to solve the problem of the observed size evolution. The gas content of merging galaxies may explain the scatter of the redshift-size evolution (Khochfar & Silk, 2006). However without gas measurements we are not able to test this hypothesis at this point.

The virial theorem predicts that equal-mass mergers do not change the stellar velocity dispersion $\sigma_\star$, and minor mergers reduces the $\sigma_\star$ by $\sigma^2_{\star,1+2}/\sigma^2_{\star,1} \approx M_1/M_{1+2}$ if the satellite has a $\sigma_\star$ much lower than the massive galaxy it is merging with (Bezanson et al., 2009; Naab et al., 2009). Using the stellar mass accretion rate we estimate that 4:1-10:1 minor mergers can only reduce the $\sigma_\star$ of massive galaxies by 6% from $z = 2.5$ to 0.1. If we relax the assumption and allow 1:1 - 4:1 mergers to be equally efficient in reducing $\sigma_\star$, the total stellar mass accreted implies that the $\sigma_\star$ decreases by maximum 25% from $z = 2.5$ to 0.1. From this we conclude that merging is insufficient to reduce the high $\sigma_\star$ (~ 300 km s^{-1}) observed in $z \sim 2$ QGs (Toft et al., 2012) by $\sim 60\%$ to match the average of the local population. This is consistent with claims that the addition of lower $\sigma_\star$ galaxies to the quiescent population at later times contribute to the decreasing average $\sigma_\star$ of the overall massive QG population (Bezanson et al., 2012, 2013). We note that if a significant amount of dark matter is accreted by these massive QGs, the total mass increases and therefore the velocity dispersion and the sizes may change without any observable stellar mass growth.

3.3.5 The major merger contribution to the formation of "new" massive galaxies

To understand what the merger rates from Section 3.3.3.2 imply for the overall galaxy evolution, in this section we aim to quantify the contribution of merging to the observed increase in the number density (n_{mas}) of massive galaxies in the redshift range $z = 0.1 - 3$. As shown in Section 3.3.3.3, most of the stellar mass accreted is through major merging, so in this section we only consider major merging for which our samples are complete to higher redshifts. Merging can affect the number counts of massive galaxies in two counteracting ways. On one hand, merging among lower mass galaxies can increase the number of massive galaxies above a stellar mass threshold. On the other hand, merging among massive galaxies already above the mass threshold will lead to

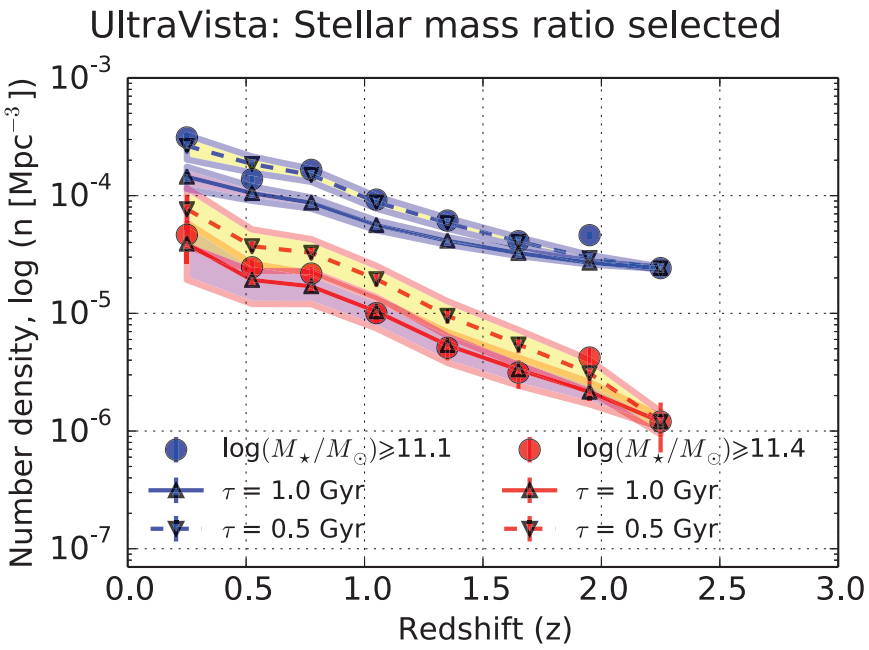

Figure 3.10: The number density evolution of the most massive galaxies (n_{mas}) above two stellar mass thresholds. The blue (red) filled circles represent the observed n_{mas} of massive galaxies of $\log(M_\star/M_\odot) \geqslant 11.1$ (11.4), and the error bars represent the Poisson error of the number counts. The triangles represent the major-merger driven n_{mas} growth using two merger observability timescales (τ_{obs} =0.5 Gyr: downward triangles, dashed lines and yellow shades; 1.0 Gyr: upward triangles, solid lines, purple shades). The colored shades show the uncertainty on n_{mas} propagated from the Poisson errors of the number of mergers. The predicted major-merger driven n_{mas} growth accounts for the formation of "new" massive galaxies above the threshold due to major merging, as well as the reduction in numbers of massive galaxies that merge with each other (a minor effect as observed). The predicted growth is normalized to the observed n_{mas} of massive galaxies $z \sim 2.25$ to which we are complete for major mergers. We only perform this exercise on the UltraVISTA catalog, because the 3DHST+CANDELS contain too few galaxies above these stellar mass thresholds for meaningful n_{mas} constraints. We find that the slope of the observed n_{mas} evolution of the most massive galaxies follows the predicted slope due to major merging, if the $\tau_{obs} \simeq 0.6 - 0.7$ Gyr (Lotz et al., 2010) for major merging which is roughly the average of the two timescales shown. To keep the slope consistent with the observed number densities, a maximum of 15% stellar mass can be added in addition to major merging, implying $\leqslant 6\%$ for mechanisms other than major and minor merging.

a decreased number count. We denote ΔN_+ as the number of mergers with individual stellar masses lower than a given threshold, but with the sum of their stellar masses above the threshold (Robaina et al., 2009; Man et al., 2012), and ΔN_- as the number of mergers with the individual stellar masses of both galaxies above the threshold. The net change of n_{mas} due to major merging is $\Delta n_{mas}(z) = (\Delta N_+(z) - \Delta N_-(z))/V_{comoving}(z) \times$

$\Delta t(z)/\tau_{obs}$, where $V_{comoving}(z)$ and $\Delta t(z)$ are the comoving volume and the elapsed time of the redshift range, and τ_{obs} is the merger observability timescale given the projected separation (R_{proj}) range. The τ_{obs} for major mergers with R_{proj} = 10-30kpc h^{-1} is about 0.6-0.7 Gyr (Lotz et al., 2010) with an error of $\sim$ 0.4 Gyr. In this exercise we show the results of two values of τ_{obs} (0.5 and 1.0 Gyr). Since we assume that no new stars are formed during mergers for the reasons discussed in Section 3.3.3.3, the presented quantities mark the minimum merger contribution to the formation of new massive galaxies.

We present the results in Figure 3.10. We find that major merging alone can explain the n_{mas} evolution of galaxies more massive than $10^{11.1}M_{\odot}$ if τ_{obs} lies between 0.5 - 1 Gyr. If τ_{obs} was systematically much longer than 1 Gyr, then additional mechanisms may be required to explain the n_{mas} evolution of these very massive galaxies. We note that 3DHST+CANDELS is inadequate for tracing the n_{mas} growth of the most massive galaxies. The volume probed is too small leading to large cosmic variance on the observed number density and therefore is not shown.

Taking our results further, we use the observed n_{mas} evolution of the most massive galaxies to constrain the upper limit of the stellar masses that can be added in addition to major merging. We increase the stellar masses of all the galaxies by an arbitrary factor, and count the number of galaxies $\Delta N^{'}_{+}$ that cross the given mass thresholds. Its contribution to the n_{mas} evolution is $\Delta N^{'}_{+}(z)/V_{comoving}(z)$. We find that the observed n_{mas} evolution is marginally consistent with a maximum 15% of stellar mass growth of the overall massive galaxy population in addition to major merging since $z \sim 2.5$. Any non-major merging stellar mass growth beyond 15% would overproduce the number of the most massive galaxies. As shown in Section 3.3.3.3, minor merging accounts for $\sim 9\%$ of the stellar mass accreted. Therefore we conclude that there remains little room ($\leqslant 6\%$) for the most massive galaxies to increase their stellar masses by mechanisms other than major and minor merging, such as star formation or very minor mergers ($\mu >$10:1).

3.4 DISCUSSIONS

3.4.1 AN EMERGING EVOLUTIONARY SCENARIO FOR MASSIVE QUIESCENT GALAXIES (QGS)

There are comparative studies of the possible mechanisms that can explain the size evolution (Hopkins et al., 2010a; Trujillo et al., 2011; Cameron & Pettitt, 2012). Merging, in particular dry minor merging, appears to be a viable means to explain the observed size and velocity dispersion evolution. However, even when we assume that all mergers were dry (dissipationless), the size evolution inferred from our merger fraction can only account for a factor of two of size increase from z $\sim$2.5 to 0.1. This is marginally

consistent with being 1σ below the mean stellar-mass size relation of the measurement of Newman et al. (2012), but $> 2\sigma$ compared to that of van der Wel et al. (2014). This necessitates additional mechanisms to explain the observed size increase for the bulk of the population.

The apparent strong size evolution may be in part due to observational effects. Our observations indicate that massive galaxies tend to merge with galaxies with lower stellar mass-to-light ratios (see Figure 3.2 and Section 3.3.1.1). If the younger, bluer stars of the companion are added to the outskirts of massive galaxies consisting of older stellar populations (van Dokkum et al., 2010; Hilz et al., 2012, 2013), then the half-light radius (r_e) measured in rest-frame optical bands increases. This scenario is supported by the observed negative color gradients (van Dokkum et al., 2010; Guo et al., 2011; Szomoru et al., 2011; Gargiulo et al., 2012; Szomoru et al., 2013), and is consistent with the observation of van der Wel et al. (2014) that the r_e of massive galaxies are smaller when measured at longer wavelengths. Szomoru et al. (2013) show that the half-mass radii of massive QGs are on average $\sim 25\%$ smaller than the half-light radii measured from the rest-frame g-band. Therefore the observed size evolution is perhaps in part due to the radial dependence of the $M_\star/L$. Since the number- and mass-weighted average stellar mass ratio is $\sim$ 4:1 for the mergers in this work, the satellites may strip off their stars at the outskirts like the 5:1 intermediate mass ratio merger simulated by Hilz et al. (2013), lending support to merging as a viable explanation for the observed size evolution and color gradients.

It is important to distinguish between the growth of individual galaxies and the evolution of the overall population. The number density of the massive QGs evolves with redshift, for instance massive ($10^{11} M_\odot$) galaxies are 30 times more abundant at $z \sim 0.95$ than $z \sim 2.75$ (e.g. Marchesini et al. 2009; Ilbert et al. 2013 and references therein, also see Section 3.3.5). Therefore if larger, later quenched galaxies are continuously added to the QG population, it may be sufficient to increase the average sizes of QGs (more details about the so-called "progenitor bias" in van der Wel et al. 2009a; Carollo et al. 2013; Krogager et al. 2013). This assumes that the sizes of QGs are correlated with their age or time since being quenched, a trend which is observed in some works (Shankar & Bernardi, 2009; van der Wel et al., 2009a; Bernardi et al., 2010; Poggianti et al., 2013) but not in others (Trujillo et al., 2011; Whitaker et al., 2012). Another implication is that the scatter of the size evolution is expected to increase if the progenitor bias is the sole explanation for the observed size evolution, which contradicts the constant scatter observed (Trujillo et al., 2011; Krogager et al., 2013; van der Wel et al., 2014). Additionally, the progenitor bias alone does not explain the disappearance of compact QGs observed at $z > 2$ (Belli et al., 2014a; van der Wel et al., 2014; van Dokkum et al., 2014). The number density of compact QGs peaks at $z \sim 1.6 - 2.2$ and decreases towards lower and higher redshifts. Our merger fractions (stellar mass ratio selected) peak at $z \sim 1 - 1.5$,

and one may speculate on a causal relation between the two observations.

A fixed number density selection may provide a more direct comparison between massive QGs at $z \sim 2$ and their descendants at lower redshifts (e.g. van Dokkum et al., 2010; Behroozi et al., 2013; Leja et al., 2013). If the descendants of compact massive QGs at $z \gtrsim 2$ are the most compact QGs in clusters in the local Universe, the sizes of individual QGs will only need to increase by a factor of ~ 1.6 (Poggianti et al., 2013), which is in good agreement with the size evolution inferred from our merger rates.

Apart from the observational effects and the progenitor bias discussed above, alternative means to increase the sizes of individual QGs have been proposed. Some examples include AGN and/or supernova feedback (Fan et al., 2008, 2010), adiabatic cooling via the mass loss of old stars (Damjanov et al., 2009; van Dokkum et al., 2014), and halo size evolution (Posti et al., 2014). It is beyond the scope of this work to draw conclusions on the relative contributions of the possible options in explaining the size evolution. We emphasize that our results provide a strong constraint: whichever mechanisms are responsible for the observed size evolution, there is little room focolorr further stellar mass to be created or added (6% at most for $z = 0 - 2.5$) for the most massive galaxies ($M_\star \geqslant 10^{11.1} M_\odot$) in order not to over-produce the observed numbers at different redshifts.

3.4.2 Merger contribution to cosmic star formation

The open question of whether merging is a major contributor to the cosmic star formation history (SFH) has been tackled in different ways: Do merging galaxies have higher star formation rates compared to isolated ones (Ellison et al., 2008; Patton et al., 2011; Scudder et al., 2012; Xu et al., 2012b; Yuan et al., 2012; Patton et al., 2013; Lackner et al., 2014)? At each epoch, are star-forming galaxies primarily mergers or isolated disks (Genzel et al., 2008; Shapiro et al., 2008; Förster Schreiber et al., 2009; Law et al., 2009; Kaviraj et al., 2013a,b; Kaviraj, 2014a,b)? These different perspectives can lead to seemingly contradictory conclusions.

Despite the apparent offset of visually identified mergers from the SFR-$M_\star$ relation (dubbed "main-sequence', Hung et al. 2013), merging galaxies only show disturbed morphologies for a limited time (~ 0.3 Gyr, e.g. Lotz et al. 2010). If the duty cycle of mergers is interpreted as the cause for the scatter of the SFR-$M_\star$ relation, major mergers account for a majority of the total SF at $z \sim 0.6$ (Puech et al., 2014). Patton et al. (2013) have shown that mergers can enhance SFR to $R_{proj} \sim 150$ kpc, and such widely separated merging galaxies are likely not identified in morphological selected samples which probe later-stage mergers. On the other hand, the existence of isolated star-forming disks has been used as evidence against mergers being a contributor of cosmic SF budget based on the assumption that mergers destroy disks (e.g. Toomre & Toomre, 1972). While mergers *can* destroy disks and remain a popular explanation for bulge for-

mation (Hopkins et al., 2010c), various works have shown that disks can reform after gas-rich mergers (Hopkins et al., 2009a; Stewart et al., 2009b; Puech et al., 2012).

Even though galaxy merging may not increase the total amount of stars formed from the available cold gas reservoir, it can trigger starburst episodes by temporarily enhancing the star formation efficiency, leading to faster cold gas depletion (Cox et al., 2008; Torrey et al., 2012). Detailed studies of the SFH of individual galaxies can provide an answer to whether most stars in galaxies are formed during merging or isolated phases (continuous vs bursty SFH). In Section 3.3.1.1 we have shown that using the H-band flux ratio to select mergers leads to an increasing merger fraction evolution, as opposed to the flat or diminishing trend seen using stellar mass ratio selected pairs. The former merger fraction share a similar redshift evolution as the cosmic star formation rate density (e.g. Madau & Dickinson 2014 and references therein) albeit with considerable uncertainties: both rise from $z \sim 0$ to $z \sim 1$ and reach a plateau or increase mildly from $z \sim 1$ to $z \sim 2.5$. This may be a hint that at $z \gtrsim 1.5$, massive galaxies are primarily merging with low stellar mass ($M_1/M_2 > 10$:1) but gas-rich satellites. These mergers are classified as major or minor depending on whether the baryon mass or stellar mass ratio is used. When inferring the merger contribution to the cosmic star formation budget, we need to account for these "missing" mergers (Stewart et al., 2009a) that did not enter the stellar mass ratio selection. Future surveys of the molecular gas mass of high-z galaxies are needed to make progress on this issue.

3.4.3 FUTURE PROSPECTS

The merger fraction of massive galaxies is $< 30\%$, resulting in low number densities of mergers ($\sim 10^{-4.5} - 10^{-6}$ Mpc^{-3}) at $z > 2$. As we show in Section 3.3.1.2, cosmic variance is the dominant source of uncertainty in merger fraction measurement with CANDELS-sized surveys, due to the small survey area and low source number density. We note that the merger fractions measured from UltraVISTA and 3DHST+CANDELS yield very consistent results (see Figure 3.4), even at the redshifts where UltraVISTA is expected to be incomplete for low surface brightness satellites. This is due to the fact that most satellites have lower $M_\star/L$ ratios (see Section 3.3.1.1 and Figure 3.2). As long as the lower limit of R_{proj} is set so that no close pairs are missed due to blending, and the relevant observability timescales are applied for the R_{proj} range (Lotz et al., 2010), deep ground-based NIR surveys like UltraVISTA and UDS provide as accurate results as *HST* surveys. Ground-based surveys have the additional advantage of larger sample sizes, so that the evolution can be probed in finer redshift bins with small Poisson uncertainties. Put another way, large area surveys are crucial to mitigate cosmic variance and Poisson uncertainties in galaxy merger fraction measurements. A limitation of the pair selection is that a minimum R_{proj} must be imposed to match the resolution of the imaging data, for example 10 kpc h^{-1} in this work. If the scientific interest is

on the incidence of late stage mergers of $R_{proj} \leqslant 10$kpc h^{-1} among AGNs or ULIRGS (e.g. Kartaltepe et al., 2010; Treister et al., 2010; Silverman et al., 2011; Kartaltepe et al., 2012; Treister et al., 2012; Ellison et al., 2013), alternative merger identifications may be a more appropriate choice (e.g. Le Fèvre et al., 2000; Conselice et al., 2003; Lotz et al., 2008c; Bluck et al., 2012; Lackner et al., 2014).

Photometric redshifts (photo-z's) are essential in removing line-of-sight projected pairs from merger samples. The projected pair fraction is redshift dependent and can reach $N_{\rm projected}/N_{\rm mergers} \simeq 400\%$ at $z \geqslant 2$ (see Table 3.2). Statistical simulations can provide an estimate for the number of projected pairs, however photo-z's are crucial for selecting real mergers for spectroscopic follow-up. One may expect photometric samples of mergers to include more mergers due to the larger uncertainties of photo-z's than spec-z's, however the merger fractions presented in this work using photometrically selected mergers are in agreement or even lower than those using spectroscopic selected mergers (de Ravel et al., 2009, 2011; López-Sanjuan et al., 2011, 2012; Tasca et al., 2014). Aside from the variations of the parent sample as discussed in Lotz et al. (2011), this may be an indication that the selection effects associated with the spectroscopic merger samples outweigh the uncertainties of photo-z's in photometric merger samples, e.g. mass-incompleteness (due to flux-limited selection), slit/fiber placement incompleteness, limited sample sizes and so on. Therefore we argue that large-area ($\gtrsim 1$ deg^2) surveys with accurate photo-z's currently provide the most time-efficient datasets for measuring galaxy merger fractions.

On the theoretical front, the merging probability of galaxy pairs in close physical separations need to be quantified as a function of redshift and environment, as discussed in Section 3.3. It is also important to understand how galaxy fly-bys can impact the structure and dynamics of massive galaxies. These are subtle yet crucial quantities that fold into the interpretation of the inferred galaxy merger rates, which are paramount in determining whether galaxy merging is a significant driver of its evolution.

3.5 CONCLUSIONS

We present the largest sample of photometrically selected mergers at $z = 0.1 - 3$ from mass-complete catalogs, using complementary datasets of a large area ground-based survey (UltraVISTA) and a deep spaced-based survey (3DHST+CANDELS). We measure the galaxy major and minor merger fractions (f_{major} and f_{minor}). Applying the merging observability timescale (τ_{obs}) from Lotz et al. (2010), we infer the merger rates, as well as the evolution in stellar mass, size and number density for massive galaxies. We summarize our findings as follows:

1. The merger fraction shows a steep increase from $z \sim 0$ to 1, with f_{major} showing a stronger evolution than f_{minor}. Using the stellar mass ratio selection (Fig-

ure 3.1, left), f_{major} and f_{minor} show a plateau at $z \sim 1-1.8$ and diminishes beyond $z \sim 1.8$. If the observed H-band flux ratio selection is used instead (Figure 3.1, right), f_{major} and f_{minor} increase monotonically with redshift. The UltraVISTA and 3DHST+CANDELS show discrepant results at $z > 1.5$ due to the magnitude limit of the UltraVISTA DR1 survey.

2. Selecting mergers by the observed H-band flux ratio leads to an increasing merger fraction with redshift, while selecting mergers by stellar mass ratio shows a diminishing redshift dependence. This variation in merger selection technique is the cause of the discrepant merger fraction measurements at $z > 1.5$ in the literature (Bluck et al., 2009; Williams et al., 2011; Man et al., 2012; Newman et al., 2012). The discrepancy is a consequence of the $M_\star/L$ evolution of galaxies with redshift: at high redshifts and lower $M_\star$, galaxies have higher star formation rates and lower $M_\star/L$ ratios. The two selections produce consistent merger fractions at $z < 1.5$, but the fractions diverge at $z > 1.5$. The H-band flux ratio selection is biased towards bright, star-forming low-mass satellites at $z \gtrsim 1.5$, and the stellar mass ratio selection is biased against low-mass satellites which have significant cold gas mass. Cold gas measurements for massive galaxies and their satellites are required to refine the merger definition using the baryon mass ratio.
3. Our inferred merger rates using the stellar mass ratio selection is consistent with the gas-poor ($f_{gas} < 20\%$) merger rates of the simulations of Hopkins et al. (2010c). On the other hand, our inferred merger rates using the H-band flux ratio selection is consistent with their predicted gas-rich ($f_{gas} \geqslant 20\%$) ones.
4. We get consistent merger rates when mergers are selected from different R_{proj} bins (5-20, 10-30, 10-50, 10-100 kpc h^{-1}) when the relevant τ_{obs} from Lotz et al. (2010) are applied. However, we note that the widest R_{proj} are systematically higher than the other bins, with a more noticeable discrepancy at lower redshift. This is consistent with the pairs at 50-100 kpc h^{-1} probing large-scale structure formation.
5. The results imply that an average massive ($M_\star \geqslant 10^{10.8} M_\odot$) galaxy experiences $\sim 1.0 \pm 0.2$ major and $\sim 0.7 \pm 0.1$ minor mergers over the redshift range of $z = 0.1-2.5$, if mergers are selected by stellar mass ratio. There may be an additional ~ 0.5 major merger and ~ 0.3 minor merger if mergers are selected by the H-band flux ratio.
6. The mass-weighted average stellar mass ratio is $\sim$ 3:1-4:1, implying that the inferred stellar mass accretion rate is primarily driven by intermediate mass ratio mergers up to $z \sim 2.5$. This work extends the expectations from $z \lesssim 1$ to $z \sim 2.5$ that major merging is the dominant process for stellar mass accretion for massive galaxies.
7. Major and minor merging combined can at most increase the sizes by a factor of two from $z = 2.5$ to 0.1 for an average $M_\star \simeq 10^{11} M_\odot$ quiescent galaxy, if we assume that all mergers are dry. Additional mechanisms are thus required to explain the strong observed size evolution (factor of $\sim 3-5$).

8. The observed amount of major merging is sufficient to explain the evolution of the formation of new massive ($M_\star \geqslant 10^{11.1} M_\odot$) galaxies by number density arguments. These very massive galaxies can only increase their stellar masses by at most $\sim 6\%$ during $z = 0 - 2.5$ by processes in addition to major and minor merging, in order to match the observed number density evolution. This hints that star formation and very minor merging are unlikely mechanisms responsible for the observed size evolution.

Acknowledgements

We are grateful for the contributions of the UltraVISTA, COMSOS, CANDELS and 3DHST collaborations for making the catalogs available for public use. AM acknowledges Tomo Goto, Knud Jahnke, and Jennifer Lotz for helpful conversations at the early phase of this project. AM also thanks Bo Milvang-Jensen for clarification of the UltraVISTA data, and Anna Gallazzi for clarifying the stellar population models. The Dark Cosmology Centre is funded by the Danish National Research Foundation. We acknowledge the HPC facility at the University of Copenhagen for providing the computing resources used in this work. ST and AZ gratefully acknowledge support from the Lundbeck Foundation.

This work has made use of the UltraVISTA catalog, which is based on data products from observations made with ESO Telescopes at the La Silla Paranal Observatory under ESO program ID 179.A-2005 and on data products produced by TERAPIX and the Cambridge Astronomy Survey Unit on behalf of the UltraVISTA consortium.

This work is in part based on observations taken by the 3D-HST Treasury Program (GO 12177 and 12328) with the NASA/ESA HST, which is operated by the Association of Universities for Research in Astronomy, Inc., under NASA contract NAS5-26555. The 3DHST+CANDELS catalog is compiled using the datasets in these papers: Dickinson et al. (2003); Steidel et al. (2003); Capak et al. (2004); Giavalisco et al. (2004); Erben et al. (2005); Hildebrandt et al. (2006); Taniguchi et al. (2007); Barmby et al. (2008); Furusawa et al. (2008); Wuyts et al. (2008); Erben et al. (2009); Hildebrandt et al. (2009); Nonino et al. (2009); Cardamone et al. (2010); Retzlaff et al. (2010); Grogin et al. (2011); Kajisawa et al. (2011); Koekemoer et al. (2011); Whitaker et al. (2011); Bielby et al. (2012); Brammer et al. (2012); Hsieh et al. (2012); McCracken et al. (2012); Ashby et al. (2013); Almaini/Foucaud in prep and Dunlop et al. in prep.

APPENDIX

3.A COULD WE BE MISSING MERGERS?

In order to measure the merger fraction evolution robustly, it is essential to ensure completeness in the identification of merging satellites especially at high redshifts. We as-

sess the completeness of faint satellites in two aspects:

1. Stellar mass completeness: is UltraVISTA mass complete at high-z for the 10:1 satellites?

2. Surface brightness (SB): do we miss low SB faint satellites?

We present our analysis in the following subsections.

3.A.1 STELLAR MASS COMPLETENESS

We estimate the stellar mass ($M_\star$) completeness of the UltraVISTA catalog by comparing the K-band magnitudes and photo-z's of the detected galaxies with those of the deeper K-band selected FIREWORKS catalog ($K = 24.3$ at 5σ depth, Wuyts et al. 2008) in the Chandra Deep Field South. Assuming that the FIREWORKS catalog is 100% complete, we take the fractions of massive galaxies in FIREWORKS above different $M_\star$ in different redshift bins which are fainter than the UltraVISTA survey magnitude limit as the mass completeness limits. The results are shown in Figure 3.A.1. From this comparison we estimate that for the UltraVISTA sample, massive galaxies of $\log(M_\star/M_\odot) \geqslant 10.8$ are $> 75\%$ complete at $z \leqslant 3$. Major ($\mu \geqslant$ 4:1) satellites of $\log(M_\star/M_\odot) > 0.25\times \log(10.8) = 10.2$ are above 80% complete for $z \leqslant 2.7$. Minor satellites (4:1 $\leqslant \mu \leqslant$ 10:1) of $\log(M_\star/M_\odot) > 0.1\times \log(10.8) = 9.8$ are above 80% complete for $z \leqslant 2.4$. We list the $> 75\%$ limits in Table 3.A.1.

The CANDELS survey is sensitive to faint objects ($H = 26.9$ at 5σ depth, Grogin et al. 2011). For example quiescent galaxies with $M_\star = 10^{10} M_\odot$ are 50% complete at $z \sim 2.8$ (3.2) for wide and deep regions (Guo et al., 2013), therefore we expect the stellar mass completeness not to be an issue.

3.A.2 SURFACE BRIGHTNESS LIMITS: MODELING THE FAINTEST POSSIBLE SATELLITES

The detection of objects at faint magnitudes is sensitive to their surface brightness (SB) profiles and the source extraction thresholds. In order to test the redshift limit up to which we are complete to detecting the faintest possible satellites, we simulate the source detection by simulating galaxies with a range of Sersic profiles with magnitudes determined by a dust-free, maximally old stellar population at given $M_\star$ and redshifts. The effective half-light radii (r_e) assumed are the extrema calculated from the observed scaling relations and/or simulations, as described in detail below. To emulate the actual observations of UltraVISTA and CANDELS, the Sersic profiles are smoothed to the instrument PSF and added to images with blank patches of sky, and SExtractor is run with the object detection settings of the respective catalogs.

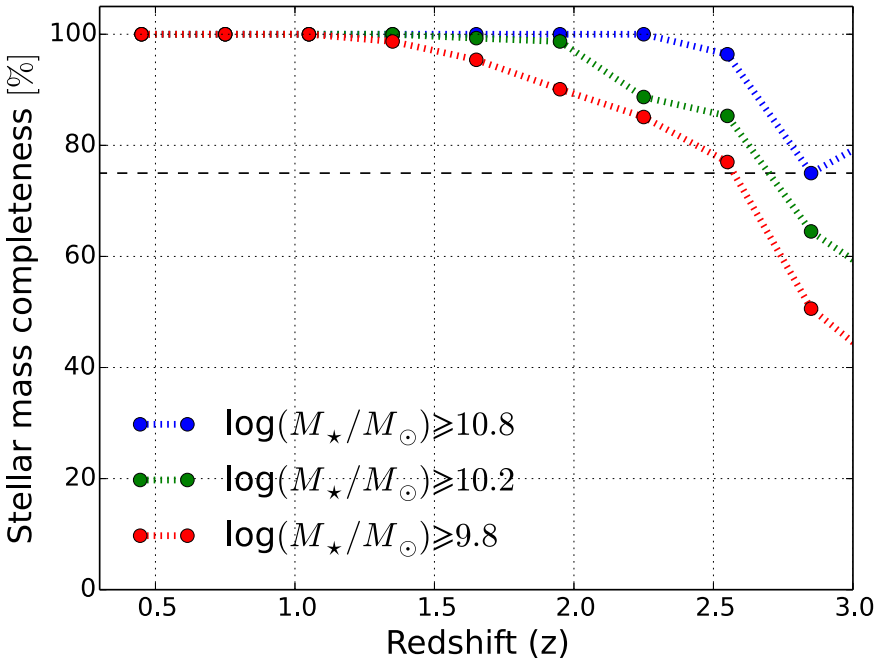

Figure 3.A.1: This plot shows the stellar mass completeness of the UltraVISTA catalog as a function of redshift. The stellar mass completeness here is computed by comparing the K-band magnitude distribution of UltraVISTA to the deeper FIREWORKS catalog. The stellar mass bins of the massive galaxies of $\log(M_\star/M_\odot) \geqslant 10.8$, as well as their 4:1 and 10:1 satellites are shown in different colors as indicated in the legend. The dashed line shows the 75% completeness limit.

Structural measurements of intermediate mass ($M_\star \sim 10^{9.8} M_\odot$) galaxies at $z \gtrsim 2$ are sparse due to their faintness. We list the possibilities here and select the extreme sizes for our simulations.

1. Observationally, the sizes of local elliptical or early-type galaxies scale with stellar mass as $R \propto M_\star^{0.5-0.56}$ for $M_\star > 10^{10.6} M_\odot$. The observed $z \sim 2$ stellar mass-size relation has a similar slope (Williams et al., 2010; Newman et al., 2012).

2. If intermediate mass galaxies have the same stellar density as massive galaxies, then the radius scales with stellar mass as $R \propto M_\star^{1/3}$.

3. Lastly, numerical simulations for merger-driven size evolution have shown that a Hernquist profile in projection can be described by a Sersic index of $n \sim 2.6$ (Hilz et al., 2012, 2013). These simulations use the same scale radius for the stellar halos of the host galaxy and the satellite which has only a tenth of the host stellar mass for the "diffuse" case.

Table 3.A.1. Completeness limits

	Mass completeness$> 75\%$	SB complete limit
	Massive galaxies / logM=10.8	
UltraVISTA	$z = 3.3$	$z > 3.5$
CANDELS	$\cdots$	$z > 3.5$
	1:4 satellites / logM=10.2	
UltraVISTA	$z = 2.7$	$z = 2.4$
CANDELS	$\cdots$	$z = 3.0$
	1:10 satellites / logM=9.8	
UltraVISTA	$z = 2.4$	$z = 1.5$
CANDELS	$\cdots$	$z = 2.5$

Note. — We tabularize the redshift and resolution limits to which we are complete for even the faintest low surface brightness galaxies (maximally old stellar population) of the given stellar masses for a range of Sersic profiles. The second column are the redshift limits for stellar mass completeness of $> 75\%$ derived by comparing UltraVISTA galaxies to the deeper FIREWORKS catalog, as described in Appendix 3.A.1. The third column shows the Sersic tested SB limits derived by simulating maximally old galaxies of a range of Sersic profiles, as detailed in Appendix 3.A.2. We list the redshift to which the catalogs are complete to the detection of such galaxies with the Sersic profiles simulated.

3.A.2.1 Sizes

Considering the above mentioned possibilities, we simulate the two extreme sizes of a $M_\star = 10^{9.8} M_\odot$ quiescent galaxy: the most compact (constant stellar density: $R \propto M_\star^{1/3}$) and the most extended (simulation: $R_{massive} = R_{intermediate}$). Observations show that a $M_\star = 10^{10.8} M_\odot$ quiescent galaxy has $\log(r_e/kpc) \sim 0.2$ at $1.5 < z < 2$ and $\log(r_e/kpc) \sim 0.04$ at $2 < z < 2.5$ (Williams et al., 2010; Newman et al., 2012; Cassata et al., 2013), with a scatter of $\sigma_{log(r_e)} \sim 0.25$. We scale the sizes to one-tenth of the stellar mass with the extreme scenarios, e.g. our simulated $M_\star = 10^{9.8} M_\odot$ galaxy at $z = 2.5$ has r_e of 0.29 kpc (compact) to 1.95 kpc (extended), equivalent to 0.035″ and 0.248″.

3.A.2.2 Magnitudes

We assume a maximally old, dust-free stellar population with a single burst and highest metallicity (Z=0.03) to compute the faintest possible magnitudes for these intermedi-

ate mass galaxies using the updated version (2012) of the stellar population synthesis model library of Bruzual & Charlot (2003). This corresponds to magnitude limits of $H = 26.34$ and $K = 25.41$ for a $M_\star = 10^{9.8} M_\odot$ maximally old galaxy at $z = 2.5$.

3.A.2.3 Other assumptions

We simulate different light profiles using three Sersic indices (n =[0.5, 1, 4]), in which the latter two represent the exponential disk profile and the de Vaucouleurs profile respectively. We assume two axial ratios of $q = [0.5, 1]$, though we note that lower axial ratios are easier to detect when the source is closer to the SB limit.

3.A.2.4 Method and results

With the assumed parameters we generate Sersic models according to the H and K limits. We smooth the images with a Gaussian beam corresponding to the PSF size of the imaging surveys. Then we add them to blank regions on the CANDELS-wide H-band and the UltraVISTA K-band images, and we extract sources from the simulated images with the corresponding SExtractor settings of the two surveys.

We outline the results of our simulation for both catalogs. For the UltraVISTA DR1 catalog, as long as the source is brighter than K=24.2-24.3 mag arcsec^2, we are able to extract the sources for all the Sersic models simulated. This corresponds to $z = 2.4$ (1.5) for using UltraVISATA DR1 to detect major (minor) satellites. The limit for the CANDELS wide catalog is H=26.45 mag arcsec^2, corresponding to $z = 3$ (2.5) for major (minor) satellites. We note that these limits are more constraining that those derived from a simple stellar mass completeness argument (Appendix 3.A.1).

From this test we observe that the source detection for faint objects close to the SB limit depends on the following structural parameters: (1) r_e: for a given integrated magnitude, the larger the r_e the lower the SB per pixel. Sufficient pixels (10 pixels following UltraVISTA and CANDELS settings) above the SB threshold are required for a detection; (2) n: for a given integrated magnitude, the combination of a very low n and very extended r_e may lead to too low SB/pix for detection. On the other hand, for a very high n and very compact r_e a non-detection may result due to the insufficient number of pixels above the detection threshold; (3) q: if the axis ratio is close to 1, the flux densities are divided over more pixels than the case of a lower q, resulting in an insufficient number of pixels above the detection threshold.

We note that our derived limits may be subject to change, if there are systematic uncertainties in the magnitudes and/or the stellar mass. Namely, the magnitude limits are derived from dust-free models, which may be reasonable assumptions given that the faintest possible galaxies at $z = 2.5$ are not actively star-forming. On the other hand, there are known systematic uncertainties in stellar masses (~ 0.2 dex) and ages

from SED fitting due to different assumptions of IMF or stellar population synthesis model. If the modeled magnitudes are actually fainter or if the stellar masses are underestimated, then our SB completeness limit may be lower than the numbers quoted here.

3.B COMPARISON WITH OTHER MERGER FRACTION STUDIES

We only compare our results with previous merger fraction measurements using the close pair selection but not the morphological selection (e.g. Le Fèvre et al., 2000; Conselice et al., 2003; Lotz et al., 2008c; Heiderman et al., 2009; Jogee et al., 2009; Bluck et al., 2012). As the morphological selection is sensitive to the imaging quality, merger fraction measurements may be subject to large systematic uncertainties beyond $z \sim 1$. We refer readers to Lotz et al. (2011) for a comprehensive review on the two methods, and focus on comparing our results with works that use the close pair method to identify mergers. We note that for the few studies which cover a different R_{proj} range than our data points shown on Figure 3.B.1, we use the observability timescales of Lotz et al. (2010) to correct the merger fractions for a fair comparison.

3.B.1 MERGER FRACTION AT $z \geqslant 1.2$

We compare our merger fractions with $z \geqslant 1.2$ studies using the close pair selection. As the selection criteria vary slightly across studies, we re-run our selection according to the published studies for a fair comparison.

We compare our merger fractions with similar studies that select mergers using the stellar mass ratio (Williams et al., 2011; Newman et al., 2012) [2]. In these studies, the projected separation limits are R_{proj} = 13-30 kpc h^{-1} and 10-30 kpc h^{-1} respectively. We replicate the selections by slightly modifying our criteria: we search for satellites around massive quiescent galaxies ($M_\star \geqslant 10^{10.8} M_\odot$ and sSFR $< 10^{-10.7}$), using a limit of R_{proj}=10-30 kpc h^{-1}. We note that the results of Newman et al. (2012) are based on satellites around quiescent galaxies at lower stellar masses ($M_\star \geqslant 10^{10.5} M_\odot$). We check that lowering the stellar mass cut by 0.3 dex gives consistent merger fractions within the large Poisson uncertainties, as is also shown in Newman et al. (2012, Table 3). The comparison is shown in Figure 3.B.1 (left). We find our f_{major} to be consistent with that of Newman et al. (2012), and the one measured from UltraVISTA is $\sim 1-2\sigma$ higher than that from Williams et al. (2011) at $z \sim 1$ and 1.8. We note that in these redshift bins, Williams et al. (2011) show slightly higher f_{minor} than in other fields. Therefore we conclude that the combined f_{major} and f_{minor} measured in our data and in Williams et al. (2011) are in good agreement. The discrepancy of $\sim 3\%$ in the f_{major} can be

[2] In the case of Newman et al. (2012), we convert their mass limit from a Salpeter IMF to a Chabrier IMF to match this study.

explained by the separation of major and minor mergers, as well as cosmic variance and photo-z criterion variation. This discrepancy does not affect the conclusions made in this work.

Bluck et al. (2009) and Man et al. (2012) search for satellites of H-band flux ratios down to 4:1 around galaxies more massive than $10^{11}M_{\odot}$, within projected separations of $R_{proj} \leqslant 30$ kpc, i.e. 21 kpc h^{-1}. In particular, Bluck et al. (2009) impose a lower limit of $R_{proj} > 5$ kpc to screen out confused pairs which are likely unresolved with NICMOS. This comparison is illustrated in Figure 3.B.1 (right). Our f_{major} is consistent with these studies.

Ryan et al. (2008) present the first measurement of the f_{major} at $z > 1$ in the HUDF using the stellar mass ratio selection. They use a smaller $R_{proj} \leqslant 20$ kpc h^{-1} and search for satellites around galaxies of $10^{10}M_{\odot}$, which is six times lower than our mass criteria. This may explain why their f_{major} to be 50% higher than ours.

As discussed in Section 3.4.3, flux-limited spectroscopic surveys may lead to biased merger fractions due to mass incompleteness, slit/fiber collision, etc. Bearing in mind the difference in the merger selection, we compare our results using photometric mergers with those using spectroscopic mergers. Our results are consistent with López-Sanjuan et al. (2011) who measure the f_{major} and f_{minor} of $\gtrsim L^{\star}_{B}$ galaxies from the spectroscopic survey of VVDS up to $z \sim 1$ using the B-band flux ratio selection. The observed H-band corresponds approximately to the rest-frame B-band at $z \sim 2.5$ and therefore our results using the flux ratio selection are directly comparable to their work. López-Sanjuan et al. (2013) and Tasca et al. (2014) extend measurements of spectroscopic merger fractions to $z > 1.2$, in which the former use a flux ratio selection for star-forming galaxies and the latter a stellar mass ratio selection. Both works report a f_{major} of $15 - 20\%$. Our major merger fraction are marginally consistent with that of López-Sanjuan et al. (2013) although we note that their primary sample consists of star-forming galaxies only, and may include more mergers if merging does trigger star formation activity. Our merger fractions are $\gtrsim 10\%$ lower than that of Tasca et al. (2014). Both of these studies sample the mergers around less massive galaxies (0.8-1.7 dex lower than our mass limit), and we speculate that it may account for the higher fractions.

3.B.2 MERGER FRACTION AT $z \leqslant 1.2$

Our merger selection criteria are very similar to those of Bundy et al. (2009), López-Sanjuan et al. (2012) and Xu et al. (2012a) so we detail our comparison here.

Bundy et al. (2009) select mergers photometrically with the K-band flux ratio, and report a mildly increasing f_{major} for massive ($> 10^{11}M_{\odot}$) galaxies from $z = 0$ to 1.2. When compared to our f_{major} using the H-band flux ratio for the similar $M_{\star}$ and R_{proj} range (Figure 3.B.1, right), our results are in good agreement with theirs.

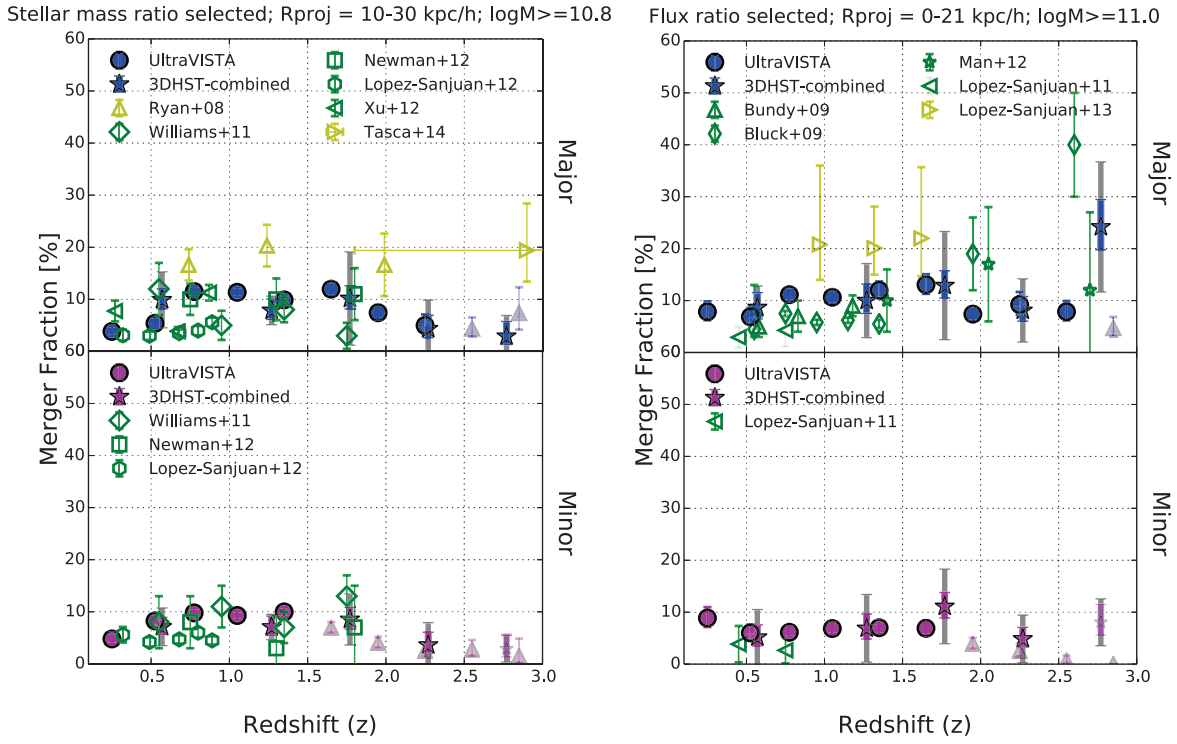

Figure 3.B.1: A comparison of the major (blue filled symbols) and minor (magenta) merger fractions presented in this work with other close pair studies using similar selection criteria. The literature points are plotted in green / yellow open symbols. The green points represent the works directly comparable to our stellar mass range and the yellow points show the works concerning mergers around less massive galaxies ($\log(M_\star/M_\odot) < 10.5$). We use the stellar mass ratio selection (left) and the H-band flux ratio selection (right) following the two methods for the respective works, as described in Section 3.3.1.1. ***Left:*** Stellar mass ratio selected mergers (Ryan et al., 2008; Williams et al., 2011; López-Sanjuan et al., 2012; Newman et al., 2012; Xu et al., 2012a; Tasca et al., 2014). We search for satellites within $10 \leqslant R_{proj} \leqslant 30$ kpc h^{-1} around massive quiescent ($\log(M_\star/M_\odot) \geqslant 10.8$ and log(sSFR)<-10.7) galaxies. ***Right:*** H-band flux ratio selected mergers (Bundy et al., 2009; Bluck et al., 2009; López-Sanjuan et al., 2011; Man et al., 2012; López-Sanjuan et al., 2013): We search for satellites with $R_{proj} \leqslant 30$ kpc ($R_{proj} \leqslant 21$ kpc h^{-1}) around massive ($\log(M_\star/M_\odot) \geqslant 11$) galaxies using the H-band flux ratios. As we show in Section 3.3.1.1, the "major" flux ratio selection includes "minor" stellar mass ratio mergers at $z > 1.5$. This leads to an increasing merger fraction at $z > 1.5$. There are slight differences among the merger selections as described in Appendix 3.B. We find consistent conclusions with these studies that the major and minor merger fractions are flat or even diminishing when the stellar mass ratio selection is used, but an increasing trend is observed at $z > 1.5$ when the flux ratio is used.

López-Sanjuan et al. (2012) measure the f_{major} and f_{minor} of massive ($> 10^{11} M_\odot$) galaxies in zCOSMOS at $z = 0 - 1$, selecting mergers by stellar mass ratio and relative

velocity $\delta\nu \leq 500$ km s-1. They find a redshift dependence of the f_{major} as $(1+z)^{1.4}$, and a redshift-constant f_{minor} in this redshift range. Xu et al. (2012a) present results for f_{major} at $z = 0 - 1$ for COSMOS with similar selection criteria. We compare to their f_{major} for galaxies with log($M_\star/M_\odot$)=11-11.4. Our results are consistent to these two works, as shown in Figure 3.B.1 (left).

Lotz et al. (2011) demonstrate that the variation in selecting the parent galaxy sample and the mass ratio probe leads to different redshift trends in the merger fraction. Therefore we do not compare our results directly with the pair fraction measurements at $z \leqslant 1.2$ with different selection criteria (e.g. Bundy et al., 2004; Xu et al., 2004; Bell et al., 2006a; De Propris et al., 2007; Kartaltepe et al., 2007; Lin et al., 2008; McIntosh et al., 2008; Patton & Atfield, 2008; Rawat et al., 2008; de Ravel et al., 2009; Robaina et al., 2010; de Ravel et al., 2011). We note that once the selection differences are accounted for, the merger rate per galaxy presented in Section 3.3.3.2 of this work is consistent with those inferred from these works as presented in Lotz et al. (2011): both follow a monotonically increasing trend from $z \sim 0$ to $z \sim 1.2$.

4

ARE QUIESCENT GALAXIES TRULY PASSIVE?

Confirming the Quiescent Galaxy Population out to $z = 3$: A Stacking Analysis of Mid-, Far-Infrared and Radio Data

Allison W. S. Man[1,2], Thomas R. Greve[3], Sune Toft[1], Benjamin Magnelli[4], Alexander Karim[4], Olivier Ilbert[5], Mara Salvato[6], Emeric Le Floc'h[7], Frank Bertoldi[4], Caitlin M. Casey[8], Nicholas Lee[2], Yanxia Li[2], Felipe Navarrete[4], Kartik Sheth[9], Vernesa Smolčić[10], David B. Sanders[2], Eva Schinnerer[11], and Andrew W. Zirm[1]

[1] Dark Cosmology Centre, Niels Bohr Institute, University of Copenhagen, Denmark
[2] Institute for Astronomy, 2680 Woodlawn Drive, University of Hawaii
[3] Department of Physics and Astronomy, University College London
[4] Argelander-Institut für Astronomie, Universität Bonn
[5] Aix Marseille Université, CNRS, Laboratoire d'Astrophysique de Marseille
[6] Max-Planck-Institut für extraterrestrische Physik
[7] Laboratoire AIM, CEA/DSM/IRFU, CNRS, Université Paris-Diderot
[8] Department of Physics and Astronomy, University of California, Irvine
[9] National Radio Astronomy Observatory
[10] Physics Department, University of Zagreb
[11] Max-Planck-Institut für Astronomie

Submitted to the Astrophysical Journal Letters on 11$^{\rm th}$ November 2014
arXiv preprints: 1411.2870

Abstract

We present stringent constraints on the average mid-, far-infrared and radio emissions of ∼14200 quiescent galaxies (QGs), identified out to $z = 3$ in the COSMOS field via their rest-frame NUV−r and r−J colors, and with stellar masses $M_\star = 10^{9.8-12.2}\,M_\odot$. Stacking in deep *Spitzer* (MIPS $24\,\mu$m), *Herschel* (PACS and SPIRE), and VLA (1.4 GHz) maps reveals extremely low dust-obscured star formation rates for QGs (SFR < 0.1–$3\,M_\odot\mathrm{yr}^{-1}$ at $z \leqslant 2$ and $<$ 6–$18\,M_\odot\mathrm{yr}^{-1}$ at $z > 2$), consistent with the low unobscured SFRs (< 0.01–$1.2\,M_\odot\mathrm{yr}^{-1}$) inferred from modeling their ultraviolet-to-near-infrared photometry. The average SFRs of QGs are $> 10\times$ below those of star-forming galaxies (SFGs) within the $M_\star$- and z-ranges considered. The stacked 1.4 GHz signals (S/N > 5) are, if attributed solely to star formation, in excess of the total (obscured plus unobscured) SFR limits, suggestive of a widespread presence of low-luminosity active galactic nuclei (AGN) among QGs. Our results reaffirm the existence of a significant population QGs out to $z = 3$, thus corroborating the need for powerful quenching mechanism(s) to terminate star formation in galaxies at earlier epochs.

4.1 INTRODUCTION

Half of the most massive ($M_\star \geqslant 10^{11}\,M_\odot$) galaxies at $z \sim 1.5$ have evolved stellar populations and SFRs of only a few $M_\odot$ yr^{-1} (e.g., Ilbert et al., 2013, and references therein), suggesting that they have undergone a rapid build-up of stellar mass followed by an effective phase of star formation (SF) quenching, probably via AGN feedback (e.g., Bower et al., 2006; Croton et al., 2006). If significant dust is present in these galaxies, however, it would imply that the SFRs, inferred from the rest-frame ultraviolet (UV), are severely underestimated, and that their stellar populations are in fact not old but simply reddened by the dust. Direct far-infrared (FIR) measurements of the dust are therefore essential to unambiguously assess the level of obscured SF. A recent *Herschel* stacking analysis by Viero et al. (2013) found that massive QGs at $z > 2$ have IR luminosities comparable to local ultra-luminous IR galaxies (ULIRGs, $L_{\rm IR} \geqslant 10^{12}\,L_\odot$), inconsistent with the quiescence inferred from the UV continua (e.g., Ilbert et al., 2013) as well as their low $24\,\mu$m stacked flux densities (Fumagalli et al., 2013; Utomo et al., 2014). If QGs harbor significant dust-obscured SF, it would challenge the need for powerful quenching mechanisms.

Here, we analyze a sample of ∼14200 QGs with $M_\star = 10^{9.8-12.2}\,M_\odot$ out to $z = 3$, selected over 1.48 deg^2 in the COSMOS field. Taking advantage of the available deep multi-wavelength data, we constrain their dust-obscured SFRs through stacking in *Spitzer* Multiband Imaging Photometer (MIPS), *Herschel* Photodetector Array Camera and Spectrometer (PACS; Poglitsch et al. 2010) and Spectral and Photometric Imaging Receiver (SPIRE; Griffin et al. 2010) maps. These are compared with stacks in deep Very Large Array (VLA) radio maps. We infer extremely low levels of dust-obscured SF ($< [0.3, 3, 18]\,M_\odot$yr^{-1} at $z \sim [0.8, 1.7, 2.6]$), thus definitively confirming the quiescent nature of these galaxies.

Magnitudes are quoted in the AB system. We adopt a Chabrier (2003) initial mass function, and H_0 = 70 km s^{-1} Mpc^{-1}, $\Omega_{\rm M}$ = 0.3 and Ω_Λ = 0.7.

4.2 DATA AND SAMPLE SELECTION

We select galaxies brighter than $K_s = 24$ from the UltraVISTA survey (McCracken et al., 2012) that have $M_\star \geqslant 10^{9.8}\,M_\odot$ and photometric redshifts $z_{\rm phot} = 0.1-3.0$. Both $M_\star$ and $z_{\rm phot}$ are from Ilbert et al. (2013), derived from spectral energy distribution (SED) fits to broadband UV-to-IRAC photometry (Capak et al., 2007; Scoville et al., 2007b). A small number of AGN, identified via their emission in X-rays (Brusa et al., 2010; Civano et al., 2012), IRAC bands (Donley et al., 2012), or the radio (Schinnerer et al., 2007, 2010), are removed to minimize the effects of erroneous SED fits and thus inaccurate $z_{\rm phot}$ and $M_\star$. Including the AGN in the analysis does not change the stacked flux densities (within the uncertainties) nor the conclusions of this Letter.

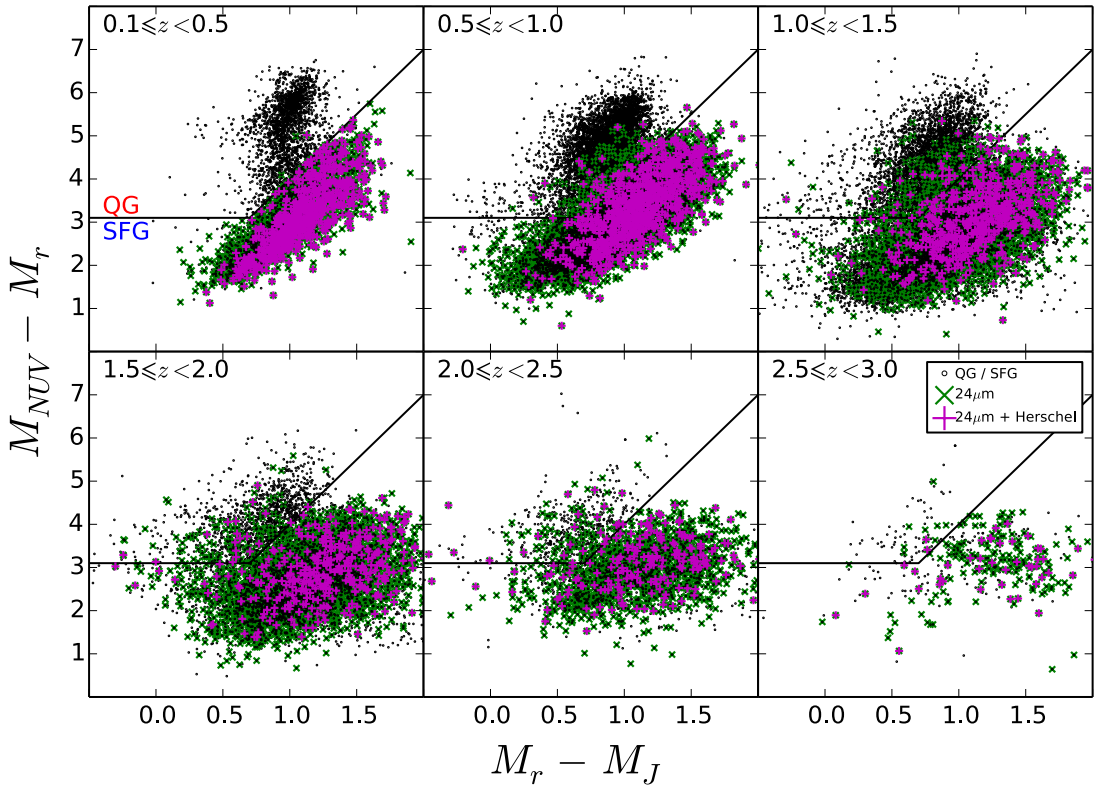

Figure 4.1: Rest-frame NUV−r and r−J colors for galaxies above the mass-completeness limits (small black circles) from the UltraVISTA survey. QGs are defined as having $M_{\rm NUV} - M_{\rm r} > 3(M_{\rm r} - M_{\rm J}) + 1$ and $M_{\rm NUV} - M_{\rm r} > 3.1$. The QGs/SFGs classification boundary is marked by black solid lines. Galaxies with $\mathrm{SFR}_{24} > 20\,M_{\odot}\mathrm{yr}^{-1}$ (green crosses) and *Herschel* detections (magenta pluses) are indicated (fractions of the total QG sample are listed in Table 4.1).

Each galaxy is classified as a QG or a SFG based on its rest-frame NUV−r and r−J colors (Figure 4.1). NUV−r is a measure of the amount of UV light from young stars (i.e., recent SF) relative to the red optical light from evolved stellar populations, while r−J constrains the degree of dust attenuation in the red part of the spectrum. The QGs are divided into six bins of $z_{\rm phot}$, each of which is split into four $M_{\star}$-bins (see Table 4.1); however, only $M_{\star}$-bins which are $> 90\%$ mass-complete (according to the limits presented in Ilbert et al. 2013) are included.

To weed out dusty galaxies erroneously classified as QGs, we cross-correlate our sample with the MIPS $24\,\mu$m catalog of Le Floc'h et al. (2009) with a radius of $2''$. A redshift-dependent $24\,\mu$m flux density (S_{24}) cut-off is then applied to remove QGs with dust-obscured SFRs $> 20\,M_{\odot}\mathrm{yr}^{-1}$ (as inferred from their S_{24} — see Section 4.4.2).

The fraction ($f_{\rm QG,24}$) of QGs with $24\,\mu$m-inferred SFRs $> 20\,M_{\odot}\mathrm{yr}^{-1}$ increases with redshift and peaks at 13–19% for the most massive $z \gtrsim 2$ QGs (see Table 4.1). This

Table 4.1. *Spitzer* $24\,\mu$m and *Herschel* detected fractions for QGs

	$\log(M_\star/M_\odot)$			
	11 – 12.2	10.6 – 11	10.2 – 10.6	9.8 – 10.2
Redshift	$f_{\rm QG,24}$ ($f_{\rm QG,H}$)	$f_{\rm QG,24}$ ($f_{\rm QG,H}$)	$f_{\rm QG,24}$ ($f_{\rm QG,H}$)	$f_{\rm QG,24}$ ($f_{\rm QG,H}$)
0.1 – 0.5	0% (0%)	0.4% (0.2%)	0% (0%)	0.2% (0%)
0.5 – 1.0	4.6% (1.4%)	4.0% (1.0%)	2.2% (0.3%)	0.4% (0.1%)
1.0 – 1.5	9.9% (2.4%)	5.3% (1.0%)	2.4% (0%)	0.6% (0%)
1.5 – 2.0	8.8% (1.5%)	9.0% (1.4%)	7.5% (1.0%)	···
2.0 – 2.5	19.4% (6.0%)	17.4% (2.5%)	···	···
2.5 – 3.0	13.3% (2.7%)	···	···	···

Note. — $f_{\rm QG,24}$ is the fraction of QGs (classified by their NUV−r and r−J colors) with $24\,\mu$m-inferred SFRs $> 20\,M_\odot{\rm yr}^{-1}$. $f_{\rm QG,H}$ is the fraction of QGs fulfilling the above $24\,\mu$m criterion that are also detected in at least two *Herschel* PACS+SPIRE bands (S/N $\geqslant 5$).

suggests a higher fraction of misclassified QGs at $z \gtrsim 2$, which is unsurprising given their faintness (i $\gtrsim 25$). Overall, however, the fractions are reassuringly small. A similar conclusion is reached from the fraction ($f_{\rm QG,H}$) of *Herschel* detected QGs ($< 6\%$), determined using the catalog of Lee et al. (2013) in which the $24\,\mu$m sources are cross-identified to the *Herschel* detections (i.e., S/N $\geqslant 5$ in at least two PACS or SPIRE bands). This population of dusty galaxies having quiescent NUV−r and r−J colors could either be SFGs with strong attenuation, or galaxies containing evolved stellar populations and undergoing rejuvenation of SF (Lemaux et al., 2013). The robust *Herschel* detections in the QG region tend to lie close to the QG/SFG classification boundary at least out to $z = 1.5$ (Figure 4.1), perhaps indicative of their post-starburst nature (Hayward et al., 2014).

For the stacking analysis (Section 4.3) we use the aforementioned MIPS $24\,\mu$m imaging (FWHM $\simeq 6''$) from Sanders et al. (2007), while the *Herschel* PACS and SPIRE maps are from the PACS Evolutionary Probe survey (PEP; Lutz et al. 2011) and the *Herschel* Multi-tiered Extragalactic Survey (HerMES; Oliver et al. 2012), respectively. The PACS maps reach depths of 5 and 10.3 mJy beam^{-1} (3σ) at 100 and 160 μm, respectively (FWHM $\simeq 6.8''$ and $11''$), and SPIRE 250, 350, and 500 μm depths are 8, 11,

and 13 mJy beam^{-1} (3σ), respectively (FWHM $\simeq$ 18.2″, 24.9″, and 36.3″). For the radio stacking we use the 1.4 GHz VLA-COSMOS large survey (Schinnerer et al., 2007, 2010), which reaches a root-mean-square noise (rms) of 15 μJy beam^{-1} at an angular resolution of $\sim 1.5''$ (FWHM).

4.3 STACKING

Our *Herschel* maps are characterized by a high level of source confusion which, if unaccounted for, will bias a stacked signal (Marsden et al., 2009; Béthermin et al., 2010; Kurczynski & Gawiser, 2010; Viero et al., 2013). Here, we use a global deblending technique similar to that of Kurczynski & Gawiser (2010) but generalized to deblend multiple galaxy samples simultaneously, which in our case totaled 87 samples (separated by their SFG/QG classifications, z- and $M_\star$-bins, and SFR$_{24}$ threshold).

Source confusion is not an issue for our radio maps due to the high angular resolution, and the stacked signal of a given sample was determined from the median combination of the galaxy postage stamps belonging to the sample. The MIPS $24\,\mu$m stacks were determined in a similar way, despite the larger beam size. To ensure that our $24\,\mu$m median stacks were not biased, we stacked samples of SFGs using the global deblending technique and found excellent agreement with the median results. The $24\,\mu$m flux densities were measured on the stacked images using an aperture radius of 3.5″ with aperture corrections applied following the MIPS handbook. For the radio fluxes we adopted the central pixel values. In both cases the errors were estimated from the rms of the background in the stacked images.

4.4 RESULTS

4.4.1 PANCHROMATIC UV-TO-RADIO SEDS OF QGS

The stacked MIPS $24\,\mu$m, *Herschel*, and radio flux densities of the z- and $M_\star$-bins of QGs are listed in Table 4.1. None of the QG samples are significantly detected (i.e., S/N > 3) in any of the *Herschel* stacks. The most massive ($M_\star \geqslant 10^{10.6}\,M_\odot$) QGs are detected at all redshifts out to $z = 3$ in the $24\,\mu$m stacks (S/N $\sim$ 5–26) and out to $z = 1.5$ in the radio stacks (S/N $\sim$ 4–10). The intermediate-mass QGs ($M_\star < 10^{10.6}\,M_\odot$) are detected at $24\,\mu$m (S/N $\sim$ 5–20) but not in the radio (S/N $\leqslant 3$) in all relevant (i.e., mass-complete) redshift bins. As expected, S_{24} and $S_{\rm radio}$ decrease with z (cosmic dimming) and increase with $M_\star$.

Figure 4.1 summarizes our constraints on the SEDs of QGs at mid-, far-IR, and radio wavelengths along with the median UV-to-near-IR SEDs. Note, the *Herschel* non-detections are shown as 3σ upper limits (i.e. $3\sigma_{\rm map}/\sqrt{N_{\rm stack}}$, where $\sigma_{\rm map}$ is the map rms noise and $N_{\rm stack}$ the number of galaxies in the stack). For comparison we show the

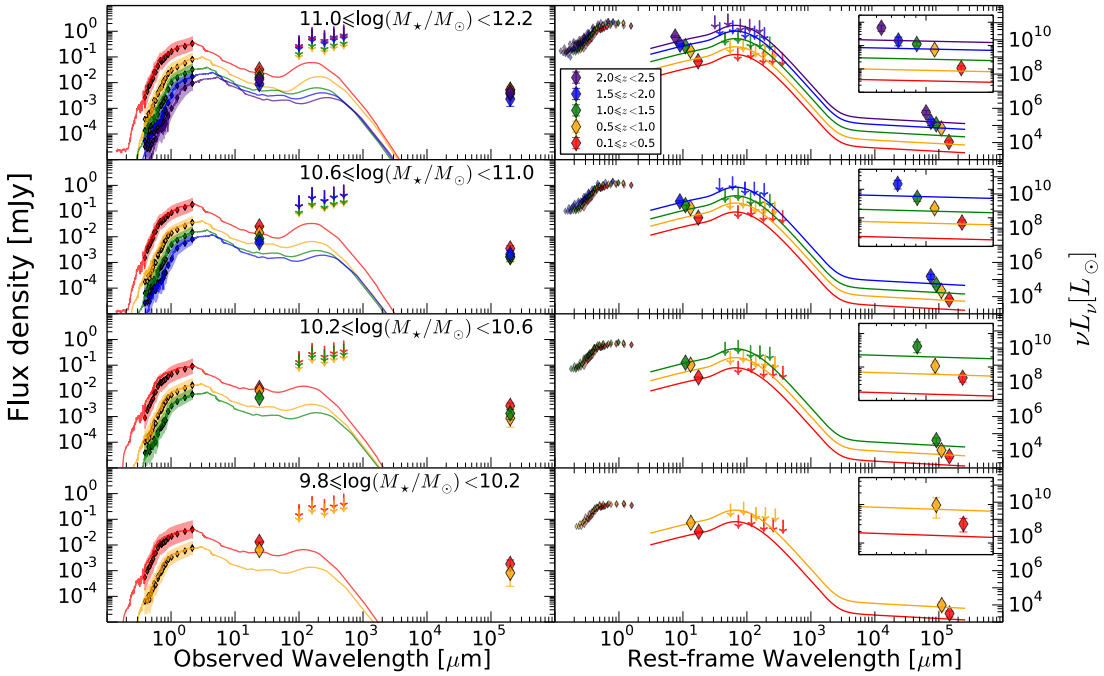

Figure 4.1: Panchromatic SEDs of QGs in four $M_\star$- bins (rows) and six z- bins (colors) in observed (left) and rest-frame (right) frames. The median UV-to-near-IR photometry is plotted and shaded with its standard deviations. The longer wavelength data represent our stacking results. *Left*: At $z > 0.5$ the observed S_{24} are higher than that expected from pure stellar emissions of elliptical galaxy models of Bruzual & Charlot 2003 (matched to the median stellar ages from SED fits and scaled to K-band magnitudes). *Right*: The FIR black-body models (Casey, 2012) fitted to the *Herschel* upper limits (assuming $T_{\rm dust} = 30\,{\rm K}$) are co-joined with a radio power-law ($\alpha = -0.8$) and plotted as lines, following the radio-FIR correlation presented in Ivison et al. (2010) with shallow redshift evolution. The templates are not fitted to the radio data. Shown in the insets, the observed $S_{\rm radio}$ is higher than expected from SF. The $24\,\mu{\rm m}$ and radio excesses suggest contributions from low-luminosity AGN.

SED template of a dust-free elliptical galaxy (Bruzual & Charlot, 2003) scaled to match the UV-to-near-IR median photometry of the QGs (Figure 4.1, left). The model, which represents pure stellar emission, is insufficient to fully account for the stacked $24\,\mu{\rm m}$ flux densities. If we instead fit a modified black-body law (see details in Section 4.4.2) to the *Herschel* limits, add radio emission (a power-law with slope $\alpha = -0.8$) such that the radio-FIR correlation (Ivison et al., 2010) is fulfilled, we still fall short of the stacked 1.4 GHz fluxes (Figure 4.1, right panels). The implications of this excess emission at $24\,\mu{\rm m}$ and 1.4 GHz are discussed in Section 4.4.3.

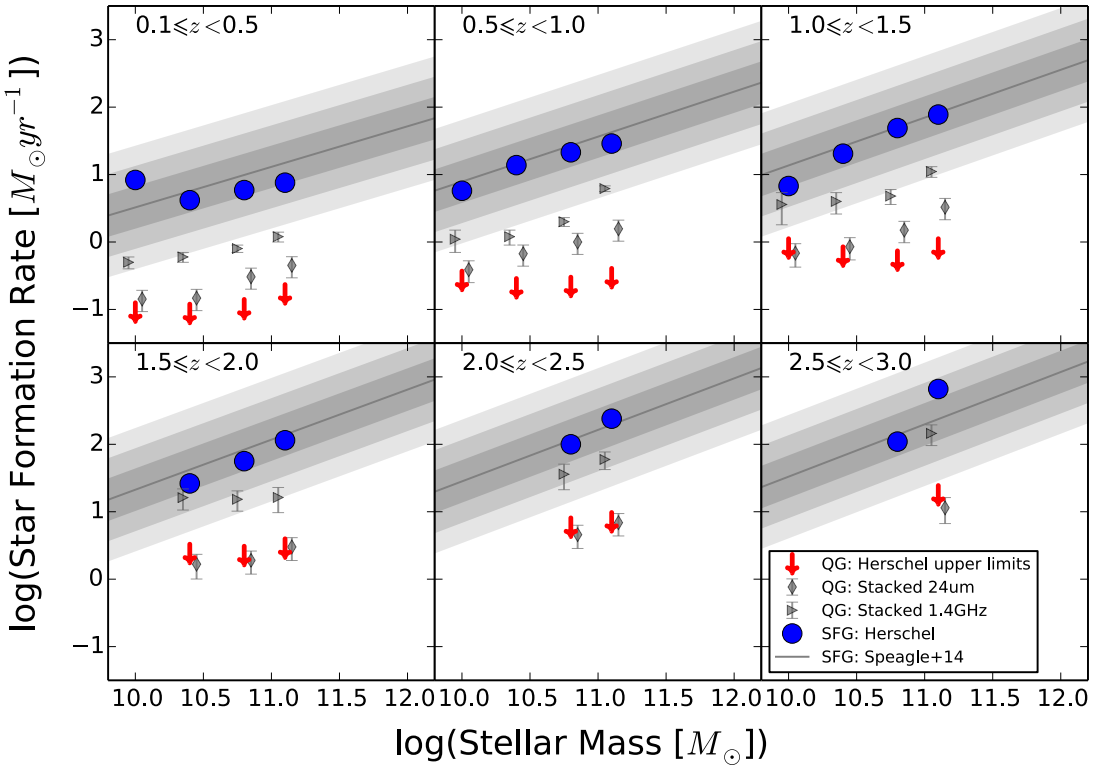

Figure 4.2: SFRs inferred from stacking as a function of $M_\star$ and z. Blue circles and red downward arrows represent the SFRs from global deblending and stacking in *Herschel* for SFGs and QGs respectively, with the latter ones representing 3σ upper limits for QGs since they are consistent with no detection. Assuming the $24\,\mu$m and radio emissions originate from SF only, we plot the inferred SFRs as gray diamonds and triangles. $\mathrm{SFR_{radio}}$, as well as $\mathrm{SFR_{24}}$ at $z < 1.5$, show clear offsets from $\mathrm{SFR_H}$ for QGs, therefore part of the radio emission in QGs likely arises from low-luminosity AGN. The SFR-$M_\star$ measured in a recent compilation (Speagle et al., 2014) is plotted as gray lines, and the $1-3\times$ observed dispersion (σ_{SFR}=0.3) are shown as dark-to-light shades. QGs have SFRs at least $\gtrsim 1$ dex below those of SFGs out to $z \sim 3$.

4.4.2 Where do QGs lie relative to the SFGs on the SFR-$M_\star$ relation?

The mid-, far-IR and radio stacks each provide an independent measurement of the dust-obscured SFRs in our QGs. Firstly, we estimate the 8 to 1000 μm rest-frame IR luminosity (L_{IR}) from S_{24} using the calibration by Rujopakarn et al. (2013), including the 0.13 dex scatter of the calibration in the error budget. Independent L_{IR} upper limits are then obtained by redshifting and scaling a modified black-body model to the *Herschel* 3σ upper limits using the IDL code of Casey (2012). We use an optically thick, modified black-body law with a fixed dust temperature ($T_{\mathrm{dust}} = 30\,\mathrm{K}$) and emissivity 1.5. Note

that $L_{\rm IR}$ is insensitive to $T_{\rm dust}$, as it only varies by less than a factor of two if we assume $T_{\rm dust} = 15\,{\rm K}$ or 50 K instead. For each of our QG samples, $L_{\rm IR}$ is estimated in the above manner using the median $z_{\rm phot}$ (listed in Table 4.1), and subsequently converted into an obscured SFR using the $L_{\rm IR}$-SFR calibration by Kennicutt (1998) adjusted to the IMF used in this work. Assuming that all the radio emission originates from SF, and a radio spectral index $\alpha = -0.8$, rest-frame 1.4 GHz luminosities ($L_{1.4\,{\rm GHz}}$) are derived from the radio stacks and subsequently converted to ${\rm SFR}_{\rm radio}$ using the $L_{1.4\,{\rm GHz}}$-SFR calibration by Bell (2003).

The *Herschel* $L_{\rm IR}$ upper limits and the (specific) SFRs for QGs as a function of $M_\star$ and z are listed in Table 4.1. The *Herschel* upper limits put stringent constraints on the dust-obscured SFR: $< 1\,M_\odot{\rm yr}^{-1}$ at $z < 1.5$ and at most $< 18\,M_\odot{\rm yr}^{-1}$, i.e., sSFR $\leqslant 10^{-(10-12)}{\rm yr}^{-1}$, across all z and $M_\star$ bins. These limits are consistent with the quiescence inferred from the unobscured SFR from UV-to-IRAC SED fits (0.01–$1.2\,M_\odot$ yr^{-1}, see Table 4.1). QGs form stars at a very modest rate ($>10\times$ lower than SFGs, Figure 4.2). As a consistency check, we find that the stacked *Herschel* flux densities of SFGs obtained from global deblending and stacking (Kurczynski & Gawiser, 2010) are in good agreement with those from median combination, and we recover the SFR-$M_\star$ sequence found in a recent compilation of similar measurements (Speagle et al. 2014, Figure 4.2).

4.4.3 DO QGS HOST AGN?

${\rm SFR}_{24}$ are consistent with ${\rm SFR}_{\rm H}$, except at $z < 1.5$ in which ${\rm SFR}_{24}$ is higher than ${\rm SFR}_{\rm H}$ (by as much as $5\times$), as shown in Figure 4.2. This discrepancy could be explained by the following factors not related to recent SF: (1) The Rayleigh-Jeans tail of the stellar photospheric emission, which is dominated by red giants; (2) Circumstellar dust envelops of asymptotic giant branch (AGB) stars (Knapp et al., 1992; Piovan et al., 2003); (3) Interstellar (cirrus) dust heated by evolved stellar populations (e.g., Bendo et al., 2012); (4) Polycyclic aromatic hydrocarbon emission associated with (2) and (3) (Kennicutt, 1998; Bendo et al., 2008); (5) Warm dust heated by the obscured AGN (Daddi et al., 2007). The first four factors are viable for galaxies with intermediate-old stellar populations ($> 1\,{\rm Gyr}$, Salim et al. 2009). The elliptical galaxy template from stellar population synthesis models (Bruzual & Charlot, 2003), which accounts for only (1) and to some extend (2), cannot fully reproduce the observed S_{24} at least for $z > 0.5$ (Figure 4.1, left). This suggests that AGN and/or dust heating from evolved stellar populations are likely responsible for the low levels of $L_{\rm IR}$ of QGs (Salim et al., 2009; Bendo et al., 2012; Fumagalli et al., 2013; Utomo et al., 2014). The relative contribution of the above factors depends heavily on the evolution models of AGB stars, dust grain models and interstellar radiation strength, which are actively debated and beyond the scope of this Letter. While we cannot discern the relative contributions of dust heating from these factors using the data in hand, we note that the ${\rm SFR}_{24}$ are likely upper limits if non-SF

processes contribute significantly to S_{24}.

It is interesting that $\mathrm{SFR_{radio}}$ is systematically higher than SFR inferred from $24\,\mu\mathrm{m}$ and *Herschel* as well as UV-to-IRAC SED fits, up to two orders of magnitude in the most extreme case. Compared to the total (obscured + unobscured) SFR inferred from other indicators (*Herschel*, MIPS, UV-to-IRAC SED fitting), the median S_{radio} are inconsistent with originating from SF alone. This is reflected in the low radio index ($q_{24} \equiv \log(S_{24}/S_{\mathrm{radio}})$) listed in Table 4.1 compared to SFGs with typical values of 1.5 – 3 (e.g., Ivison et al., 2010). $L_{1.4\,\mathrm{GHz}}$ [W Hz^{-1}] increases with redshift from $10^{21.5}$ at $z \sim 0.4$ to $10^{23.7}$ at $z \sim 2.6$ for the most massive QGs, where the radio excess is the most prominent (see Figure 4.1 right panel insets). Based on the FIR-radio correlation presented in Ivison et al. (2010) and including the radio-detected QGs in the stack, we estimate that 20-90% of $L_{1.4\,\mathrm{GHz}}$ arises from non-SF processes. This fraction is significantly higher for more massive QGs as shown in Figure 4.1, although we note that if we adopt a more conservative *Herschel* upper limit for the non-detection, the fraction will be lower. Our results indicate that low-luminosity radio AGN may be widespread among massive QGs, echoing the reciprocatory that massive QGs are the preferential hosts for low-luminosity radio AGNs (e.g., Smolčić et al., 2009). However, it is not straightforward to use the median stacked radio luminosity to constrain the heating rate of radio-AGN feedback, without prior assumption of the duty cycle which is not well quantified.

4.5 DISCUSSION

We reject the null hypothesis that the red colors of QGs are due to strong obscured SF, based on a deep FIR stacking analysis. QGs have truly low SFRs and evolved stellar populations, as expected from their low unobscured SFRs measured from the UV continua. The average sSFRs of QGs are at least 1 dex lower than those of SFGs out to $z = 3$. The stacked $24\,\mu\mathrm{m}$ and radio emissions cannot be completely accounted for by low levels of dust-obscured SFR nor stellar emissions, suggesting that low-luminosity AGN may be present in QGs.

Comparing with Fumagalli et al. (2013), who performed $24\,\mu\mathrm{m}$ stacking on 309 QGs with $M_\star \geqslant 10^{10.3}\,M_\odot$, our S_{24} are slightly higher (5–26 μJy vs 2–3 μJy). Their sample is drawn from a smaller survey area equivalent to 11% of the UltraVISTA field, and therefore the discrepancy is likely explained by the fact that their sample is dominated by lower mass galaxies, which have lower S_{24}. Nevertheless, we arrive at similar conclusions — QGs do not host strong obscured SF, and dust heating by evolved stellar populations may be significant at the low levels of L_{IR} observed. Our results indicate that $z \gtrsim 2$ QGs have average $L_{\mathrm{IR}} \leqslant 10^{11.2}\,L_\odot$, i.e., $\geqslant 0.8$ dex below the ULIRG threshold. When we repeat our stacking analysis including QGs detected at $24\,\mu\mathrm{m}$ following the definition of Viero et al. (2013), we obtain higher stacked mid- and far-IR emission, in broad agreement with their results. As QGs have higher $24\,\mu\mathrm{m}$ and *Herschel* detec-

tion fractions at $z \gtrsim 2$ (up to 19% and 6%, respectively, see Table 4.1 and Section 4.2), the inclusion of the quoted fractions of $L_{\rm IR} > 10^{13}\,L_{\odot}$ sources boosts the stacked FIR emission of massive QGs at $z \gtrsim 2$ to be comparable to ULIRGs.

We reaffirm that a population of truly quiescent galaxies is already in place by $z = 3$. This corroborates the need for powerful quenching mechanisms to terminate star formation in galaxies. While environmental quenching may be dominant for intermediate-mass QGs (Peng et al., 2010), stacking analyses at radio (this work) and X-ray (Olsen et al., 2013) wavelengths reveal that massive QGs harbor low-luminosity AGN. AGN provide a viable mechanism for quenching SF in galaxies, as supported by the enhanced AGN fraction among transitory objects between SFGs and QGs (e.g., Barro et al., 2014). After galaxies are quenched, the AGN may then proceed to "maintenance mode" suppressing further SF through a feedback cycle (Schawinski et al., 2009b; Best & Heckman, 2012). With upcoming surveys it will be possible to conduct a complete census of AGN to sample the entire feedback duty cycle and constrain their energetics, in order to quantify their role in quenching star formation in galaxies.

Table 4.1. Stacked flux densities of *Spitzer*/MIPS 24 μm, *Herschel* (PACS+SPIRE), and VLA 1.4 GHz and the inferred SFRs for QGs

Redshift	$\overline{z_{\rm phot}}$	$N_{\rm stack}$	$S_{24\,\mu m}$ [μJy]	$S_{100\,\mu m}$ [mJy]	$S_{160\,\mu m}$ [mJy]	$S_{250\,\mu m}$ [mJy]	$S_{350\,\mu m}$ [mJy]	$S_{500\,\mu m}$ [mJy]	$S_{\rm radio}$ [μJy]	$\rm SFR_{SED}$ [$M_\odot {\rm yr}^{-1}$]	$\rm SFR_{24}$ [$M_\odot {\rm yr}^{-1}$]	$\rm SFR_H$ [$M_\odot {\rm yr}^{-1}$]	$\rm SFR_{radio}$ [$M_\odot {\rm yr}^{-1}$]	$\log(L_{\rm IR,H})$ $\log[L_\odot]$	$\log(\rm sSFR_H)$ $\log[{\rm yr}^{-1}]$	q_{24}
$\log(M_\star/M_\odot)$ = 11 – 12.2 (median = 11.1)																
0.1 – 0.5	0.4	229	32.3±1.5	0.4±0.3	0.3±0.7	0.4±0.5	0.0±0.7	-0.1±0.9	5.2±1.3	0.03	0.4±0.2	<0.2	1.2±0.2	<9.2	< -11.9	0.8
0.5 – 1.0	0.8	1222	21.3±0.8	0.0±0.1	0.2±0.3	-0.2±0.2	-0.2±0.3	-0.1±0.4	5.2±0.5	0.13	1.6±0.5	<0.3	6.2±0.6	<9.5	< -11.7	0.6
1.0 – 1.5	1.2	733	15.9±0.9	0.1±0.2	-0.2±0.4	-0.2±0.3	0.2±0.4	0.4±0.5	3.6±0.6	0.42	3.3±1.1	<0.8	11.1±2.0	<9.9	< -11.2	0.6
1.5 – 2.0	1.7	288	8.8±1.1	-0.4±0.3	-0.4±0.<6	-0.8±0.5	-0.7±0.6	-0.1±0.8	2.3±0.9	0.35	3.0±1.1	<2.9	16.3±6.6	<10.4	< -10.7	0.6
2.0 – 2.5	2.2	174	13.4±1.5	-0.4±0.4	0.5±0.8	-0.4±0.6	-0.1±0.8	0.3±1.0	4.2±1.2	0.71	6.9±2.5	<7.1	59.6±17.4	<10.8	< -10.3	0.5
2.5 – 3.0	2.6	65	10.8±2.2	-0.4±0.6	0.1±1.3	-0.6±1.0	-0.1±1.4	-0.0±1.6	6.5±2.2	1.20	11.4±4.8	<17.6	145.0±49.2	<11.2	< -9.9	0.2
$\log(M_\star/M_\odot)$ = 10.6 – 11.0 (median = 10.8)																
0.1 – 0.5	0.4	502	25.2±1.0	0.6±0.2	1.0±0.5	0.0±0.4	-0.7±0.5	-0.6±0.6	3.5±0.8	0.02	0.3±0.1	<0.1	0.8±0.1	<9.0	< -11.8	0.9
0.5 – 1.0	0.8	2167	14.2±0.6	0.0±0.1	-0.0±0.2	-0.7±0.2	-0.6±0.2	-0.2±0.3	1.7±0.4	0.10	1.0±0.3	<0.2	2.0±0.3	<9.3	< -11.4	0.9
1.0 – 1.5	1.2	1646	8.4±0.5	-0.1±0.1	-0.4±0.3	-1.1±0.2	-1.1±0.3	-0.8±0.3	1.6±0.4	0.23	1.5±0.5	<0.5	4.8±1.2	<9.7	< -11.0	0.7
1.5 – 2.0	1.7	516	6.0±0.8	-0.2±0.2	-0.3±0.5	-1.5±0.3	-1.5±0.5	-0.9±0.6	2.1±0.7	0.30	1.9±0.7	<2.2	15.3±5.1	<10.3	< -10.4	0.5
2.0 – 2.5	2.2	295	8.5±1.2	-0.2±0.3	0.2±0.6	-0.9±0.5	-0.6±0.6	-0.4±0.8	2.3±1.0	0.65	4.6±1.7	<5.9	36.0±14.8	<10.8	< -10.0	0.6
$\log(M_\star/M_\odot)$ = 10.2 – 10.6 (median = 10.4)																
0.1 – 0.5	0.4	699	12.8±0.8	0.5±0.2	1.0±0.4	-0.9±0.3	-1.5±0.4	-1.2±0.5	2.6±0.7	0.01	0.1±0.1	<0.1	0.6±0.1	<8.9	< -11.4	0.7
0.5 – 1.0	0.8	2281	10.1±0.5	0.1±0.1	-0.1±0.2	-1.0±0.2	-1.2±0.2	-0.8±0.3	0.9±0.3	0.06	0.7±0.2	<0.2	1.2±0.3	<9.3	< -11.1	1.1
1.0 – 1.5	1.2	1199	5.4±0.6	-0.1±0.1	0.0±0.3	-1.4±0.2	-1.2±0.3	-0.7±0.4	1.3±0.5	0.15	0.9±0.3	<0.6	4.0±1.4	<9.8	< -10.6	0.6
1.5 – 2.0	1.7	432	5.4±1.0	-0.2±0.2	0.1±0.5	-1.4±0.4	-1.3±0.5	-0.8±0.6	2.2±0.8	0.31	1.7±0.7	<2.4	16.2±5.6	<10.4	< -10.0	0.4
$\log(M_\star/M_\odot)$ = 9.8 – 10.2 (median = 10.0)																
0.1 – 0.5	0.4	583	13.1±0.8	0.3±0.2	0.1±0.4	-1.8±0.3	-2.1±0.5	-1.9±0.5	1.8±0.7	0.01	0.1±0.1	<0.1	0.5±0.1	<8.9	< -11.0	0.9
0.5 – 1.0	0.8	1303	6.4±0.6	-0.1±0.1	-0.1±0.3	-1.2±0.2	-1.3±0.3	-0.7±0.4	0.8±0.4	0.06	0.4±0.1	<0.3	1.1±0.4	<9.4	< -10.6	0.9
1.0 – 1.5	1.2	673	4.5±0.7	0.1±0.2	-0.4±0.4	-1.3±0.3	-1.3±0.4	-0.7±0.5	1.2±0.6	0.21	0.7±0.3	<0.8	3.6±1.8	<9.9	< -10.1	0.6

Note. — The median redshifts ($\overline{z_{\rm phot}}$), the number of QGs stacked ($N_{\rm stack}$), and the stacked flux densities are listed. $\rm SFR_{SED}$ is the median SFR from the UV-to-IRAC SED fitting. We infer SFRs from the stacked flux densities (Section 4.4.2), assuming that the 24 μm and radio emissions originate from SF only. The IR luminosity and specific SFR upper limits ($L_{\rm IR,H}$ and $\rm sSFR_H$) inferred from the *Herschel* upper limits are shown in logarithmic units. The radio index q_{24} is computed as $\log(S_{24\,\mu m}/S_{\rm radio})$.

Acknowledgements

We thank the COSMOS, UltraVISTA, PEP, and HerMES collaborations for providing the data used here. Dark Cosmology Centre is funded by DNRF. AM thanks Anna Gallazzi, Mark Sargent, Ryan Quadri, Brian Lemaux, and Julie Wardlow for helpful discussions. TRG acknowledges support from an STFC Advanced Fellowship. Support for BM was provided by the DFG priority program 1573 "The physics of the interstellar medium". AK acknowledges support by the Collaborative Research Council 956, sub-project A1, funded by the Deutsche Forschungsgemeinschaft (DFG). CMC acknowledges support from a McCue Fellowship through the University of California, Irvine's Center for Cosmology. VS is funded by the European Union's Seventh Framework program (grant agreement 337595). Based on data products from observations made with ESO Telescopes at the La Silla Paranal Observatory under ESO program ID 179.A-2005 and on data products produced by TERAPIX and the Cambridge Astronomy Survey Unit on behalf of the UltraVISTA consortium.

5

CONCLUSIONS AND OUTLOOK

5.1 CONCLUSIONS

In Chapters 2 and 3, we present measurements of the galaxy major and minor merger rate out to $z \sim 3$. We illustrate that the mass criterion for selecting galaxy pairs determines the merger fraction redshift evolution. Namely, defining mergers with stellar mass ratios leads to a diminishing redshift dependence, while defining with H-band flux ratios leads to an increasing trend. This selection effect explains the discrepant merger fraction measurements in literature (Bluck et al., 2009; Williams et al., 2010; Man et al., 2012; Newman et al., 2012). Furthermore, we infer the implications of the merger rates on the size and mass evolution of quiescent galaxies. Major merging alone can fully account for the stellar mass growth among the most massive galaxies, while galaxy mergers can only explain only half of the size evolution of quiescent galaxies at most. Therefore, additional mechanisms are required to fully explain the size growth of quiescent galaxies.

In Chapter 4, we constrained the average dust-obscured star formation rates in quiescent galaxies having very modest unobscured star formation. Obscured star formation rates are obtained through stacking the mid-, far-infrared and radio maps. Based on their low mid-infrared stacked flux densities, and non-detection in the far-infrared stacks, we confirm that quiescent galaxies do not host significant obscured star formation. This corroborates the need for powerful quenching mechanisms. The radio stacked emission exceeds the total (unobscured + obscured) star formation rates from other indicators, suggesting widespread active galactic nuclei among quiescent galaxies.

5.2 OUTLOOK

5.2.1 MERGER CONTRIBUTION TO THE COSMIC STAR FORMATION AT $z \sim 2$

In Chapters 2 and 3, we only focus on the stellar mass and size growth driven by galaxy mergers. The role of galaxy merging in the cosmic star formation rate density at $z \sim 2$ remains debated. In the local Universe, merging galaxies are the sites of the most intense starbursts and active black hole accretion (Kartaltepe et al., 2010; Patton et al., 2011; Treister et al., 2012). Do galaxies at $z \sim 2$ have enhanced star formation rates compared to isolated ones (Ellison et al., 2008; Patton et al., 2011; Scudder et al., 2012; Xu et al., 2012b; Yuan et al., 2012; Patton et al., 2013; Lackner et al., 2014), or are star-forming disks at $z \sim 2$ so gas-rich that the merger enhancement is incremental (e.g. Genzel et al., 2008; Shapiro et al., 2008; Förster Schreiber et al., 2009; Law et al., 2009; Kaviraj et al., 2013a,b; Kaviraj, 2014a,b)? To what extent does galaxy merging contribute to the peak of the cosmic star formation rate density at $z \sim 2$? Both obscured and unobscured star formation rates of merging galaxies should be studied to address this issue. In particular, in Chapter 3 we illustrate that gas-rich companions are missed, if galaxy mergers were selected by stellar mass ratio pairs. Therefore any conclusion based on such selections would lead to an underestimation of the merger contribution to the cosmic star formation. Developing better definitions of galaxy mergers that accounts for both the stellar and gaseous mass is the subject of future work.

5.2.2 GALAXY ENVIRONMENTAL DEPENDENCE

Do galaxy mergers in cluster environments have higher relative velocities, therefore take longer to coalesce? The environmental dependence is not currently accounted for in merger rate calculations, since the merging timescale depends on many variables, including orbital parameters, mass ratio, etc. Should the timescale depend on local density, it would vary with redshift and may have implications of the merger rate evolution. The environment effect is expected to be more notable at later epochs, since large-scale structures are more prominent. Additionally, in cluster environments galaxies can interact and exchange mass with each other during fly-by's, yet the cores do not coalesce. Such effects may lead to the growth of the stellar mass and sizes of galaxies similar to mergers, as well as triggering of starburst / active black hole episodes, but are largely overlooked in current studies. Analyzing the fly-by effects and merging timescales in a cosmological setting is required to make advancement in these aspects.

5.2.3 FEEDBACK FROM ACTIVE GALACTIC NUCLEI

The stacking analysis at radio (Chapter 4) and X-ray (Olsen et al., 2013) wavelengths indicates a widespread presence of active galactic nuclei among massive quiescent

galaxies. While active galactic nuclei feedback represents the most convenient explanation for terminating and suppressing star formation in galaxies, better observations are needed to constrain the exact physics involved. Do active galactic nuclei operate on a duty cycle, fluctuating between radiative efficient mode (X-ray) and inefficient mode (radio jet) while it exchanges energy with the circumgalactic gas? It is challenging to convert average luminosities into mechanical or radiative power injected by the active galactic nuclei into the circumgalactic gas, as it involves assumption of the duty cycle. Future deep surveys with new instruments like *NuSTAR*, the Jansky Very Large Array, the Square Kilometer Array and the Low-Frequency Array will be more sensitive to detect fainter active galactic nuclei. This will shed light towards the more representative population, and direct detections will constrain the feedback cycle through energetic arguments. The coevolution of active black holes and quiescent galaxies will hopefully be better understood.

5.2.4 Dust modeling in quiescent galaxies

As illustrated in Chapter 4, quiescent galaxies at $z = 0.5 - 1.5$ appear to have 24μm emission in excess of the expectation from pure stellar emission models, as well as the dust-obscured star formation rate upper limits. The former results are confirmed by two other 24μm stacking investigations (Fumagalli et al., 2013; Utomo et al., 2014).

In standard stellar population synthesis (e.g. Bruzual & Charlot, 2003), a dust attenuation law (e.g. Calzetti et al., 2000) is applied to stellar emission models, without considering for the dust re-emission at mid- and far-infrared wavelengths. While this is not an issue for analysis of optical-to-near-infrared observations, which is still dominated by stellar emission, self-consistent dust modeling should be used for observations spanning from ultraviolet to far-infrared (e.g. da Cunha et al., 2008; Utomo et al., 2014).

Additionally, caution must be taken when inferring the origin of dust heating in quiescent galaxies. In the absence of recent star formation and obscured active galactic nuclei, various mechanisms could contribute to the infrared luminosity of evolved stellar populations, as observed in nearby ellipticals. For instance, circumstellar dust around asymptotic giant branch stars can contribute to the mid-infrared emission (Knapp et al., 1992; Piovan et al., 2003), yet it remains a main source of uncertainty in current stellar population models. On the other hand, diffuse interstellar (cirrus) dust heated by evolved stellar populations has been observed to peak at longer wavelengths at rest-frame $100 - 300\mu$m (Bendo et al., 2012). Additionally, polycyclic aromatic hydrocarbon (PAH) molecular emission peaking at at rest-frame $5 - 20\mu$m (Bendo et al., 2008; Kennicutt & Evans, 2012) is shown to correlate with both circumstellar and interstellar dust. To mitigate the effects of mid-infrared flux boosted by PAH emissions and/or obscured active galactic nuclei, far-infrared observations are preferable for deriving the dust re-emission. To discern the contributions of young and evolved stellar populations to

heating dust in quiescent galaxies, theoretical studies are needed to reduce the large parameter space (e.g. dust grain models, interstellar radiation fields, infrared luminosity, stellar ages), in order to predict the observables required to constrain such models.

A

LIST OF PUBLICATIONS

A.1 REFEREED PUBLICATIONS

Number of first author papers: 1 published + 2 submitted
Number of refereed papers: 9

1. **Man, A. W. S.**; Greve, T.; Toft, S.; Magnelli, B.; Karim, A.; Ilbert, O.; Salvato, M.; Le Floc'h, E.; Bertoldi, F.; Casey, C.; Lee, N.; Li, Y.; Navarrete, F.; Sheth, K.; Smolčić, V.; Sanders, D.; Schinnerer, E. & Zirm, A., 2014,
   Submitted to the *Astrophysical Journal Letters*, arXiv: 1411.2870, 7 pages
   "Confirming the Quiescent Galaxy Population out to $z = 3$: A Stacking Analysis of Mid-, Far-Infrared and Radio Data"

2. **Man, A. W. S.**; Toft, S. & Zirm, A., 2014,
   Submitted to the *Astrophysical Journal*, positive referee report received, arXiv: 1410.3479, 25 pages
   "Explaining the Discrepancy of Galaxy Merger Fraction Measurements at $z \sim 0 - 3$"

3. Krogager, J.-K.; Zirm, A.; Toft, S.; **Man, A. W. S.** & Brammer, G., 2014,
   Accepted for publication in the *Astrophysical Journal*, arXiv:1309.6316, 16 pages
   "A Spectroscopic Sample of Massive, Evolved $z \sim 2$ Galaxies: Implications for the Evolution of the Mass-Size Relation"

4. Toft, S.; Smolčić, V.; Magnelli, B.; Karim, A.; Zirm, A.; Michalowski, M.; Capak, P.; Sheth, K.; Schawinski, K.; Krogager, J.-K.; Wuyts, S.; Sanders, D.; **Man, A. W. S.**; Lutz, D.; Staguhn, J.; Berta, S.; McCracken, H.; Krpan, J. & Riechers, D., 2014,
   Astrophysical Journal, 782, 68, Published 29 January 2014, 12 pages
   "Submillimeter Galaxies as Progenitors of Compact Quiescent Galaxies"

5. Koss, M.; Blecha, L.; Mushotzky, R.; Hung, C. L.; Veilleux, S.; Trakhtenbrot, B.; Schawinski, K.; Stern, D.; Smith, N.; Li Y.; **Man, A. W. S.**, Filippenko, A.; Mauerhan,

J.; Stanek, K. & Sanders, D., 2014, *Monthly Notices of the Royal Astronomical Society*, 445, 515, Published 29 September 2014, 13 pages
"SDSS1133: An Unusually Persistent Transient in a Nearby Dwarf Galaxy"

6. Hung, C.-L.; Sanders, D. B.; Casey, C. M.; Lee, N.; Barnes, J. E.; Capak, P.; Kartaltepe, J. S.; Koss, M.; Larson, K. L.; Le Floc'h, E.; Lockhart, K.; **Man, A. W. S.**; Mann, A. W.; Riguccini, L.; Scoville, N. & Symeonidis, M., 2013, *Astrophysical Journal*, 778, 129, Published 12 November 2013, 13 pages
"The Role of Galaxy Interaction in the SFR-$M_\star$ Relation: Characterizing Morphological Properties of *Herschel*-selected Galaxies at $0 < z < 1.5$"

7. Geier, S; Richard, J.; **Man, A. W. S.**; Krühler, T.; Toft, S.; Marchesini, D. & Fynbo, J., 2013, *Astrophysical Journal*, 77, 87, Published 17 October 2013, 13 pages
"Near-Infrared Spectroscopy and Imaging of Gravitationally-Lensed $z \sim 2$ Compact Quiescent Galaxies"

8. Toft, S.; Gallazzi, A.; Zirm, A.; Wold, M.; Zibetti, S.; Grillo, C. & **Man, A. W. S.**, 2012, *Astrophysical Journal*, 754, 3, Published 27 June 2012, 18 pages
"Deep Absorption Line Studies of Quiescent Galaxies at $z \sim 2$: The Dynamical-Mass-Size Relation and First Constraints on the Fundamental Plane"

9. **Man, A. W. S.**; Toft, S.; Zirm, A.; Wuyts, S. & van der Wel, A., 2012, *Astrophysical Journal*, 744, 85, Published 16 December 2011, 7 pages
"Pair Fraction of Massive Galaxies at $0 \leq z \leq 3$"

A.2 OTHER PUBLICATIONS

Summary: 3 conference posters, 2 circulars, 1 conference proceedings paper

1. **Man, A. W. S.**; Zirm, A., & Toft, S., 2014
"Explaining the Discrepancy of Galaxy Merger Fraction Measurements at $z \sim 0 - 3$"
Poster for the IAU Symposium 311 on Galaxy Masses

2. **Man, A. W. S.**; Toft, S. & Zirm, A., 2011
"Galaxy Pairs as a Probe for Mergers at $z \sim 2$"
Conference Proceedings for GMiEU conference, 4 pages

3. **Man, A. W. S.**; Toft, S.; Zirm, A.; Wuyts, S. & van der Wel, A., 2011
"Can Major Merging Account for the Size Evolution? The Pair Fraction of Massive Galaxies at $0 < z < 3$"
Poster for the IAC Winter School on Secular Evolution of Galaxies

4. de Ugarte Postigo, A.; Fynbo, J. P. U.; Leloudas, G.; Geier, S.; **Man, A. W. S.**; Jakobsson, P., 2011
   "OT 110215: further NIR observations from NOT of the GRB candidate"
   GBR Coordinates Network, Circular Service, 11750, 1

5. de Ugarte Postigo, A.; Fynbo, J. P. U.; Leloudas, G.; Geier, S.; **Man, A. W. S.**; Jakobsson, P., 2011
   "OT 110215: NIR observations from NOT of GRB candidate"
   GBR Coordinates Network, Circular Service, 11745, 1

6. **Man, A. W. S.**; Toft, S. & Zirm, A., 2010
   "The compactness of massive, quiescent $z \sim 2$ galaxies in COSMOS field"
   Poster for the conference on the Formation and Evolution of Blackholes, Galaxies and their Environment

BIBLIOGRAPHY

Arnouts, S., et al. 2013, A&A, 558, A67

Ashby, M. L. N., et al. 2013, ApJ, 769, 80

Barmby, P., Huang, J.-S., Ashby, M. L. N., Eisenhardt, P. R. M., Fazio, G. G., Willner, S. P., & Wright, E. L. 2008, ApJS, 177, 431

Barnes, J. E. 1990, Nature, 344, 379

Barnes, J. E., & Hernquist, L. 1996, ApJ, 471, 115

Barnes, J. E., & Hernquist, L. E. 1991, ApJ, 370, L65

Barro, G., et al. 2014, ApJ, 791, 52

Behroozi, P. S., Marchesini, D., Wechsler, R. H., Muzzin, A., Papovich, C., & Stefanon, M. 2013, ApJ, 777, L10

Bell, E. F. 2003, ApJ, 586, 794

Bell, E. F., Phleps, S., Somerville, R. S., Wolf, C., Borch, A., & Meisenheimer, K. 2006a, ApJ, 652, 270

Bell, E. F., et al. 2004, ApJ, 608, 752

—. 2006b, ApJ, 640, 241

Belli, S., Newman, A. B., & Ellis, R. S. 2014a, ApJ, 783, 117

Belli, S., Newman, A. B., Ellis, R. S., & Konidaris, N. P. 2014b, ApJ, 788, L29

Bendo, G. J., et al. 2008, MNRAS, 389, 629

—. 2012, MNRAS, 419, 1833

Bernardi, M., Shankar, F., Hyde, J. B., Mei, S., Marulli, F., & Sheth, R. K. 2010, MNRAS, 404, 2087

Berrier, J. C., Bullock, J. S., Barton, E. J., Guenther, H. D., Zentner, A. R., & Wechsler, R. H. 2006, ApJ, 652, 56

Bertin, E., & Arnouts, S. 1996, A&AS, 117, 393

Bertone, S., & Conselice, C. J. 2009, MNRAS, 396, 2345

Best, P. N., & Heckman, T. M. 2012, MNRAS, 421, 1569

Béthermin, M., Dole, H., Beelen, A., & Aussel, H. 2010, A&A, 512, A78

Bezanson, R., van Dokkum, P., & Franx, M. 2012, ApJ, 760, 62

Bezanson, R., van Dokkum, P. G., Tal, T., Marchesini, D., Kriek, M., Franx, M., & Coppi, P. 2009, ApJ, 697, 1290

Bezanson, R., van Dokkum, P. G., van de Sande, J., Franx, M., Leja, J., & Kriek, M. 2013, ApJ, 779, L21

Bielby, R., et al. 2012, A&A, 545, A23

Bluck, A. F. L., Conselice, C. J., Bouwens, R. J., Daddi, E., Dickinson, M., Papovich, C., & Yan, H. 2009, MNRAS, 394, L51

Bluck, A. F. L., Conselice, C. J., Buitrago, F., Grützbauch, R., Hoyos, C., Mortlock, A., & Bauer, A. E. 2012, ApJ, 747, 34

Bothwell, M. S., et al. 2013, MNRAS, 429, 3047

Bower, R. G., Benson, A. J., Malbon, R., Helly, J. C., Frenk, C. S., Baugh, C. M., Cole, S., & Lacey, C. G. 2006, MNRAS, 370, 645

Boylan-Kolchin, M., Ma, C.-P., & Quataert, E. 2008, MNRAS, 383, 93

Brammer, G. B., van Dokkum, P. G., & Coppi, P. 2008, ApJ, 686, 1503

Brammer, G. B., et al. 2011, ApJ, 739, 24

—. 2012, ApJS, 200, 13

Bruce, V. A., et al. 2014, MNRAS, 444, 1660

Brusa, M., et al. 2010, ApJ, 716, 348

Bruzual, G., & Charlot, S. 2003, MNRAS, 344, 1000

Buitrago, F., Trujillo, I., Conselice, C. J., Bouwens, R. J., Dickinson, M., & Yan, H. 2008, ApJ, 687, L61

Bundy, K., Fukugita, M., Ellis, R. S., Kodama, T., & Conselice, C. J. 2004, ApJ, 601, L123

Bundy, K., Fukugita, M., Ellis, R. S., Targett, T. A., Belli, S., & Kodama, T. 2009, ApJ, 697, 1369

Calzetti, D., Armus, L., Bohlin, R. C., Kinney, A. L., Koornneef, J., & Storchi-Bergmann, T. 2000, ApJ, 533, 682

Cameron, E., & Pettitt, A. N. 2012, MNRAS, 425, 44

Capak, P., et al. 2004, AJ, 127, 180

—. 2007, ApJS, 172, 99

Cardamone, C. N., et al. 2010, ApJS, 189, 270

Carlberg, R. G., Pritchet, C. J., & Infante, L. 1994, ApJ, 435, 540

Carollo, C. M., et al. 2013, ApJ, 773, 112

Casey, C. M. 2012, MNRAS, 425, 3094

Cassata, P., et al. 2010, ApJ, 714, L79

—. 2013, ApJ, 775, 106

Cattaneo, A., Mamon, G. A., Warnick, K., & Knebe, A. 2011, A&A, 533, A5

Chabrier, G. 2003, PASP, 115, 763

Chang, Y.-Y., et al. 2013, ApJ, 773, 149
Cimatti, A., et al. 2008, A&A, 482, 21
—. 2013, ApJ, 779, L13
Civano, F., et al. 2012, ApJS, 201, 30
Conselice, C. J., Bershady, M. A., Dickinson, M., & Papovich, C. 2003, AJ, 126, 1183
Conselice, C. J., Mortlock, A., Bluck, A. F. L., Grützbauch, R., & Duncan, K. 2013, MNRAS, 430, 1051
Conselice, C. J., et al. 2007, MNRAS, 381, 962
—. 2011, MNRAS, 226
Cox, T. J., Jonsson, P., Somerville, R. S., Primack, J. R., & Dekel, A. 2008, MNRAS, 384, 386
Croton, D. J., et al. 2006, MNRAS, 365, 11
da Cunha, E., Charlot, S., & Elbaz, D. 2008, MNRAS, 388, 1595
Daddi, E., et al. 2003, ApJ, 588, 50
—. 2005, ApJ, 626, 680
—. 2007, ApJ, 670, 173
—. 2010, ApJ, 713, 686
Damjanov, I., et al. 2009, ApJ, 695, 101
De Propris, R., Conselice, C. J., Liske, J., Driver, S. P., Patton, D. R., Graham, A. W., & Allen, P. D. 2007, ApJ, 666, 212
de Ravel, L., et al. 2009, A&A, 498, 379
—. 2011, A&A, submitted, arXiv:1104.5470
Dekel, A., Sari, R., & Ceverino, D. 2009, ApJ, 703, 785
Di Matteo, T., Springel, V., & Hernquist, L. 2005, Nature, 433, 604
Dickinson, M., Giavalisco, M., & GOODS Team. 2003, in The Mass of Galaxies at Low and High Redshift, ed. R. Bender & A. Renzini, 324
Donley, J. L., et al. 2012, ApJ, 748, 142
Drory, N., & Alvarez, M. 2008, ApJ, 680, 41
Ellison, S. L., Mendel, J. T., Scudder, J. M., Patton, D. R., & Palmer, M. J. D. 2013, MNRAS, 430, 3128
Ellison, S. L., Patton, D. R., Simard, L., & McConnachie, A. W. 2008, AJ, 135, 1877
Erb, D. K., Steidel, C. C., Shapley, A. E., Pettini, M., Reddy, N. A., & Adelberger, K. L. 2006, ApJ, 646, 107
Erben, T., et al. 2005, Astronomische Nachrichten, 326, 432
—. 2009, A&A, 493, 1197
Fakhouri, O., & Ma, C. 2008, MNRAS, 386, 577
Fan, L., Lapi, A., Bressan, A., Bernardi, M., De Zotti, G., & Danese, L. 2010, ApJ, 718,

1460
Fan, L., Lapi, A., De Zotti, G., & Danese, L. 2008, ApJ, 689, L101
Ferreras, I., et al. 2013, MNRAS, submitted, arXiv:1312.5317
Förster Schreiber, N. M., Shapley, A. E., Erb, D. K., Genzel, R., Steidel, C. C., Bouché, N., Cresci, G., & Davies, R. 2011, ApJ, 731, 65
Förster Schreiber, N. M., et al. 2009, ApJ, 706, 1364
Franx, M., van Dokkum, P. G., Schreiber, N. M. F., Wuyts, S., Labbé, I., & Toft, S. 2008, ApJ, 688, 770
Franx, M., et al. 2003, ApJ, 587, L79
Fumagalli, M., et al. 2013, ArXiv e-prints
Furusawa, H., Kosugi, G., Akiyama, M., Takata, T., Sekiguchi, K., & Furusawa, J. 2008, in Astronomical Society of the Pacific Conference Series, Vol. 399, Panoramic Views of Galaxy Formation and Evolution, ed. T. Kodama, T. Yamada, & K. Aoki, 131
Gabasch, A., Goranova, Y., Hopp, U., Noll, S., & Pannella, M. 2008, MNRAS, 383, 1319
Gabor, J. M., & Davé, R. 2012, MNRAS, 427, 1816
Gallazzi, A., Bell, E. F., Zibetti, S., Brinchmann, J., & Kelson, D. D. 2014, ApJ, 788, 72
Gargiulo, A., Saracco, P., Longhetti, M., La Barbera, F., & Tamburri, S. 2012, MNRAS, 425, 2698
Genzel, R., et al. 2008, ApJ, 687, 59
Giavalisco, M., et al. 2004, ApJ, 600, L93
Griffin, M. J., et al. 2010, A&A, 518, L3
Grogin, N. A., et al. 2011, ArXiv e-prints
Guo, Y., et al. 2011, ApJ, 735, 18
—. 2013, ApJS, 207, 24
Hayward, C. C., et al. 2014, MNRAS, 445, 1598
Heiderman, A., et al. 2009, ApJ, 705, 1433
Hildebrandt, H., Pielorz, J., Erben, T., van Waerbeke, L., Simon, P., & Capak, P. 2009, A&A, 498, 725
Hildebrandt, H., et al. 2006, A&A, 452, 1121
Hilz, M., Naab, T., & Ostriker, J. P. 2013, MNRAS, 535
Hilz, M., Naab, T., Ostriker, J. P., Thomas, J., Burkert, A., & Jesseit, R. 2012, MNRAS, 425, 3119
Hopkins, A. M., & Beacom, J. F. 2006, ApJ, 651, 142
Hopkins, P. F., Bundy, K., Hernquist, L., Wuyts, S., & Cox, T. J. 2010a, MNRAS, 401, 1099
Hopkins, P. F., Cox, T. J., Younger, J. D., & Hernquist, L. 2009a, ApJ, 691, 1168
Hopkins, P. F., et al. 2009b, MNRAS, 397, 802

—. 2010b, ApJ, 715, 202
—. 2010c, ApJ, 715, 202
—. 2010d, ApJ, 724, 915
Hsieh, B.-C., Wang, W.-H., Hsieh, C.-C., Lin, L., Yan, H., Lim, J., & Ho, P. T. P. 2012, ApJS, 203, 23
Hung, C.-L., et al. 2013, ApJ, 778, 129
Ilbert, O., et al. 2009, ApJ, 690, 1236
—. 2010, ApJ, 709, 644
—. 2013, A&A, 556, A55
Ivison, R. J., et al. 2010, A&A, 518, L31
Jiang, C. Y., Jing, Y. P., Faltenbacher, A., Lin, W. P., & Li, C. 2008, ApJ, 675, 1095
Jogee, S., et al. 2009, ApJ, 697, 1971
Kajisawa, M., et al. 2011, PASJ, 63, 379
Kartaltepe, J. S., et al. 2007, ApJS, 172, 320
—. 2010, ApJ, 721, 98
—. 2012, ApJ, 757, 23
Kauffmann, G., & White, S. D. M. 1993, MNRAS, 261, 921
Kaviraj, S. 2014a, MNRAS, 440, 2944
—. 2014b, MNRAS, 437, L41
Kaviraj, S., et al. 2013a, MNRAS, 428, 925
—. 2013b, MNRAS, 429, L40
Kennicutt, R. C., & Evans, N. J. 2012, ARA&A, 50, 531
Kennicutt, Jr., R. C. 1998, ARA&A, 36, 189
Khochfar, S., & Silk, J. 2006, ApJ, 648, L21
Kitzbichler, M. G., & White, S. D. M. 2008, MNRAS, 391, 1489
Knapp, G. R., Gunn, J. E., & Wynn-Williams, C. G. 1992, ApJ, 399, 76
Koekemoer, A. M., et al. 2011, ArXiv e-prints
Kriek, M., van der Wel, A., van Dokkum, P. G., Franx, M., & Illingworth, G. D. 2008, ApJ, 682, 896
Kriek, M., van Dokkum, P. G., Franx, M., Illingworth, G. D., & Magee, D. K. 2009a, ApJ, 705, L71
Kriek, M., van Dokkum, P. G., Labbé, I., Franx, M., Illingworth, G. D., Marchesini, D., & Quadri, R. F. 2009b, ApJ, 700, 221
—. 2009c, ApJ, 700, 221
Kriek, M., et al. 2006a, ApJ, 645, 44
—. 2006b, ApJ, 649, L71
Krogager, J.-K., Zirm, A. W., Toft, S., Man, A., & Brammer, G. 2013, ApJ, submitted,

arXiv:1309.6316
Kurczynski, P., & Gawiser, E. 2010, AJ, 139, 1592
Lackner, C. N., Cen, R., Ostriker, J. P., & Joung, M. R. 2012, MNRAS, 425, 641
Lackner, C. N., et al. 2014, AJ, submitted, arXiv:1406.2327
Lanz, L., et al. 2013, ApJ, 768, 90
Laporte, C. F. P., White, S. D. M., Naab, T., & Gao, L. 2013, MNRAS, 435, 901
Law, D. R., Steidel, C. C., Erb, D. K., Larkin, J. E., Pettini, M., Shapley, A. E., & Wright, S. A. 2009, ApJ, 697, 2057
Law, D. R., Steidel, C. C., Shapley, A. E., Nagy, S. R., Reddy, N. A., & Erb, D. K. 2011, ArXiv e-prints
Le Fèvre, O., et al. 2000, MNRAS, 311, 565
Le Floc'h, E., et al. 2009, ApJ, 703, 222
Lee, N., et al. 2013, ApJ, 778, 131
Leja, J., van Dokkum, P., & Franx, M. 2013, ApJ, 766, 33
Lemaux, B. C., et al. 2013, ArXiv e-prints
Lidman, C., et al. 2013, MNRAS, 433, 825
Lilly, S. J., Le Fevre, O., Hammer, F., & Crampton, D. 1996, ApJ, 460, L1
Lilly, S. J., et al. 2007, ApJS, 172, 70
Lin, L., et al. 2004, ApJ, 617, L9
—. 2008, ApJ, 681, 232
López-Sanjuan, C., Balcells, M., Pérez-González, P. G., Barro, G., Gallego, J., & Zamorano, J. 2010, A&A, 518, A20
López-Sanjuan, C., Balcells, M., Pérez-González, P. G., Barro, G., García-Dabó, C. E., Gallego, J., & Zamorano, J. 2009, A&A, 501, 505
López-Sanjuan, C., et al. 2011, A&A, 530, A20
—. 2012, A&A, 548, A7
—. 2013, A&A, 553, A78
—. 2014, A&A, 564, A127
Lotz, J. M., Jonsson, P., Cox, T. J., Croton, D., Primack, J. R., Somerville, R. S., & Stewart, K. 2011, ApJ, 742, 103
Lotz, J. M., Jonsson, P., Cox, T. J., & Primack, J. R. 2008a, MNRAS, 391, 1137
—. 2010, MNRAS, 404, 575
Lotz, J. M., et al. 2008b, ApJ, 672, 177
—. 2008c, ApJ, 672, 177
Lutz, D., et al. 2011, A&A, 532, A90
Madau, P., & Dickinson, M. 2014, ARA&A, accepted, arXiv:1403.0007
Madau, P., Ferguson, H. C., Dickinson, M. E., Giavalisco, M., Steidel, C. C., & Fruchter,

A. 1996, MNRAS, 283, 1388
Maller, A. H., Katz, N., Kereš, D., Davé, R., & Weinberg, D. H. 2006, ApJ, 647, 763
Man, A. W. S., Toft, S., Zirm, A. W., Wuyts, S., & van der Wel, A. 2012, ApJ, 744, 85
Man, A. W. S., Zirm, A. W., & Toft, S. 2014, ArXiv e-prints
Mannucci, F., et al. 2009, MNRAS, 398, 1915
Marchesini, D., van Dokkum, P. G., Förster Schreiber, N. M., Franx, M., Labbé, I., & Wuyts, S. 2009, ApJ, 701, 1765
Marsden, G., et al. 2009, ApJ, 707, 1729
Martin, D. C., et al. 2005, ApJ, 619, L1
McCavana, T., Micic, M., Lewis, G. F., Sinha, M., Sharma, S., Holley-Bockelmann, K., & Bland-Hawthorn, J. 2012, MNRAS, 424, 361
McCracken, H. J., et al. 2012, A&A, 544, A156
McIntosh, D. H., Guo, Y., Hertzberg, J., Katz, N., Mo, H. J., van den Bosch, F. C., & Yang, X. 2008, MNRAS, 388, 1537
Mihos, J. C., & Hernquist, L. 1994, ApJ, 431, L9
—. 1996, ApJ, 464, 641
Moreno, J. 2012, MNRAS, 419, 411
Moreno, J., Bluck, A. F. L., Ellison, S. L., Patton, D. R., Torrey, P., & Moster, B. P. 2013, MNRAS, 436, 1765
Moster, B. P., Somerville, R. S., Newman, J. A., & Rix, H.-W. 2011, ApJ, 731, 113
Muzzin, A., et al. 2013, ApJS, 206, 8
Naab, T., Jesseit, R., & Burkert, A. 2006, MNRAS, 372, 839
Naab, T., Johansson, P. H., & Ostriker, J. P. 2009, ApJ, 699, L178
Naab, T., Johansson, P. H., Ostriker, J. P., & Efstathiou, G. 2007, ApJ, 658, 710
Newman, A. B., Ellis, R. S., Bundy, K., & Treu, T. 2012, ApJ, 746, 162
Nipoti, C., Treu, T., Auger, M. W., & Bolton, A. S. 2009, ApJ, 706, L86
Nonino, M., et al. 2009, ApJS, 183, 244
Oliver, S. J., et al. 2012, MNRAS, 424, 1614
Olsen, K. P., Rasmussen, J., Toft, S., & Zirm, A. W. 2013, ApJ, 764, 4
Onodera, M., et al. 2010, ApJ, 715, L6
Oser, L., Naab, T., Ostriker, J. P., & Johansson, P. H. 2012, ApJ, 744, 63
Oser, L., Ostriker, J. P., Naab, T., Johansson, P. H., & Burkert, A. 2010, ApJ, 725, 2312
Patton, D. R., & Atfield, J. E. 2008, ApJ, 685, 235
Patton, D. R., Carlberg, R. G., Marzke, R. O., Pritchet, C. J., da Costa, L. N., & Pellegrini, P. S. 2000, ApJ, 536, 153
Patton, D. R., Ellison, S. L., Simard, L., McConnachie, A. W., & Mendel, J. T. 2011, MNRAS, 412, 591

Patton, D. R., Torrey, P., Ellison, S. L., Mendel, J. T., & Scudder, J. M. 2013, MNRAS, 433, L59

Peebles, P. J. E. 1993, Principles of Physical Cosmology

Peng, Y.-j., et al. 2010, ApJ, 721, 193

Piovan, L., Tantalo, R., & Chiosi, C. 2003, A&A, 408, 559

Poggianti, B. M., et al. 2013, ApJ, 762, 77

Poglitsch, A., et al. 2010, A&A, 518, L2

Posti, L., Nipoti, C., Stiavelli, M., & Ciotti, L. 2014, MNRAS, 440, 610

Puech, M., Hammer, F., Hopkins, P. F., Athanassoula, E., Flores, H., Rodrigues, M., Wang, J. L., & Yang, Y. B. 2012, ApJ, 753, 128

Puech, M., Hammer, F., Rodrigues, M., Fouquet, S., Flores, H., & Disseau, K. 2014, MNRAS, 443, L49

Rawat, A., Hammer, F., Kembhavi, A. K., & Flores, H. 2008, ApJ, 681, 1089

Retzlaff, J., Rosati, P., Dickinson, M., Vandame, B., Rité, C., Nonino, M., Cesarsky, C., & GOODS Team. 2010, A&A, 511, A50

Robaina, A. R., Bell, E. F., van der Wel, A., Somerville, R. S., Skelton, R. E., McIntosh, D. H., Meisenheimer, K., & Wolf, C. 2010, ApJ, 719, 844

Robaina, A. R., et al. 2009, ApJ, 704, 324

Robertson, B., Cox, T. J., Hernquist, L., Franx, M., Hopkins, P. F., Martini, P., & Springel, V. 2006, ApJ, 641, 21

Rujopakarn, W., Rieke, G. H., Weiner, B. J., Pérez-González, P., Rex, M., Walth, G. L., & Kartaltepe, J. S. 2013, ApJ, 767, 73

Ryan, Jr., R. E., Cohen, S. H., Windhorst, R. A., & Silk, J. 2008, ApJ, 678, 751

Salim, S., et al. 2009, ApJ, 700, 161

Sanders, D. B., et al. 2007, ApJS, 172, 86

Schawinski, K., Virani, S., Simmons, B., Urry, C. M., Treister, E., Kaviraj, S., & Kushkuley, B. 2009a, ApJ, 692, L19

Schawinski, K., et al. 2009b, ApJ, 690, 1672

Schinnerer, E., et al. 2007, ApJS, 172, 46

—. 2010, ApJS, 188, 384

Scoville, N., et al. 2007a, ApJS, 172, 1

—. 2007b, ApJS, 172, 1

—. 2014, ApJ, 783, 84

Scudder, J. M., Ellison, S. L., Torrey, P., Patton, D. R., & Mendel, J. T. 2012, MNRAS, 426, 549

Shankar, F., & Bernardi, M. 2009, MNRAS, 396, L76

Shapiro, K. L., et al. 2008, ApJ, 682, 231

Shih, H.-Y., & Stockton, A. 2011, ApJ, 733, 45

Silverman, J. D., et al. 2011, ApJ, 743, 2
Sinha, M., & Holley-Bockelmann, K. 2012, ApJ, 751, 17
Skelton, R. E., et al. 2014, ApJS, 214, 24
Smolčić, V., et al. 2009, ApJ, 696, 24
Somerville, R. S., Hopkins, P. F., Cox, T. J., Robertson, B. E., & Hernquist, L. 2008, MNRAS, 391, 481
Somerville, R. S., Lee, K., Ferguson, H. C., Gardner, J. P., Moustakas, L. A., & Giavalisco, M. 2004, ApJ, 600, L171
Sommer-Larsen, J., & Toft, S. 2010, ApJ, 721, 1755
Speagle, J. S., Steinhardt, C. L., Capak, P. L., & Silverman, J. D. 2014, ApJS, 214, 15
Springel, V., et al. 2005, Nature, 435, 629
Steidel, C. C., Adelberger, K. L., Shapley, A. E., Pettini, M., Dickinson, M., & Giavalisco, M. 2003, ApJ, 592, 728
Stewart, K. R., Bullock, J. S., Barton, E. J., & Wechsler, R. H. 2009a, ApJ, 702, 1005
Stewart, K. R., Bullock, J. S., Wechsler, R. H., & Maller, A. H. 2009b, ApJ, 702, 307
Szomoru, D., Franx, M., Bouwens, R. J., van Dokkum, P. G., Labbé, I., Illingworth, G. D., & Trenti, M. 2011, ApJ, 735, L22
Szomoru, D., Franx, M., & van Dokkum, P. G. 2012, ApJ, 749, 121
Szomoru, D., Franx, M., van Dokkum, P. G., Trenti, M., Illingworth, G. D., Labbé, I., & Oesch, P. 2013, ApJ, 763, 73
Szomoru, D., et al. 2010, ApJ, 714, L244
Tacconi, L. J., et al. 2010, Nature, 463, 781
—. 2013, ApJ, 768, 74
Tadaki, K.-i., et al. 2014, ApJ, 788, L23
Taniguchi, Y., et al. 2007, ApJS, 172, 9
Targett, T. A., Dunlop, J. S., McLure, R. J., Best, P. N., Cirasuolo, M., & Almaini, O. 2011, MNRAS, 412, 295
Tasca, L. A. M., et al. 2014, A&A, 565, A10
Taylor, E. N., et al. 2009, ApJS, 183, 295
Toft, S., Franx, M., van Dokkum, P., Förster Schreiber, N. M., Labbe, I., Wuyts, S., & Marchesini, D. 2009, ApJ, 705, 255
Toft, S., Gallazzi, A., Zirm, A., Wold, M., Zibetti, S., Grillo, C., & Man, A. 2012, ApJ, 754, 3
Toft, S., van Dokkum, P., Franx, M., Thompson, R. I., Illingworth, G. D., Bouwens, R. J., & Kriek, M. 2005, ApJ, 624, L9
Toft, S., et al. 2007, ApJ, 671, 285
—. 2014, ApJ, 782, 68
Toomre, A., & Toomre, J. 1972, ApJ, 178, 623

Torrey, P., Cox, T. J., Kewley, L., & Hernquist, L. 2012, ApJ, 746, 108

Treister, E., Natarajan, P., Sanders, D. B., Urry, C. M., Schawinski, K., & Kartaltepe, J. 2010, Science, 328, 600

Treister, E., Schawinski, K., Urry, C. M., & Simmons, B. D. 2012, ApJ, 758, L39

Tremonti, C. A., Moustakas, J., & Diamond-Stanic, A. M. 2007, ApJ, 663, L77

Trujillo, I., Cenarro, A. J., de Lorenzo-Cáceres, A., Vazdekis, A., de la Rosa, I. G., & Cava, A. 2009, ApJ, 692, L118

Trujillo, I., Conselice, C. J., Bundy, K., Cooper, M. C., Eisenhardt, P., & Ellis, R. S. 2007, MNRAS, 382, 109

Trujillo, I., Ferreras, I., & de La Rosa, I. G. 2011, MNRAS, 415, 3903

Trujillo, I., et al. 2006a, MNRAS, 373, L36

—. 2006b, ApJ, 650, 18

Utomo, D., Kriek, M., Labbé, I., Conroy, C., & Fumagalli, M. 2014, ApJ, 783, L30

van de Sande, J., et al. 2011, ApJ, 736, L9

—. 2013, ApJ, 771, 85

van der Wel, A., Bell, E. F., van den Bosch, F. C., Gallazzi, A., & Rix, H.-W. 2009a, ApJ, 698, 1232

van der Wel, A., Rix, H.-W., Holden, B. P., Bell, E. F., & Robaina, A. R. 2009b, ApJ, 706, L120

van der Wel, A., et al. 2011, ApJ, 730, 38

—. 2014, ApJ, 788, 28

van Dokkum, P., et al. 2014, ApJ, submitted, arXiv:1404.4874

van Dokkum, P. G. 2005, AJ, 130, 2647

van Dokkum, P. G., Kriek, M., & Franx, M. 2009, Nature, 460, 717

van Dokkum, P. G., et al. 2003, ApJ, 587, L83

—. 2008, ApJ, 677, L5

—. 2010, ApJ, 709, 1018

—. 2011, ArXiv e-prints

Viero, M. P., et al. 2013, ApJ, 779, 32

Whitaker, K. E., Kriek, M., van Dokkum, P. G., Bezanson, R., Brammer, G., Franx, M., & Labbé, I. 2012, ApJ, 745, 179

Whitaker, K. E., et al. 2010, ApJ, 719, 1715

—. 2011, ApJ, 735, 86

White, S. D. M., & Frenk, C. S. 1991, ApJ, 379, 52

Williams, R. J., Quadri, R. F., & Franx, M. 2011, ApJ, 738, L25

Williams, R. J., Quadri, R. F., Franx, M., van Dokkum, P., & Labbé, I. 2009, ApJ, 691, 1879

Williams, R. J., Quadri, R. F., Franx, M., van Dokkum, P., Toft, S., Kriek, M., & Labbé, I. 2010, ApJ, 713, 738

Wuyts, S., Cox, T. J., Hayward, C. C., Franx, M., Hernquist, L., Hopkins, P. F., Jonsson, P., & van Dokkum, P. G. 2010, ApJ, 722, 1666

Wuyts, S., Labbé, I., Schreiber, N. M. F., Franx, M., Rudnick, G., Brammer, G. B., & van Dokkum, P. G. 2008, ApJ, 682, 985

Wuyts, S., et al. 2007, ApJ, 655, 51

—. 2011, ApJ, 738, 106

Xu, C. K., Sun, Y. C., & He, X. T. 2004, ApJ, 603, L73

Xu, C. K., Zhao, Y., Scoville, N., Capak, P., Drory, N., & Gao, Y. 2012a, ApJ, 747, 85

Xu, C. K., et al. 2012b, ApJ, 760, 72

Yuan, F.-T., Takeuchi, T. T., Matsuoka, Y., Buat, V., Burgarella, D., & Iglesias-Páramo, J. 2012, A&A, 548, A117

Zepf, S. E., & Koo, D. C. 1989, ApJ, 337, 34

Zirm, A. W., et al. 2007, ApJ, 656, 66